GSI Report
2019-2
October 2019

News and Reports from

High **E**nergy **D**ensity generated by Heavy Ion and Laser Beams

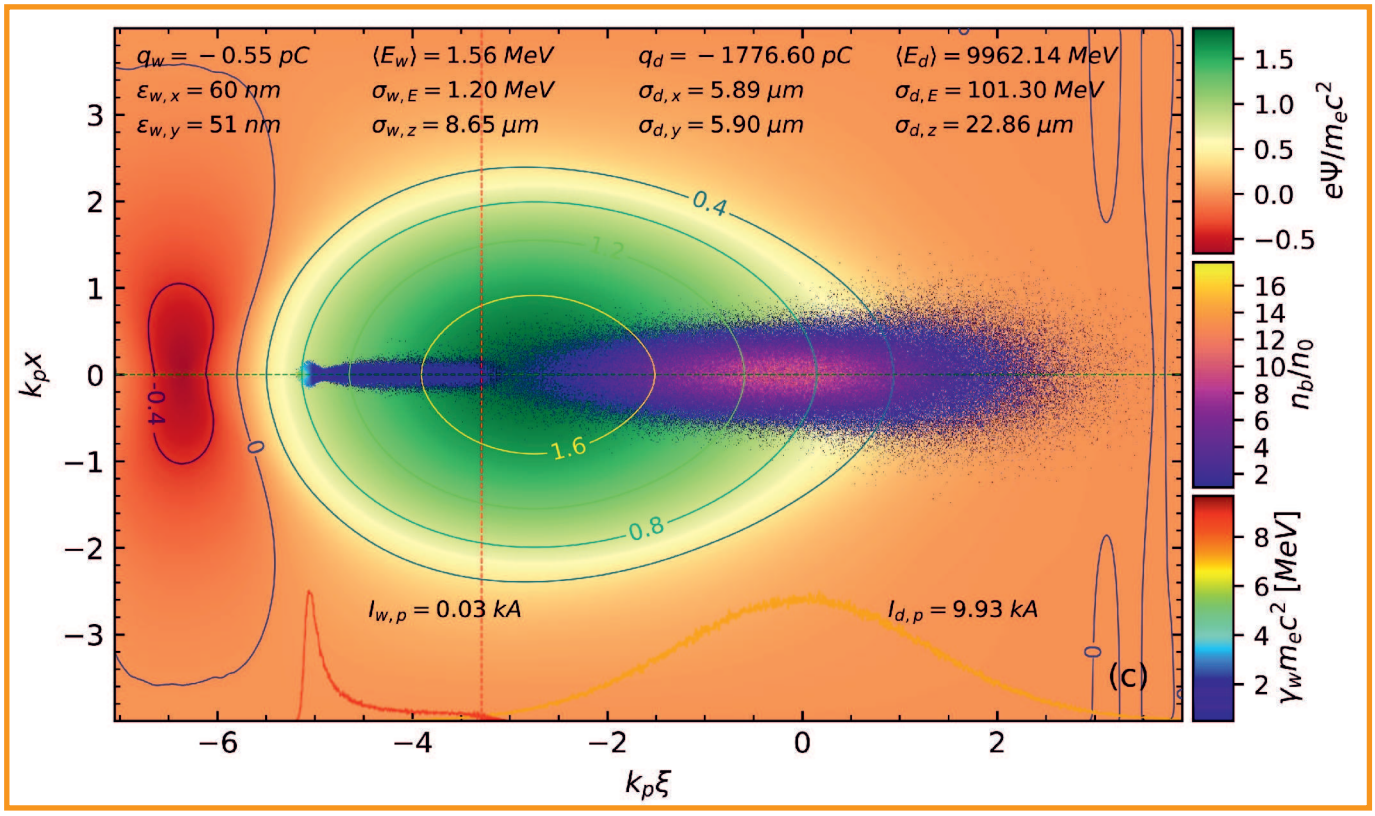

The HED@FAIR Collaboration - Report 2018

Trojan Horse Injection Scheme:

The cover picture shows a simulation of a promising plasma-based particle accelerator scheme, the so-called trojan horse injection. The realization of plasma-based accelerators would provide accelerating capabilities orders of magnitude above conventional particle accelerators. But the realization faces several problems which are not only of technical nature, but also of physical nature like transverse phase space matching, energy-spread, beam-plasma instabilities and limited energy from the driver beam for the beam-driven plasma wakefield.

The scenario of the Trojan horse injection described in the contribution on page 44 in chapter 3 makes use of a laser pulse that ionizes residual He-gas in the accelerating region of the plasma wakefield, which is induced by a dense driver beam. The cover picture shows the simulation of this injection scheme with driving electron beam, accelerating and focusing wakefield region and the region of the laser-pulse ionized residual gas. **(Reference:** Physics of Plasmas **26**, 073103 (2019); doi: 10.1063/1.5108929)

News and Reports from

High Energy Density generated by Heavy Ion and Laser Beams

2018

October 2019

Imprint

Publishers:

HED@FAIR Collaboration
(https://www.gsi.de/work/forschung/appamml/plasmaphysikphelix/hed_at_fair.htm)

GSI Helmholtzzentrum für Schwerionenforschung GmbH, Darmstadt, Germany (http://www.gsi.de)

GSI is member of the Helmholtz association of national research centers
(http://www.helmholtz.de)

Editors:

Karin Weyrich (k.weyrich@gsi.de)

Dieter H.H. Hoffmann (dhoffmann@ikp.tu-darmstadt.de)

DOI: 10.15120/GSI-2019-01053

Printed in Darmstadt by GSI, October 2019

Editorial

Dear Colleagues,

this year we are later than usual with our report. Keep in mind that in this report the contributions are about results achieved predominantly in 2018, however, in this preface we are also reporting on a few related news and developments of the current year 2019. Our scientific year started as always with a first meeting of our community at Hirschegg, Austria, where under the umbrella of the 39th International Workshop on 'High Energy Density Physics generated by Intense Ion and Laser Beams 2019' we discussed the progress in our field made in 2018.

The 2018 annual meeting of the HED@FAIR collaboration was held at the University of Castilla La Mancha in Ciudad Real in Spain, hosted by the Institute for Energy Research under the leadership of Professor Roberto Piriz. Details and a summary of this meeting are given in this report on pages 1 and 2.

This year again as in the previous ones the contributions originate from many countries, USA, China, Israel Russia, just to name a few. - The amount of chinese contributions to this report was also reflected in the strong participation from China at the Hirschegg meeting this year. - This internationality of the submitted contributions is also a clear indication of the worldwide strong interest in High Energy Density Physics, where lasers as well as intense ion beams are interesting drivers to achieve high energy density states of matter. Therefore advanced diagnostic tools to determine the plasma parameters of such new states of matter are necessary to be developed and were also the main issue of discussion at the HED@FAIR meeting in Spain in October 2018. One example for an elaborated diagnostic is the use of the Stark effect to determine the ion temperature in a high-energy-density plasma (see contribution on page 3). Also proton radiography is yet another example that will enable progress in the understanding of high energy density states of matter (view contributions on pages 6, 8, 10). Neutron generation with high intensity lasers is a rapidly developing field with numerous applications as demonstrated in contributions on pages 53 and 54, to mention only some examples for advanced diagnostic methods. On the other hand the demand for new sources of energy is represented by several contributions in the last chapter of the report addressing subjects relevant for inertial fusion energy, for example on thermonuclear ignition and the onset of propagating burn. This was studied in a contribution from Rochester LLE, by Alison Christopherson (LLE) as first author (see page 61), who did win the Laser and Particle Beams (Cambridge University) Prize for young scientists and also presented this topic successfully at the IFSA conference in Osaka (September 2019). The topic of proton-Boron fusion has gained relevance again and seems to evolve rapidly. In this report a contribution to this topic can be found on page 67, while on many conferences this year the topic was represented, too.

At GSI/FAIR the construction of the new accelerator facility is making visible progress and the schedule still envisions first experiments in 2025. This demands for having all necessary diagnostics available and ready to take data well before this time. The FAIR phase-0 is therefore designed to complete and test the experimental equipment.

This report has now a history of about 40 years - starting with a first issue in June 1980 with the year 1979 as reporting period - and was initiated by Professor Bock (GSI). The present issue will be right in time accompanying the preparations for the anniversary meeting in Hirschegg, where we have been meeting continuously since 40 years. - It is our aim to have a one page contribution to the next issue of the report from each topic presented at the next meeting at Hirschegg. And with some effort and luck, we may be ready to publish this next issue of the report about the scientific results in 2019 in June 2020 right in time for the also 40th anniversary of this report series now.

Dieter H.H. Hoffmann and Karin Weyrich, October 2019

Contents

HED@FAIR news

Annual Meeting Summary

3rd – 5th October 2018, Ciudad Real, Spain

Meeting participants during the INEI laboratory tour (photo: Ramón Sobrino-Muñoz)

The annual meeting of the collaboration High Energy Density at FAIR (HED@FAIR) was held this year in Spain, hosted by the Institute for Energy Research (INEI) at the University of Castilla-La Mancha, from October 3rd to 5th. During these three days, about 50 of researchers from Germany, Russia, Spain, China, United Kingdom, and Czech Republic, have made reports about their most recent scientific progress and discussed new results related with the design and performance of experiments to be carried out at the upcoming facility for antiproton and ion research (FAIR) facility.

The meeting was open by an introductory talk by the collaboration spokesperson A. Golubev, who gave a general overview of the present status of the collaboration and of the progress of the FAIR civil work. After the ground breaking ceremony in summer 2017, the FAIR construction site is now well under way with major work being done on the SIS-100 synchrotron building that is best illustrated by the regularly-updated drone videos made available on GSI webpage (https://www.gsi.de). In the coming months, the call for tender for the construction of the south area that includes the plasma physics experimental area should be closed, at about the time of the next project evaluation in 2019. First experiments are still planned for 2025.

During the meeting a total of 29 speakers exposed their results on different aspects of the collaboration. The HED science at FAIR and at other facilities was presented by researchers from Germany, USA and China. Advances in the development of the proton radiography system PRIOR were discussed by researchers from Germany and Russia. German researchers discussed about the technical infrastructure, and diagnostic developments for the HIHEX experiment were presented by Russian and German scientists. Besides, researchers from UK, Czech Republic, USA, Russia and China illustrated the audience about the plasma physics research programs at respective facilities in their countries. By last, researchers from Spain presented theoretical work to support some of the experiments planned in the collaboration.

Call for expression of interest (EOI) on diagnostics

Diagnostics are essential to all types of plasma physics experiments. Along experiment-specific diagnostics, the HED@FAIR collaboration wants to establish a suite of diagnostics that will be available for all to work with. These diagnostics include stand-alone devices like fast oscilloscopes and cameras, streak cameras and X-ray detectors. They also include more complicated setups like VISAR, pyrometers for instance.

Discussions on possible contributions and expression of interest have taken place during the annual meeting in Ciudad Real, during a dedicated session and also on bi-lateral basis during the meeting. The executive board would like to remind all interested collaboration partners to contact them ASAP and no later than Dec. 31st 2018 if they wish to overtake the responsibility of one or several diagnostics for FAIR. EOI should be addressed to the collaboration spokesperson or the chair of the collaboration board.

For information, a list of typical diagnostics is described in the technical design report:
https://www.gsi.de/fileadmin/Plasmaphysik/HED_at_FAIR/APPA_cave/TDR_FAIR_diagnostic_nocost.pdf

Vincent Bagnoud

1 New Diagnostic Methods and Diagnostic Tools

Determination of the ion temperature in a high-energy-density plasma using the Stark effect *

D. Alumot[†1], *E. Kroupp*[1], *E. Stambulchik*[‡1], *A. Starobinets*[1], *I. Uschmann*[2], *and Y. Maron*[1]

[1]Weizmann Institute of Science, Rehovot 7610001, Israel; [2]Institut für Optik und Quantenelektronik, Friedrich-Schiller-Universität, D-07743 Jena, Germany

We present experimental determination of the ion temperature in a neon-puff Z-pinch [1]. The diagnostic method is based on the effect of ion coupling on the Stark lineshapes. It was found, in a profoundly explicit way, that at stagnation the ion thermal energy is small compared to the imploding-plasma kinetic energy, where most of the latter is converted to hydromotion. The method here described can be applied to other highly non-uniform and transient high-energy-density (HED) plasmas.

The conversion of the kinetic energy of accelerated plasmas to ion heating, resulting in radiation emission or in nuclear fusion, is of fundamental interest in the field of HED plasmas, and has general implications for laboratory and astrophysical plasma research. Of particular importance is determination of the ion thermal energy, addressed here.

In a stationary plasma, the ion temperature is associated with the spread of the kinetic energy per ion K_i. The latter is manifested in the Doppler broadening of spectral lines emitted or, in the case of fusion plasmas, in a respective spread of the energy spectra of neutrons and other products of the fusion reactions. However, for plasmas formed in the process of implosions, both thermal *and* hydrodynamic motions contribute to K_i. Therefore, the *apparent* ion Doppler pseudo "temperature" $T_i^D = \frac{2}{3}\langle K_i \rangle$ may be a significant overestimation of the *true* ion temperature T_i. In an imploding plasma the electron temperature T_e cannot be assumed to represent T_i, either: the radial kinetic energy is first transferred to T_i and then to T_e. Thus, $T_e < T_i < T_i^D$ until the plasma fully thermalizes.

Here we present direct measurements of T_i in a HED plasma, requiring only localized instantaneous spectroscopic data. The underlying physical phenomenon is the ion-temperature dependence of the Stark profile of certain lines in moderately coupled plasmas.

We demonstrate this approach by measuring T_i at the stagnation phase of a neon-puff Z-pinch, where the $T_e < T_i < T_i^D$ inequality holds. In our Z-pinch system stagnation lasts a few nanoseconds, during which the plasma is characterized by electron density and temperature $\lesssim 10^{21}\text{cm}^{-3}$ and ~ 200 eV, respectively. These parameters are also typical for the measurements described here.

Stark line broadening is widely used for plasma diagnostics. The Stark width depends strongly on the plasma density (typically, between $\propto N_e^{2/3}$ and $\propto N_e$); this is true for broadening due to plasma electrons and ions alike. Contrary to that, the temperature dependence is rather weak and sometimes non-monotonous. Furthermore, the electron and ion contributions may have opposite tendencies resulting in a nearly complete cancellation over a wide temperature range. Consequently, the Stark diagnostics is typically perceived synonymous to the density diagnostics. However, if N_e and T_e are known with a sufficient precision independently of the lineshape measurements, then even the moderate Stark-width sensitivity to T_i can be used to infer the latter; this approach is used in the present study.

The static Stark effect in a hydrogen-like atom is proportional to the electric field F. In a plasma, the charged particles form a microfield distribution around the typical field value that depends on the density N_p and charge q_p of the plasma particles as $\propto |q_p| N_p^{2/3}$. This distribution is sufficient for evaluating the plasma broadening by the plasma ions when their Stark effect can be described in the quasistatic approximation. Furthermore, the electron broadening is usually smaller than that due to the ions, because of the dynamical nature of the electron perturbation and the larger ion charge. Thus, the broadening of these lines is mainly determined by the ion microfield distribution.

In an ideal plasma, the microfield distribution is a universal Holtsmark function that is independent of temperature. However, Coulomb interactions between the particles modify the Holtsmark distribution, due to the Debye screening and the repulsion between the ions and the positively charged radiators, resulting in a decrease of the Stark broadening.

The Debye screening influences the ion fields at large distances ($r \gtrsim \lambda_{D,i}$, where $\lambda_{D,i}$ is the ion Debye length), while the Coulomb repulsion is only important at short distances ($r \lesssim r_{m,i}$, where $r_{m,i} = q_i^2/T_i$ is the classical distance of minimal approach). In a weakly non-ideal plasma the double inequality $r_{m,i} \ll r_i \ll \lambda_{D,i}$ holds, where $r_i = (4\pi N_i/3)^{-1/3}$ is a typical inter-ion distance; since the line width is mostly affected by microfields formed by ions at distances $\sim r_i$, the ion-temperature corrections in such a plasma are minor and the respective effect on the line broadening is small. However, the more non-ideal the plasma is (characterized by the ion–ion coupling parameter $\Gamma_{ii} = q_i^2/(r_i T_i)$), the stronger the corrections become.

As an example, Fig. 1 shows the width of Ne X Ly-δ, calculated using a computer simulation, as a function of Γ_{ii} for a few values of the electron density at a fixed electron temperature. It is seen that for each density, there is a range of Γ_{ii} where the dependence of the Stark width on it and

* This work was supported in part by the Cornell Multi-University Center for High Energy-Density Science (USA), the Israel Science Foundation, and the Air Force Office of Scientific Research (USA).

† Corresponding author. droralumot@gmail.com

‡ Corresponding author. evgeny.stambulchik@weizmann.ac.il

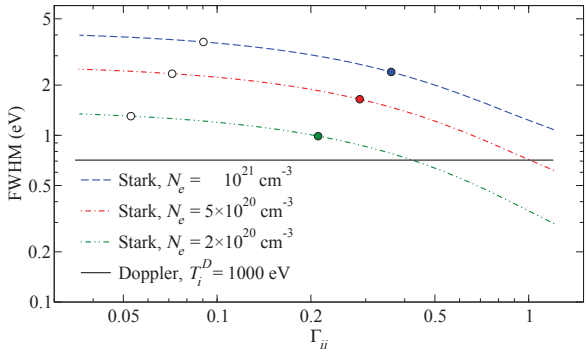

Figure 1: Ne X Ly-δ Stark width as a function of Γ_{ii}, assuming three values of the electron density and a constant $T_e = 250$ eV. The filled and opaque circles correspond to $T_i = T_e = 250$ eV and $T_i = T_i^D = 1000$ eV, respectively. Also shown is the Doppler broadening.

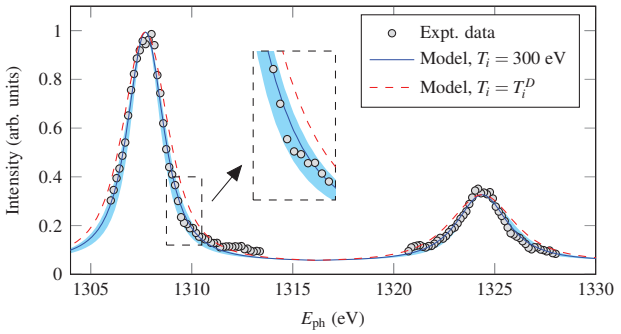

Figure 2: The experimental high-n spectra are compared to lineshape modeling for two values of T_i assumed: $T_i = 300$ eV and T_i^D. $T_i^D = 900$ eV, $N_e = 6 \times 10^{20}$ cm^{-3}, and $T_e = 200$ eV are assumed in both cases. The shaded area designates a spread of modeled spectra for T_i varying between 150 eV and 450 eV.

hence, on the ion temperature can be used for determination of T_i: for too high T_i (weakly coupled plasma) the Stark broadening is not sensitive to T_i, and for low T_i the Stark contribution becomes comparable or even smaller than the Doppler width, especially for lower plasma densities.

The x-ray output from the stagnating plasma is recorded by a $\gtrsim$ 700-eV-filtered photoconductive detector (PCD). The $t = 0$ time is defined as the time of the peak PCD output. The spectroscopic system includes three spherical crystals, recording the Ly-α satellites and the high-n Ly-δ and Ly-ϵ. Each spectrometer allows for imaging the spectra along the Z-pinch axis with a resolution of $\lesssim 50$ μm. The Ly-α satellite spectra are recorded with a 2nd-order spherical KAP crystal. Combined with collisional-radiative (CR) modeling, the spectra provide the time-resolved electron density and the total (thermal and hydro) ion velocities at any z position. Ly-δ and Ly-ϵ are recorded independently using two spherical 4th-order mica crystals. In the analyses below, we show the z-averaged spectra from an axial slice of $\Delta z = 0.5$ mm around the vertical center of the pinch.

Two singly-gated ($\sim$ 1 ns) multi-channel plate (MCP) detectors are used, one for the Ly-α satellite spectra and the other for Ly-δ and Ly-ϵ. Correcting for photon propagation, this enables simultaneously recording all three spectra. We note that even though a single high-n line is sufficient for application of the method, two such lines (Ly-δ and Ly-ϵ) were recorded to decrease the uncertainties.

We present detailed analysis of the Ly-α and high-n lineshapes recorded simultaneously at $t = 0$. The spectral analysis of the Ly-α-satellite lines yielded values of $T_i^D = 900 \pm 200$ eV and $N_e = (6 \pm 1) \times 10^{20}$ cm^{-3}. We refer the interested reader to the full publication [1] for complete details. These values are used in order to calculate T_i from the high-n lineshapes, which were recorded simultaneously from the same plasma region.

The spectra of Ly-δ and Ly-ϵ were modeled by convolving the Doppler and instrumental broadenings with the calculated Stark lineshapes, for a range of T_i values. Results of the high-n lineshape analysis are presented in Fig. 2, demonstrating that the best fit is obtained for $T_i = 300 \pm 150$ eV, while assuming $T_i = T_i^D$ results in lineshapes that are far from fitting the data.

Table 1: The measured plasma parameters for various times throughout stagnation.

t (ns)	$N_e(10^{20}$ cm$^3)$	T_i^D (eV)	T_i (eV)
-2.5	5.0 ± 1.0	1900 ± 400	400 ± 150
-1.5	3.0 ± 0.5	1100 ± 300	300 ± 150
-1.0	3.5 ± 0.5	1300 ± 300	350 ± 150
0.0	6.0 ± 1.0	900 ± 200	300 ± 150
2.0	2.5 ± 0.5	1000 ± 250	550 ± 250
2.5	5.5 ± 1.0	600 ± 200	400 ± 150
4.0	2.5 ± 0.5	600 ± 200	550 ± 200

The spectral analysis was performed on multiple shots at various times throughout stagnation. The results are summarized in Table 1. We observe that most of the kinetic energy of the ions is stored not in the thermal motion, but rather in a form of the hydrodynamic macro-motion, while the true ion temperature is, as a rule, close to the electron temperature.

We emphasize that this is the first study where the ion temperature of a HED plasma is directly obtained from instantaneous localized measurements, without the necessity to obtain an entire history of the plasma parameters, and without relying on complex energy-balance argumentations. Thus, the approach described here may be considered for measurements in highly non-uniform and transient HED plasmas.

References

[1] D. Alumot *et al.*, "Determination of the ion temperature in a high-energy-density plasma using the Stark effect", Phys. Rev. Lett. **122**, 095001 (2019).

State of the art of the plasma stripper and its interferometric diagnostic*

P. Christ[1], K. Cistakov[1], M. Fröhlich[1], R. Gavrilin[3], A. Khurchiev[3], M. Iberler[1], O. Rosmej[2], S. Savin[3], and J. Jacoby[1]

[1]Goethe Universität, Frankfurt Germany; [2]GSI, Darmstadt, Germany; [3]NRC "Kurchatov Institute" - ITEP, Moscow, Russia

The acceleration of highly intense heavy ion beams at FAIR requires improved technologies concerning ion beam stripping. As an example, theoretical calculations for Iodine ions predict a higher equilibrium charge state for a dense, highly ionized hydrogen plasma target than for a cold gas target at projectile velocities below 6 MeV/u [1]. In order to utilise this advantage, several plasma stripper devices were developed [2, 3].
The latest model posses a novel cylindrical coil to improve the symmetry and homogeneity of the magnetic field distribution to enhance the ion beam transmission. Moreover, a higher amount of energy coupled into the plasma was intended for creating a high electron density and ionization degree needed for the stripping interaction [4, 5].
To complete the spectroscopic diagnostic shown in [5], a time-resolved spectroscopy by streak camera recording the H_β-broadening was carried out. In figure 1, the peak density obtained at 500 µs streak time, 20 kV and 30 Pa was about $4.3 \cdot 10^{16}$ cm^{-3}.

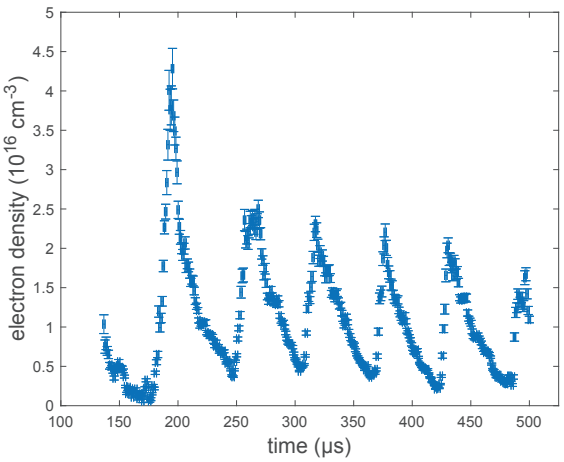

Figure 1: Electron density evolution in time

As a further diagnostic, an array of six photo diodes, which will be placed along the symmetry axis, was developed to gather spatially-resolved information about the discharge dynamics. Additionally, a first attempt for a more precise measurement of the electron temperature was conducted. In this process, some amount of argon was added to the hydrogen working gas, much enough for having strong transition lines of argon but little enough for not dramatically changing the plasma parameters to improve the accuracy of the Boltzmann plot. The new design will be tested at a beam time at GSI, Z6 early in 2019 to measure transmission, stopping power and charge state distribution.
For an even better understanding the stripping characteristics of the plasma, a highly precise, comparative and time-resolved diagnostic of the free electron density and ionization degree is vital. To profit from a high accuracy and time resolution, an interferometric approach is in development. The interferometer is based on the Mach-Zehnder scheme and is run by a polarized He/Ne-laser at 632.8 nm. Moreover, an acousto-optic modulator is used as a frequency shifter for the reference beam to gain an 80 MHz beat signal on the detector to benefit from measuring the plasma phase shift as a temporal parameter [6].
In order to develop the interferometric diagnostic detached from the plasma stripper, a separate setup consisting of a modified version of the spherical theta-pinch has been constructed. The capacitor bank is now set at 30 µF at a load voltage up to 20 kV resulting in 6 kJ energy and a resonant frequency of 10.5 kHz.
The laser, the detector and the signal processing units are contained inside a Faraday-cage to protect them from the electromagnetic noise during the discharge.

Prospective tasks concerning the interferometric diagnostic will be the introduction of a second wavelength to distinguish the contribution of free electrons from neutral atoms according to their different dispersive behaviour. Finally, a time-resolved polarimetric measurement of the magnetic field distribution of the coil in shot operation by utilising the Faraday-effect of a magneto-optic crystal is intended.

* Work supported by BMBF, HIC4FAIR, HGS-HIRe.

References

[1] T. Peter, R. Arnold and J. Meyer-ter-Vehn, Physical Review Letters, 57, 1859 (1986).

[2] C. Teske et al., Physics of Plasmas **19**, 033505 (2012).

[3] G. Loisch et al., IEEE Trans. Plasma Sci., **42** (5), 1163-1172 (2014).

[4] K. Cistakov et al., GSI SCIENTIFIC REPORT 2016, RESEARCH-APPA-PP-22.

[5] P. Christ et al., GSI SCIENTIFIC REPORT 2017, RESEARCH-APPA-PP-25.

[6] P. Christ, Master thesis, 2017.

Hard X-ray and Proton Radiography of Underwater Electrical Wire Explosion

A. Müller-Münster*[1], C. Hock[1], M. Iberler[1], J. Jacoby[1], P. Neumayer[2], D. Varentsov[2]
[1]Goethe University Frankfurt, Germany
[2]GSI, Darmstadt, Germany

By the use of Underwater Electrical Wire Explosion (UEWE) one can create and study warm dense matter (WDM) in laboratory. With a moderate pulsed power generator, with a total Capacity of 10μF, charging voltages up to 40kV, cylindrical strip line and a thyratron as switch, it is possible to create dense plasmas with 10-100 kJ/g specific energy, near-solid density and 1-2 eV temperature. Due to the high electric breakdown threshold of water (>300 kV/cm) and relatively small wire expansion velocity (~ 1km/s) there's no parasitic plasma formation along the wire surface. This makes UEWE an efficient method to study the fundamental properties of metals in extreme states [1-8].

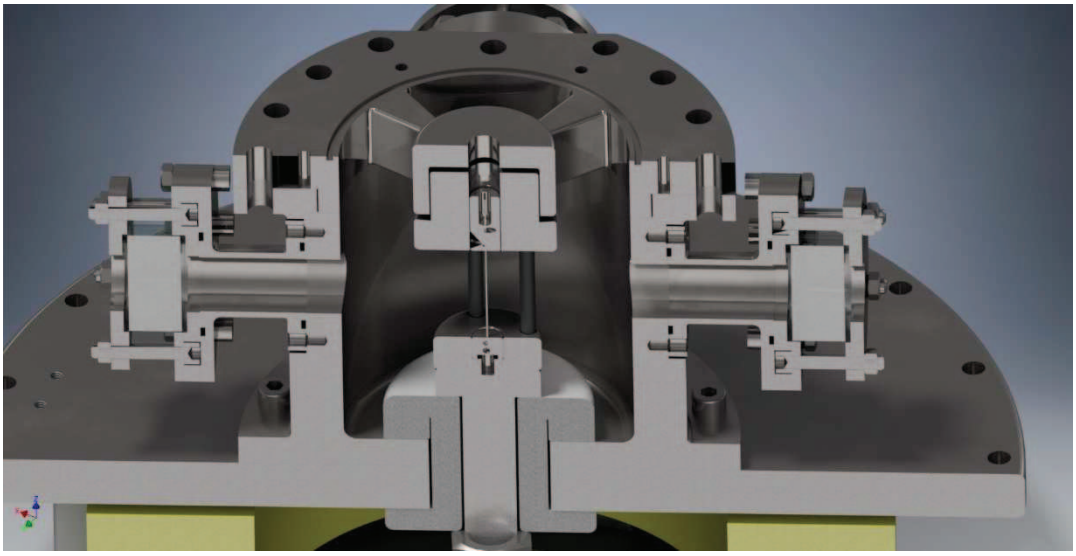

Figure 1: Half-section of the UEWE target chamber. The exploding wire is placed in the middle of a stainless steel chamber.

One of the main challenges is the determination of plasma parameters and especially the temporally and spatially resolved measurements of the target density. For the radiography of an opaque exploding wire in water one needs high energy x-rays or charged particles, which areable to penetrate the surrounding water and the windows of the target chamber too. Hence soft (few keV) x-rays, which are often used for radiography of thin tungsten wires exploding in vacuum [9] are not suitable for UEWE experiments. In most UEWE experiments only the evolution of the wire radius is measured by optical means. This is the reason why the majority of all the EOS and conductivity data obtained in the numerous UEWE experiments during the past four decades rely on the assumption of the radial uniformity of the density distribution during the whole course of wire explosion. On the other hand, there're clear theoretical and numerical indications showing that the assumption of radial uniformity does not hold, for microsecond and sub-microsecond UEWE discharges [4,7,9]. Therefore the question of uniformity of liquid metal in near critical state, formed by rapid ohmic heating in water bath still remains open.

References

[1] M.M. Martynyuk Sov. Phys.-Tech. Phys. 17 (1972) 148.
[2] U. Seydel et al., Z. Nuturf. 30a (1975) 1166.
[3] A.W. DeSilva and J.D. Katsouros, Phys. Rev. E 57 (1998) 5945.
[4] A. Grinenko et al., Phys. Rev. E 72 (2005) 066401.
[5] T. Sasaki et al., Laser and Par. Beams 24 (2006) 371.
[6] A.W. DeSilva at al., Phys. Rev. E 83 (2011) 037402.
[7] D. Sheftman et al., Phys. Plasmas 18 (2011) 092704.
[8] Y.E. Krasik et al., IEEE Trans. Plasma Sci. 44 (2016) 412.
[9] T.A. Shelkovenko et al., Plasma Phys. Rep. 42 (2016) 226.

*Mueller-Muenster@iap.uni-frankfurt.de

Laser interferometry for measurements of electron density and degree of ionization in a hydrogen plasma target*

A.O. Khurchiev#, R.O. Gavrilin, S.A. Visotskiy, D.S. Kolesnikov, A.V. Kantsyrev, I.V. Roudskoy, S.M. Savin, A.A. Golubev, A.P. Kuznetsov
«NRC «Kurchatov Institute» - ITEP, Moscow, Russia.

Introduction

Investigation of stopping power in an ionized matter is important for obtaining new knowledge in high energy density in matter and plasma physics. An important part of these experiments is finding correlation between ion energy loses and plasma parameters such as: electron density, temperature and degree of ionization. The hydrogen plasma target [1] and facility for energy loss measurements [2] were developed at ITEP. Laser interferometry was used to determine parameters of plasma target.

Experimental setup

An interferometer [3] was based on He-Ne laser with λ_1 = 632.8 nm and Nd^{3+}:YVO_4 laser with intracavity generation of the second harmonic (λ_2 = 532 nm). Laser beams are spatially matched with mirrors and directed to the Mach-Zehnder interferometer. The analyzed plasma target is placed in one of the interferometer arms. After passing through the interferometer, the probing laser beams with different wavelengths are spatially separated by dispersion prism (Figure 1).

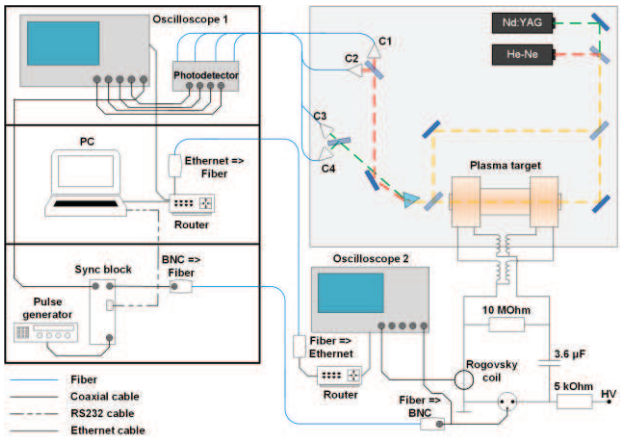

Fig.1. Schematic of the experimental setup.

In order to reduce electromagnetic noise, the measuring equipment was placed in a protective box. The oscilloscopes and the plasma target were synchronized using the synchronization block, which also used for data acquisition.

Results

The linear density of free electrons and the degree of plasma ionization in plasma target were measured for initial hydrogen pressures 1–3 Torr and capacitor battery voltages 3 – 6 kV. Figure 2 shows time dependence of the linear electrons density and the discharge current for the initial pressure 1 Torr and the voltage 6 kV.

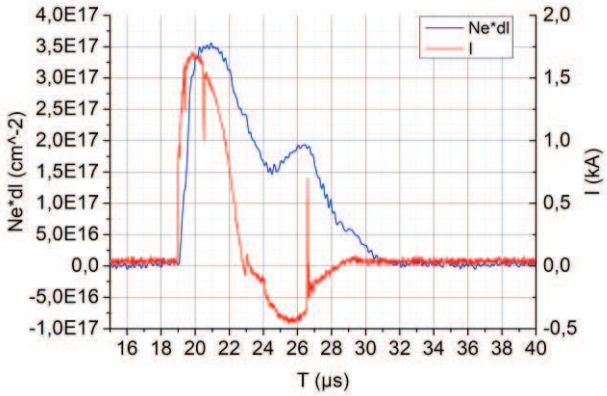

Fig. 2. Time dependence of the linear electron density and the discharge current.

Figure 3 shows the dependence of the linear electron density and the degree of ionization on pressure at various voltages for two discharge channels. The maximum linear electron density was reached (6.6±0.7) cm^{-2} at a voltage of 6 kV and pressure of 3.5 Torr. The maximum degree of ionization 0.35±0.01 was achieved at initial pressure of 1 Torr and a voltage of 6 kV.

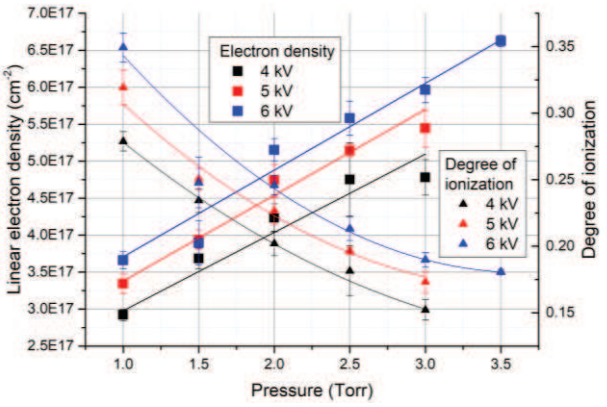

Fig.3. Linear electron density and degree of ionization plasma target versus pressure.

References

[1] A. Golubev, V. Turtikov, A. Fertman et.al, Nucl. Instr. An d Meth. A, V. 464, (2001), p. 247
[2] R.O. Gavrilin et al. GSI Report 2018-2, p. 34
[3] A. P. Kuznetsov et al., Plasma Physics Reports, 2013, Vol. 39, No. 3, pp. 248–254

* Work supported by RFBR grand №18-02-00967
#ayuxa@inbox.ru

Density reconstruction in proton radiography experiments with shock compressed gases*

D. Kolesnikov[1#], A. Bogdanov[1], A. Golubev[1], A. Kantsyrev[1], V. Mintsev[2], V. Panyushkin[1], N. Shilkin[2], A. Skobliakov[1]

[1]Institute for Theoretical and Experimental Physics named by A.I. Alikhanov of National Research Centre "Kurchatov Institute", Moscow, Russia; [2]IPCP RAS, Chernogolovka, Russia

In experiments on investigation of shock compressed gases and non-ideal plasma [1] proton radiography method is one of the best diagnostic methods for obtaining direct information about density distribution in dynamic target. During such experiments, gases have to be contained inside shell. Complicated form of beam transmission dependency on areal density [2] leads to non-trivial problem of extracting values of areal density (and subsequently volume density) of component from transmission of whole assembly. Implication of Monte Carlo modeling in Geant4 can provide solution by comparison of numerical simulation results with experimental data.

Experimental data processing

Investigation of non-ideal Xe plasma has been carried out with 800 MeV protons at PUMA facility [3]. Target (Fig.1) is Xe gas at 2.5 bar initial pressure and normal temperature contained inside cylindrical PVC shell with 22 mm inner diameter and 1 mm thickness. It undergoes shock-compression driven by detonation of HE charge with formation of non-ideal plasma behind wave front. Series of proton radiography images before and in the moment of explosion were obtained (Fig.2).

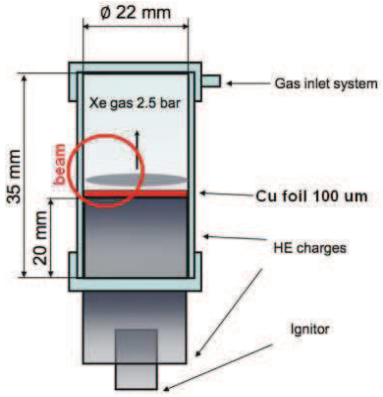

Figure 1: Scheme of target

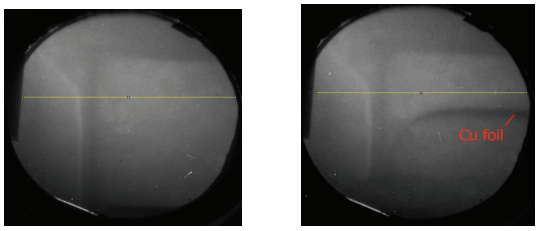

Figure 2: Proton radiography images of Xe target in static (left) and in dynamic process (right, detonation wave propagates from bottom to top). Transmission profiles taken along yellow lines.

To obtain image of target in units of proton beam transmission, operation of division of target image by white field image (WF, image in absence of target) should be performed. Instability of beam cross-profile from shot to shot leads to significant errors in reconstructed density distribution. To prevent such errors the initial proton-radiography images are corrected with the use of asymmetrical gauss function [4] corresponding to beam profile (Fig.3,4).

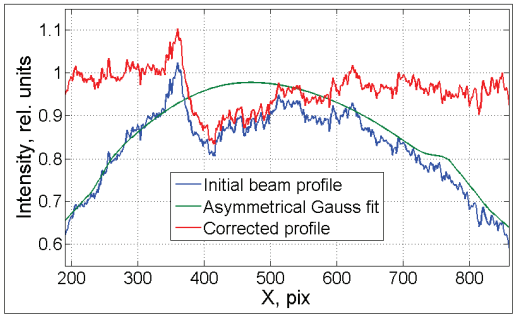

Figure 3: Correction of experimental beam profile with asymmetrical gauss fit (static target)

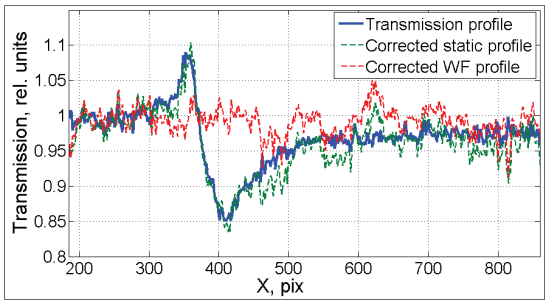

Figure 4: Corrected transmission profile of static target

Another factor preventing accurate density reconstruction is presence of noise signal in images due to neutron radioactive background, digital camera noises, etc. Noise suppression effected by multilevel wavelet thresholding [5] and exponential averaging filter [6] (Fig.5).

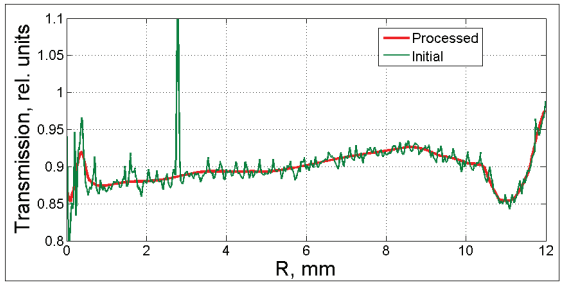

Figure 5: Example of noise suppression in experimental signal (dynamic process)

*Work supported by RFBR (grant № 18–38–00708)
#dstorm1@mail.ru

The full-scale Geant4 model [7] of PUMA microscope was used to calculate images of target with compressed Xe. Model of target consists of several coaxial cylindrical tablets of Xe with different values of compression ratio k inside the same PVC shell (Fig.6).

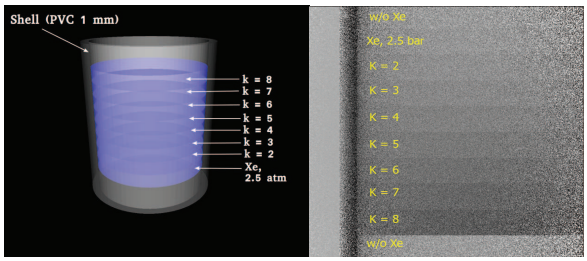

Figure 6: Model of the xenon target (left) used for numerical calculation of transmission image (right) in Geant4.

Comparison of cross profiles (Fig.1 yellow lines) for experimental image of static target and model image showed difference between them (Fig.7), especially near shell area where transmission have strong gradients. It may be referred to blur in registration system (scintillator) and chromatic effects in ion-optics. Such blur is defined by point-spread function (PSF). In our case, PSF estimated as sum of three gauss curves (Fig.7) provides good agreement (RMS of 0.5%) between blurred model profile and experimental one. All model profiles blurred by this PSF to provide possibility for comparing experimental data and results of numerical calculation to define proper value of gas compression ratio.

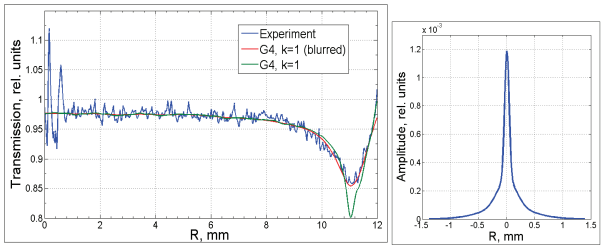

Figure 7: Left - comparison of experimental and numerically calculated transmission profiles (static target). Right – intensity profile of PSF used to blur model image.

Comparison between transmission profile of target in dynamic process and model profiles with different compression ratios k (Fig.8) shows that density distribution of Xe in radial direction is not uniform.

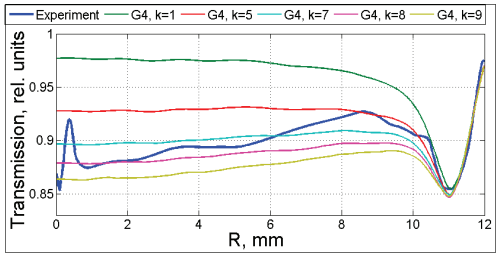

Figure 8: Comparison of experimental and numerically calculated transmission profiles (dynamic process)

Values of Xe areal density distribution (Fig.9) estimated by minimizing function of χ^2-deviation between experimental and model profiles separately for each given point in radial direction. Subsequent application of inverse Abel transform [8] provides volume density distribution inside target (Fig.10).

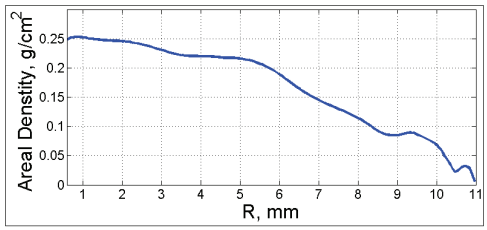

Figure 9: Obtained experimental radial distribution of areal density in Xe plasma.

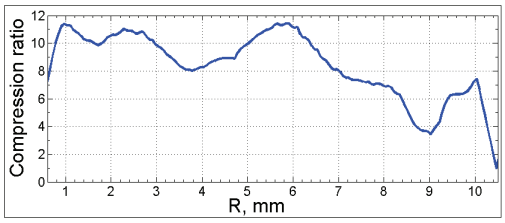

Figure 10: Obtained experimental radial distribution of volume density in Xe plasma.

Summary

Method for reconstruction of volume density distribution in proton radiography experiments with shock-compressed gases developed. It consists of several methods for correction of distortions in initial data and reconstruction of density distribution from transmission of target with the use of Geant4 numerical simulation results.

Performance of this method demonstrated on processing and analysis of experimental data on investigation of non-ideal xenon plasma at PUMA facility in ITEP.

Described method may be used for data processing and analysis at experiments on PRIOR-II facility of FAIR.

References

[1] Mintsev V.B., Shilkin N.S., et al., “High-explosive generators of dense low-temperature plasma for proton radiography”, CPP, 2018, V.58, p. 93-98

[2] Morris C. et al., “Charged particle radiography”, Rep. Prog. Phys., 2013, V.76

[3] Kantsyrev A.V. et al., IET, 2014, V. 57, pp. 1–10

[4] Kolesnikov D.S., Kantsyrev A.V., Golubev A.A., “Method for the Reconstruction of the Volume Density Distribution in Dynamic Targets”, Nuclear Physics and Engineering, 2017, V.8, No.2, p. 194-199

[5] Smolentsev N.K., “Foundations of Wavelet Theory. Wavelets in MATLAB”, 2005, Moscow: DMK

[6] Tolstunov V.A., Stepanets P.V., TUSUR journal, 2009, V.20, No.2, p. 43

[7] Kantsyrev A.V., Skoblyakov A.V., et al., “Monte-Carlo Geant4 numerical simulation of experiments at 247-MeV proton microscope”, JPCS, 2018, V.946, No.1

[8] D. Kolesnikov, A. Bogdanov, A. Golubev, A. Kantsyrev, A. Skobliakov, “Volume density reconstruction of targets at proton radiography experiments”, GSI-2017-2 Report, June 2017, p.36

Study of Shock Wave Compressibility of Textolite for experiments at PRIOR*

V. Mochalova[1,#], A. Utkin[1], V. Rykova[2], M. Endres[3], and D.H.H. Hoffmann[3]
[1]Institute of Problems of Chemical Physics RAS, Chernogolovka, Russia; [2]MEPhI, Moscow, Russia;
[3]Technical University Darmstadt, Darmstadt, Germany

Using a VISAR laser interferometer with nanosecond time resolution, the experiments on developing of targets, investigation of the shock wave structure and spall strength and also the determination of Hugoniot data were performed with samples of textolite with longitudinal and transverse direction of the fibers. The goal of this study is development of targets for experiments at a novel diagnostic system proton microscope (PRIOR) at the TU Darmstadt. Textolite is a composite anisotropic material with a low specific weight, consisting of interwoven fabric fibers and a binder - epoxy resin. The density of the material tested is 1.265 g/cm^3. The measured sound speed along the fibers is C_l = 7.1 km/s, transverse - C_l = 2.45 km/s.

To study the shock wave compressibility of textolite under high pressure, the explosive propellant charges were used to provide a flat throw of aluminum flyer plates. Their velocity varied from 0.7 to 5.05 km/s. Shock waves in the samples tested were created by the collision of an aluminum flyer plate with the metal plate. The velocity of the sample-water boundary was recorded by VISAR interferometer. To determine the absolute value of the velocity, two interferometers with velocity fringe constants of 280 m/s and 1280 m/s were used simultaneously. A laser beam was reflected from an aluminum foil which was glued onto the sample. In each experiment, average value of the shock wave velocity D was determined using interferometric data.

On the velocity profiles, for textolite with transverse direction of the fibers, after the shock jump the particle velocity is almost constant until the arrival of a rarefaction wave from the flyer plate. The oscillations on profiles are observed due to the porosity of the investigated material. Unlike the textolite with transverse orientation of the fibers, in the case when a shock wave propagates along the fibers, a two-wave configuration is recorded (precursor and shock wave), which is due to the anisotropic structure of material. The amplitude of the precursor is about 150 m/s. The velocity of the perturbations propagation along the fibers can be several times higher than the shock wave velocity, what results in the formation of the precursor. Since the amplitude of forward-running perturbations attenuates, the front of the first wave degenerates into a sound pulse, so its propagation velocity is close to 7.1 km/s, measured by the ultrasonic method.

As a result of processing of the experimental data, Hugoniot parameters of textolite in the coordinates of shock wave D – particle velocity u were found at the wave propagation along (D = 1.45 + 2.05*u, km/s) and across (D = 2.37 + 1.26*u, km/s) the fibers (fig.1).

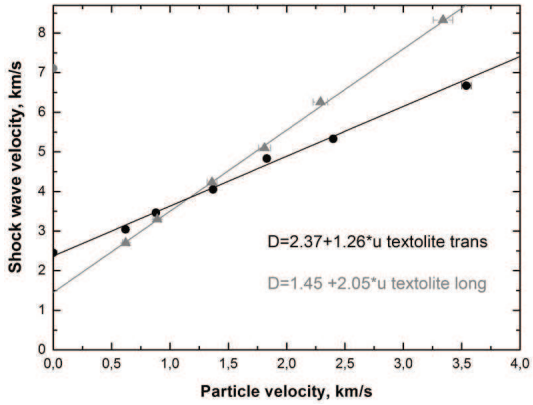

Figure 1: Hugoniot parameters of textolite.

A study of spall strength for textolite was conducted as well. The measured velocity profiles of free surface of textolite for parallel (lower profile) and perpendicular (top profile) orientation of the fibers are shown in fig.2. The exit of the shock wave on the free surface causes an increase in the velocity of the surface up to the maximum value. A rarefaction wave propagates inside the sample, which, interacting with the incident unloading wave, results in an internal fracture - a spall. The spall strength σ, which characterizes the maximum tensile stress in the sample, is determined by the equation: $\sigma=0.5\ \rho_0 C_0\ \Delta W$, where ΔW - the velocity difference between its maximum and value at the moment of arrival of spall pulse (shown by arrow), C_0 – the sound speed at zero pressure, ρ_0 – the initial density of the sample. It was found that the spall strength value of textolite with parallel orientation of the fibers is almost twice higher than that for perpendicular orientation.

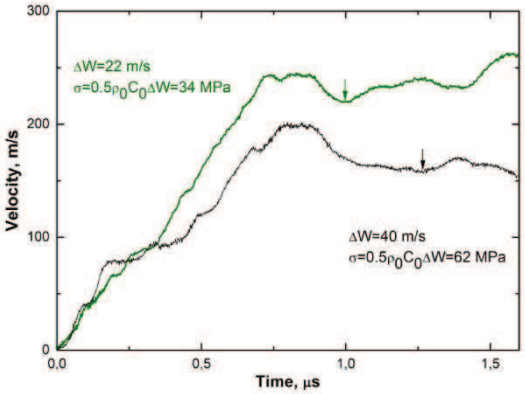

Figure 2: Velocity profiles of free surface for textolite.

It was found that shock wave properties of textolite were strongly dependent on the fibers orientation.

* Work supported by FAIR-Russia Research Center.
# roxete20000@hotmail.com

Residual dose rate estimate for PRIOR-II experiment at HHT*

V.A. Volkov[1,†], A.V. Bogdanov[1], A.A. Golubev[1], A.V. Kantsyrev[1]
[1]NRC 'Kurchatov Institute' – ITEP, Moscow, Russia

PRIOR-II [1] is the proton radiography setup with expected resolution of about 10 μm planned within FAIR project framework. As long as human intervention during the setup maintenance is necessary during an accelerator experiment, radiation safety of the experimental area becomes an important concern. In order to test the setup for meeting GSI/FAIR radiation safety requirements, 3D maps of residual equivalent dose rates induced by proton beam during the PRIOR-II run were calculated.

The simulation was performed using the FLUKA [2,3] code and AMB74 conversion coefficients set. The irradiation profile represents realistic scenario of the activation of the setup. The incident proton beam with energy of 4 GeV comes in 10 pulses. The temporal duration of each pulse is 1 μs, interval between the pulses is 60 s, and the beam intensity is 10^{12} protons per pulse (total flux of 10^{13}). For the calculation the circular parallel proton beam 1cm in diameter with Gaussian momentum spread of $5{\cdot}10^{-4}$ GeV/c was chosen. The beam parameters correspond to the upper boundary of the intensity.

For the current calculation, which does not use field mapping of the magnetic elements setup, the beam parameters, collimator and target dimensions were chosen to imitate beam collisions with the setup elements in the presence of magnetic fields. The target is a tungsten cylinder with diameter of 0.6 cm and length of 1 cm. The collimator is a tungsten cylinder with outer diameter of 3.6 cm and the length of 4 cm. The collimator inner opening diameter is 1.4 cm.

Residual equivalent dose rates for cooling times up to 1 month were calculated. The example results for the moment immediate after the end of irradiation and cooling time of 1 hour are shown in Fig. 1.

Equivalent dose rate falloff in the characteristic points of the setup (Fig.2) is shown on the Fig. 3. As can be seen from the plot, the experimental area can be put into the controlled access mode (3μSv/h criterion at point E representing the dosimeter position) in approximately 70 minutes after the measurement.

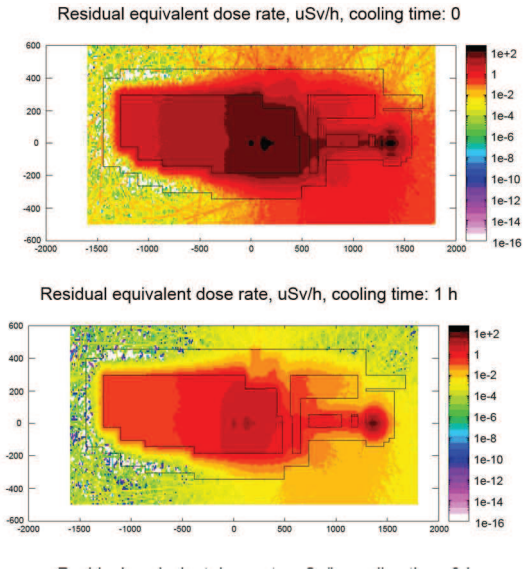

Figure 1: 3D residual equivalent dose maps immediately after the irradiation and for cooling time of 1 hour

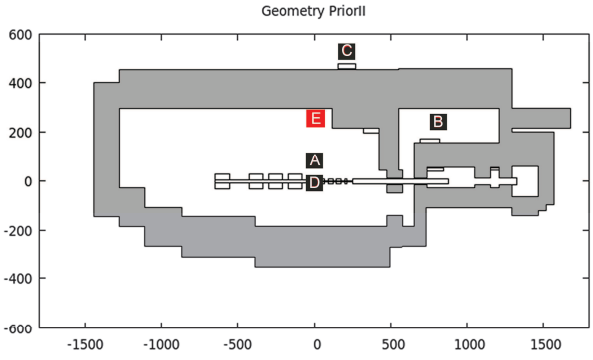

Figure 2: the setup scheme with characteristic points marked

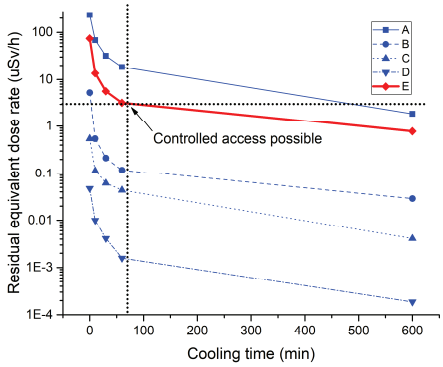

Figure 3: residual equivalent dose falloff

References

[1] D. Varentsov Review of Scientific Instruments 87, 023303 (2016)

[2] *The FLUKA Code: Developments and Challenges for High Energy and Medical Applications"* T.T. Böhlen, F. Cerutti, M.P.W. Chin, A. Fassò, A. Ferrari, P.G. Ortega, A. Mairani, P.R. Sala, G. Smirnov and V. Vlachoudis, Nuclear Data Sheets 120, 211-214 (2014).

[3] *"FLUKA: a multi-particle transport code"* A. Ferrari, P.R. Sala, A. Fasso`, and J. Ranft, CERN-2005-10 (2005), INFN/TC_05/11, SLAC-R-773

* Work supported by RFBR grant 18-38-00708
† vasilyvolkov@list.ru

Spectroscopic Investigations for Optical Beam Profile Monitors

R. Hampf[1], P. Forck[2], S. Udrea[2], A. Ulrich[1], J. Wieser[3]
[1]TU-München, Germany, [2]GSI, Darmstadt, Germany, [3]Excitech GmbH, Schortens, Germany

Optical beam diagnostic is planned for intense ion beams, which would destroy conventional beam diagnostic devices. The concept is to measure beam-induced fluorescence (BIF) from a gas target, spatially resolved, and to deduce beam profiles from these data. A more detailed description of the concept is given in [1-3]. The spectroscopic investigations on BIF have thus been continued and latest results are presented here.

Experiments have been performed at the Tandem accelerator of the Munich Meier Leibnitz Laboratory, using 87MeV $^{32}S^{8+}$ as well as 14MeV p-beams. Neon and argon were mainly used as target gases in a wide pressure range, spanning from 10^{-5}mbar up to 300mbar. For emission line identification and time structure measurements data was taken by high resolution optical spectroscopy using a McPherson 218 monochromator equipped with a S20-cathode photomultiplier. Beam profiles and emission intensities were measured using three different cameras: A regular, cooled CCD camera (Atik 383L+), an Electron Multiplier CCD (EMCCD) as well as an image intensified CCD (iCCD, PiMax4). Specific lines for beam profile images were selected, using optical bandpass filters. The cameras were combined with an f=60mm, broadband (315 to 1100nm) apochromatic lens (Coastal Optics/Jenoptik 60mm f4 Apo Macro). The wavelength dependent photon response function of the cameras was determined, using a PTB-calibrated tungsten strip lamp (OsramWI-17/G 16A). Ion beam currents were continuously measured using the output of a Faraday end-cup. The target cell was pumped down to $<10^{-4}$mbar before applying a suppressor voltage to the Faraday cup and reading the actual ion beam current. No suppressor voltage was used during the measurements, and beam current readings thus are considered relative values to be normalized to the readings with suppressor voltage applied. A differential pumping stage (no entrance foil) was used for pressures lower than 1mbar (neon) or 0.3mbar (argon), respectively. A 1.3 mg/cm^2 Ti foil was installed for high pressures to separate the target chamber from the beam line vacuum. The charge state 8+ was selected for S-ions and the accelerator's beam transport system, and used to convert measured electrical current to particle flux for the low pressure range. Using the Ti foil, the average charge state is estimated to be 14+. No further post-stripping within the target cell was assumed due to very low area mass density. Please note that the "effective emission cross section" is given for 87MeV S-ions under the given experimental conditions. For scaling to other ions/energies/charge states/etc., please note that the charge state of the 87MeV S-ions, provided by the Tandem accelerator, is 8+ for the pressure range $p < 0.1$mbar, and is reaching equilibrium charge state 14+ for the pressure range $p > 0.3$mbar.

Target gas pressure was measured by a capacitive pressure transducer (MKS Baratron) for pressures above $5 \cdot 10^{-3}$ mbar, and a thermocouple/ionivac combi-instrument (Bar-ion) for pressures below 10^{-3} mbar. Pressures were cor-rected in the low-pressure mode for target gas response functions of the instruments.

Light emission intensities were mostly recorded using the cameras with illumination time set for appropriate exposure at each pressure. Typical photon intensities for the 740nm filtered Ar-emission, normalized to beam current, are shown in Fig. 1 for a ^{32}S-beam, with respect to target gas pressure. Normalization to target gas density results in apparent emission cross sections, depicted in Fig. 2 for neon, and in Fig. 3 for argon lines, respectively.

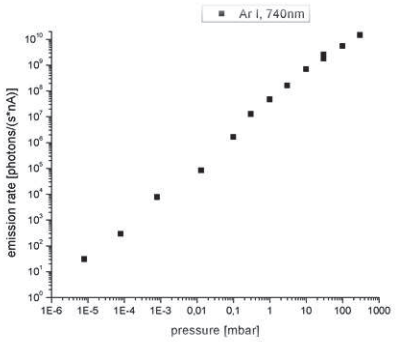

Figure 1: Intensity of photo-emission for the 740nm Ar line, using 87MeV ^{32}S beam excitation.

As depicted in Fig. 2, the 585nm Ne I line is strongly dominated at higher pressures by secondary effects, such as cascades and recombination, and only showing direct excitation behaviour below roughly 10^{-4}mbar.

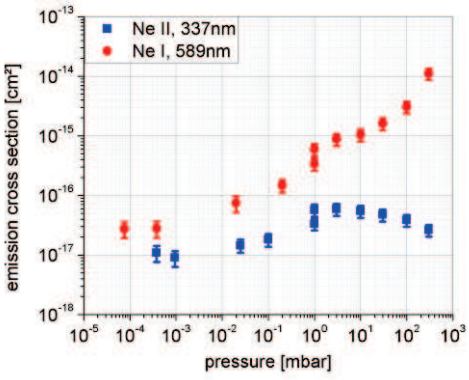

Figure 2: Apparent emission cross section for the 585nm Ne I, and the 337nm Ne II line, using ^{32}S beam excitation.

Depending on the specific levels (e.g. directly connected to resonance states, dipole allowed/forbidden, etc.), quenching of the emission (e.g. Ar 740nm, Fig. 3), or enhancement due to recombination or cascades (Ne 585nm) may occur.

Contrary to neutral line emission, ionic emission from neon and argon (see Fig. 2, 3), represented here by the 3p-3s 337nm (Ne) and 4p-4s 476nm (Ar) lines, shows a relatively constant emission cross section, with slight recombination (0.1 to 1mbar) and collisional quenching, competing with radiative decay, stepping in at higher pressures (>10mbar).

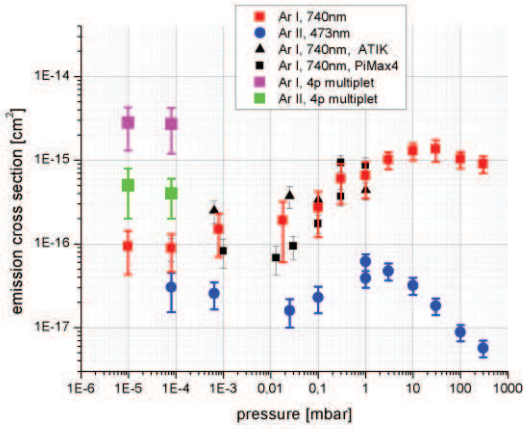

Figure 3: Apparent emission cross section for the total ionic argon 4p-4s multiplet (400-550nm), the 476nm Ar II line, and the 740nm Ar I line, using ^{32}S beam excitation.

Additionally to the ^{32}S-experiments, a proton beam experiment, measuring beam profiles and intensities, was performed. Due to radiation safety, beam current was limited to 8nA, measured at the Faraday end-cup of the target cell. Light emission was consistently low (see Fig. 4), limiting the pressure range to be investigated. Beam profiles and apparent intensities are shown in Fig. 4.

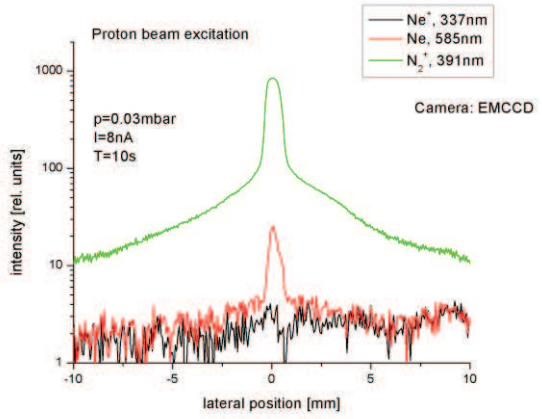

Figure 4: Comparison of beam profiles and emission intensities for the 337nm Ne^+ line (black), the 585nm Ne line, as well as the 391nm N_2^+ emission, using p-beam excitation at 0.03mbar target gas pressure.

The minimum pressure for the neutral 585nm Ne line was 10^{-3}mbar. The 337nm Ne^+ line essentially became invisible already at about 10^{-2}mbar, while the 391nm N_2^+ emission is still strongly pronounced.

Apparent emission cross sections have been derived, as presented in Fig. 5.

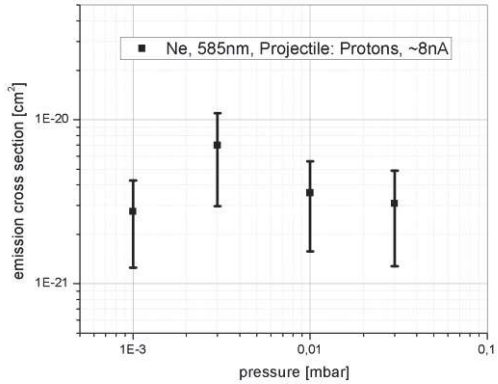

Figure 5: Apparent emission cross section for the neutral 3p-3s 585nm Ne line, using 8nA, 14MeV p-beam excitation.

We assume these to be preliminary data, which - up to now inexplicably - deviate from estimations based on data from [4] and extrapolated to the experimental conditions by Bethe-Born approximation [5].

Also, a small discontinuity in absolute cross section values occurs when taking data with and without Ti-foil (post-stripping), and thus converting electrical current to particle current according to either 8+ or 14+ ions (see e.g. Fig. 2 at 1mbar)

References

[1] P.Forck et al., GSI-FAIR SCIENTIFIC REPORT 2017, p.394,
[2] S. Udrea et al., Conf. Proc. IBIC 2017, p. 359.
[3] C. Andre et al., Conf. Proc. IBIC 2014, p. 412 and references therein,
[4] M. Eckhardt et al., Z. Phys. **A 292**, 337 (1979)
[5] M. Inokuti, Rev. Mod. Phys. **4**, 297 (1971)

Acknowlegement
This work has been funded by the BMBF project APPA R&D, FKZ 05P15WOFA1, GSI Vorhaben TUM ULRI1719, and Maier Leibnitz Labor München (MLL).

Characterisation of Electrons from Relativistic Laser-Produced Plasmas by means of Thermoluminescence Detector-based 10-channel Spectrometer

N. Zahn[1], O. Rosmej[1,2] , F. Horst[2,4], A. Sokolov[2], Ş. Zähter[1], T. Radon[2], I. Dinescu[5], N. Borisenko[3], J.Jacoby[1]

[1] Institute for Applied Physics, Goethe University, Fankfurt, Germany; [2] GSI Helmholtzzentrum für Schwerionenforschung, Darmstadt, Germany; [3] Lebedev Physical Institute, Moscow, Russia; [4] Justus-Liebig-University, Giessen, Germany; [5] Horia Hulubei National Institute for R&D in Physics and Nuclear Engineering, Bucharest, Romania

Interaction of a relativistic sub-picosecond laser pulses with extended, sub-mm long near critical electron density (NCD) plasmas ensures a long acceleration path of electrons and consequent effective coupling of the laser energy with fast MeV energetic electrons. Low density polymer foam layers (2mg/cc Triacetate-Cellulose $C_{12}H_{16}O_8$) with a thickness of 300 and 500 µm were used as targets to create such type of hydrodynamic stable, large scale, quasi-homogeneous plasmas.

The experimental results on the electron heating by a 80-100J, 750 fs short PHELIX-laser pulse of 2-5×10^{19} W/cm^2 intensity demonstrated that effective temperature of supra-thermal electrons increased from 1.5-2 MeV, in the case of the relativistic laser interaction with a metallic foil at high laser contrast, up to 13 MeV for the laser shots onto pre-ionized foam layer with a near critical electron density. Measurements showed high directionality of the acceleration process.

The observed with the electron spectrometers tendency towards the strong increase of the mean electron energy and a number of MeV laser-accelerated electrons is reinforced by the results of the gamma-yield measurements. For measurements of the gamma bremsstrahlung spectra, 10 channels TLD detector-based thermoluminescence dosimetry method was applied. The spectrometer is designed for an energy range from 30 keV to 100 MeV [1].

In the case of laser interaction with long-scale NCD-plasmas, the dose caused by the gamma-radiation measured in the direction of the laser pulse propagation showed a 1000-fold increase compared to the high contrast shots onto plane foils and doses measured perpendicular to the laser propagation direction for all used combinations of targets and laser parameters [2].

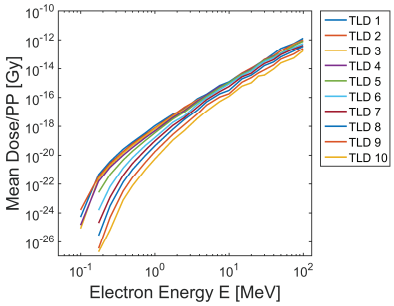

Figure 1: Simulated response-functions of the 10 TLD-channels in the spectrometer to an electron radiation

Figure 1 shows the response functions of the spectrometer to monoenergetic electron radiation in the energy range of 100 keV - 100 MeV which have been simulated using the Monte Carlo code FLUKA [3] as dose values in the TLD detectors placed in a stack of different materials. Different gradients and thresholds of these response-functions allow performing of the reconstruction (unfolding) of the electron spectra.

The evaluation of the electron spectra from the readings of 10 TLDs was resolved in 20 energy bins and was performed applying an unfolding algorithm based on a sequential enumeration of matching data series of the dose values measured by the dosimeters and calculated by means of FLUKA-simulations.

The electron distribution functions were found to be described by two temperature Maxwellian distributions. Figure 2 shows the resulting values of electron temperatures T_{e1} and T_{e2} for selected laser shots: $N°$ 31, 34, 38, 44 were made onto pre-ionized foam and 16, 25, 28, 37 onto foil/foam at the highest laser contrast. In the case of the laser interaction with pre-ionized foams, when the TLD doses reached their maximum values, both electron temperatures are essentially higher compared to T_{e1} and T_{e2} evaluated for the case of high contrast shots.

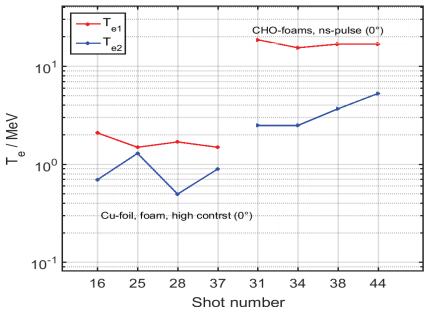

Figure 2: Electron temperatures evaluated from the measured TLD-doses

These results represent a very good correlation with the experimental conditions and with the results of the electron spectrometers. In the case of pre-ionized foams the obtained values for $T_{e1} \simeq$ 12 MeV and corresponding absolute numbers of electrons N_{e1}= 0.5-1×10^{10}. This number corresponds to 8-16 nC of the well-directed super-ponderomotive electron beam.

References

[1] F. Horst *et al.*, NIM A **782** (2015) p. 69-76
[2] O. Rosmej *et al.*, 2019 *New J. Phys.* https://doi.org/10.1088/1367-2630/ab1047
[3] A. Ferrari *et al.*, CERN–2005–10 (2005), INFN/TC 05/11, SLAC–R–773

First-Principles Method for X-ray Thomson Scattering

Wei Kang[*1,2], *Chongjie Mo*[†1,3], *Zhenguo Fu*[4], *Ping Zhang*[1,4], *and Xiantu He*[1,4]

[1]HEDPS, Center for Applied Physics and Technology, Peking University, Beijing, China; [2]College of Engineering, Peking University, Beijing, China; [3]School of Physics, Peking University, Beijing, China; [4]Institute of Applied Physics and Computational Mathematics, Beijing, China

Introduction

We provide a first-principles method to calculate x-ray Thomson scattering (XRTS) spectra of warm dense matter (WDM), with inelastic and elastic signals treated individually using perturbative time-dependent density functional theory (TDDFT) formula and first-principles molecular dynamics (FPMD) simulations, respectively. As an example of the method, calculations of isochorically heated beryllium (Be) are compared carefully with experimental data. A satisfactory agreement is observed, which strongly suggests our method a valid tool to predict XRTS in warm dense states. We also apply the method to the calculation of XRTS of isochorically heated aluminum (Al) foils. Experiments of the same setting are carried our recently with x-ray free electron lasers as both heating source and probe. However, the predicted electronic temperature (T_e) is less than 2 eV, which is much lower than the previous estimation of 6 eV.

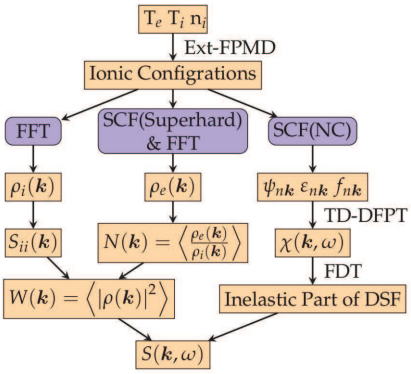

Figure 1: Procedures of calculating total electron dynamic structure factor (DSF)

Results and Conclusion

Figure 1 displays the flow chart of the first-principles method. It shows that with the help of our newly developed extend FPMD method[1], the method can be naturally generalized to calculate XRTS of hot dense plasmas. XRTS calculations of isochorically heated Be is displayed in Fig. 2. Two calculations with all electrons and only valence electrons included respectively are compared with experimental data. It shows that with all electrons considered, the calculation agrees well with experimental data.

* weikang@pku.edu.cn
† mochongjie@pku.edu.cn

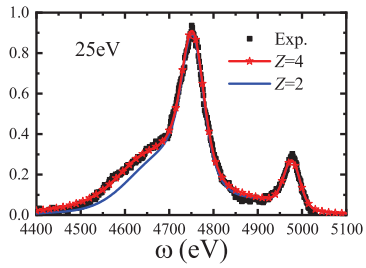

Figure 2: XRTS calculation of Be at 25 eV compared with measured spectrum[2]. Calculation with 4 (all electrons) and 2 (valence) electrons are presented.

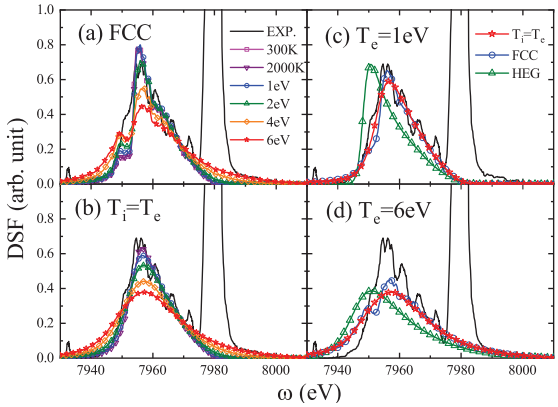

Figure 3: Calculated inelastic parts[4] of DSF together with deconvolved XRTS spectrum[3]. The TDDFT results in (a) an FCC Al lattice at T_e ranging from 300 K to 6 eV and (b) melted Al at T_i = T_e from 2000K to 6 eV. The effects of ions are displayed in (c)/(d) with T_e = 1/6 eV, for FCC Al, molted Al and homogeneous electron gases.

Temperature Estimations of isochorically heated Al are shown in Fig. 3. The TDDFT based perturbation method affords a reasonable estimation to the position of plasmon profile, as shown in the figure, which implies that the main part of ion-electron interactions are well addressed. With the calculation, T_e is determined no more than 2 eV, as long as internal equilibrium among electrons is assumed.

References

[1] S. Zhang et al., Phys. Plasmas, **23**, (2016) 042707.

[2] S. H. Glenzer et al., Phys. Rev. Lett., **90**, (2003) 175002.

[3] P. Sperling et al., Phys. Rev. Lett., **115**, (2015) 115001.

[4] C. Mo et al., Phys. Rev. Lett., **120**, (2018) 205002.

Ab-initio dielectric response function of diamond and other relevant high pressure phases of carbon

K. Ramakrishna[*1,2] *and J. Vorberger*[1]

[1]Helmholtz-Zentrum Dresden-Rossendorf, Bautzner Landstraße 400, 01328 Dresden, Germany; [2]Technische Universität Dresden, 01062 Dresden, Germany

Introduction

The description of the electronic and ionic properties, of the equation of state (EOS), and the corresponding phase boundaries requires state of the art ab-initio methods such as density functional theory (DFT) with molecular dynamics or path integral Monte Carlo. A combination of DFT and many-body quantum statistics allows to include higher order correlations and describe new physics such that the accuracy and predictive power is enhanced. We are particularly interested in the dynamic structure factor (DSF) as it is an important quantity to determine WDM properties and can be accessed using energetic x-ray free-electron (XFEL) radiation or electron beams. Enhanced DSF models include electron-hole interactions in semiconductors and insulators. This provides superior dielectric functions and conductivities, especially when it is combined with higher rungs of xc-functionals for a better description of the band gaps. From these, better EOS may be derived based on the DSF/dielectric function. Furthermore, temperature measurements via x-ray Thompson scattering (XRTS) will be improved. We show the capabilities of reproducing the q-dependent x-ray scattering spectra in comparison with the existing Kubo-Greenwood formula + Mermin approach [1].

Computational details

The Kubo-Greenwood (KG) formula used ubiquitously under WDM conditions for linear response calculations of the dielectric function and conductivity generally provides results of unknown accuracy only, especially for (partially) bound state systems due to the combination of single state DFT wavefunctions along with the lack of many-body physics in the formula itself. The KG expression for the frequency dependent conductivity tensor depends on the derivative of the wavefunction along with the Fermi-Dirac occupations and the single-particle eigenvalues.

To calculate response functions beyond the level of the KG formula, we employ various many-body methods that take wavefunctions from DFT as input. The time-dependent DFT (TDDFT) calculations under adiabatic local density approximation (ALDA) for the xc kernel are performed using Bootstrap, a long range xc kernel, which is reasonably good for reproducing excitonic effects and computationally fast for ab-initio calculation of absorption spectra [2]. Random phase approximation (RPA) uses electron states from DFT, but lacks the xc kernel as used in TDDFT. RPA provides the next best approximation to the Hartree-Fock approximation, representing a change in electron's self-energy due to dynamical screening. The solution of the Bethe-Salpeter equation (BSE) provides the only "exact" description of electron-hole correlations including excitons within the gap. The solution encompasses a two-step process where the quasiparticle electron states and wavefunctions calculated under the GW approximation are used to solve the BSE using a four-point polarization propagator in a Dyson-like equation [3]. In contrast, TDDFT uses two-point propagators and is much easier to solve.

The extended Mermin ansatz (MA) by Fortmann et. al. provides the state of the art description of the free electron feature of the scattering signal in WDM [4, 5]. It allows the study of electron-electron correlations and also the influence of electron-ion collisions by the inclusion of dynamical collision frequency and local field corrections. The absorption spectra obtained with the aforementioned methods for the body-centered cubic structure (bc8) are shown in Fig. 1.

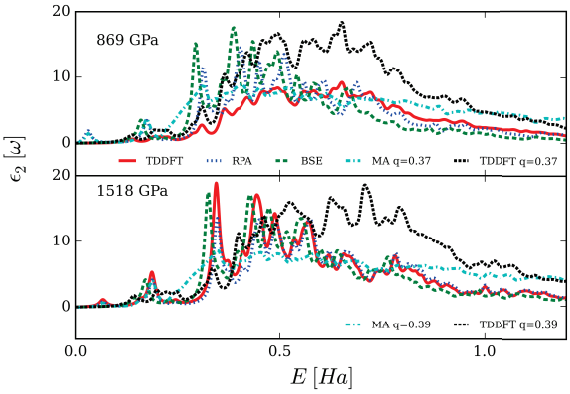

Figure 1: The imaginary part of the dielectric function of bc8 for various pressures calculated using different methods.

References

[1] K. Ramakrishna and J. Vorberger, arXiv:1809.06768 (2018)

[2] S. Sharma et al., Phys. Rev. Lett. 107, (2011) 186401

[3] E. E. Salpeter et al., Phys. Rev. 84, (1951) 1232

[4] N. D. Mermin, Phys. Rev. B 1, (1970) 2362

[5] C. Fortmann et al., Phys. Rev. E 81, (2010) 026405

* k.ramakrishna@hzdr.de

Dispersion relations for the surface wave and the Brewster wave on a surface of a highly absorbing medium

S. P. Sadykova[† 1]*, A. V. Kukushkin*[‡ 2] *, and A. A. Rukhadze*[3*]

[1]Forschungszentrum Jülich, Jülich, Germany; [2]Nizhny Novgorod State Technical University, Nizhny Novgorod, Russia; [3]Prokhorov General Physics Institute of RAS, Moscow, Russia

The Brewster windows are a widely applied diagnostics tool for the fusion plasma diagnostics. Till nowadays the nature of Brewster waves is not quite well understood. It is also well known that the global radiocommunication is realized with the help of ionosphere or, in other words, in a spectrum of higher order Electromagnetic waves inside the spherical screened waveguide where one of the wall is the Earth surface and another one is the ionosphere. Another hypothesis for propagation of signals is based on the surface wave propagation along the seawater and the ground known as **Zeneck wave**[1]. All the theoretical researches in this field are addressed to those surface waves which have the phase velocity being less than speed of a light. In this work we consider the possibility of existence of the leaky wave near to the medium surface with phase velocities higher than speed of a light.

Dispersion relations for the surface wave (SW) and the Brewster wave (BW) propagating along $Z > 0$ axis on a surface of a highly absorbing medium ($X = 0$) have been derived. It is known that the **surface wave** exists in a range of phase velocities **less than speed of a light** in a vacuum and decays while propagating off the medium surface in both directions [2], [3]. Whereas in a range of phase velocities **higher than speed of a light**, the leaky wave does exist in a narrow angular sector which is compressed to the surface and propagates along the surface decaying slowly. We call such a leaky wave as **the Brewster wave** since it can exist only when the transverse incident wave gets not reflected at the surface. This wave can exist compared to the Zeneck wave which can not as it was shown in [4] because its group and phase velocities are higher than that of a light. In this work the Fresnel task of reflection of the plane electro-magnetic wave at the flat conducting surface with $|\varepsilon(\omega)| \gg 1$ ($\varepsilon = \varepsilon' + i\varepsilon''$) was solved, where $\mathrm{Im}\,\varepsilon = \varepsilon'' \gg \varepsilon'$.

In the work [2] the following reflection coefficient was obtained:

$$R = \frac{\varepsilon(\omega)\sqrt{k_z^2c^2-\omega^2} - \sqrt{k_z^2c^2-\varepsilon(\omega)\omega^2}}{\varepsilon(\omega)\sqrt{k_z^2c^2-\omega^2} + \sqrt{k_z^2c^2-\varepsilon(\omega)\omega^2}} \qquad (1)$$

We consider that the field decays in both outward from the medium surface direction, i.e. over the surface at $X > 0$ - $\mathrm{Re}\,k_{x1} = \mathrm{Re}\sqrt{k_z^2-\omega^2/c^2} > 0$ and under the surface at $X < 0$ - $\mathrm{Re}\,k_{x2} = \mathrm{Re}\sqrt{k_z^2-\varepsilon(\omega)\omega^2/c^2} > 0$, and this absorption is strong due to $\varepsilon''(\omega) >> 1$. The solution for Maxwellian equations for the surface E-wave (E_x,E_z,B_y) is the following:

$$E_z, B_y = E_{z0}\cdot, B_{y0}\cdot \begin{cases} \exp\left(-k_{x1}x + ik_z z\right), & x > 0, \\ \mathrm{Re}\,k_{x1} = \sqrt{k_z^2-\omega^2/c^2} > 0, \\ \exp\left(k_{x2}x + ik_z z\right), & x < 0, \\ \mathrm{Re}\,k_{x2} = \sqrt{k_z^2-\varepsilon(\omega)\omega^2/c^2} > 0. \end{cases} \qquad (2)$$

Inserting these solutions into the boundary condition, i.e. continuity, for E_z and B_y at the surface $X = 0$ [3], we can get the dispersion relation for the SW when $\omega/k_z < c$:

$$\varepsilon(\omega)\sqrt{k_z^2c^2-\omega^2} + \sqrt{k_z^2c^2-\varepsilon(\omega)\omega^2} = 0 \qquad (3)$$

and for the wave vector

$$k_z = \frac{\omega}{c}\left(1 + \frac{1}{4\sqrt{\varepsilon''}}\left[i + \frac{\varepsilon'-1}{2\varepsilon''}\right]\right), \qquad (4)$$

where from it follows that the SW is a slow wave and slowly decaying in a highly absorbing media.

The dispersion relation for the Brewster wave (leaky wave), when $\omega/k_z > c$ and no reflection occurs, can be determined in the similar way using the solutions similar to that for the surface wave (2) with the only difference at $x > 0$ the $\exp(-k_{x1}x)$ will turn into $\exp(k_{x1}x)$:

$$\varepsilon(\omega)\sqrt{k_z^2c^2-\omega^2} - \sqrt{k_z^2c^2-\varepsilon(\omega)\omega^2} = 0, \qquad (5)$$

$$k_z = \frac{\omega}{c}\left(1 + \frac{1}{4\sqrt{\varepsilon''}}\left[\imath - \frac{\varepsilon'-1}{2\varepsilon''}\right]\right). \qquad (6)$$

It can be clearly seen that the phase velocity of a BW is higher than that of a speed of a light when $\varepsilon' > 1$. The BW decays slowly along the propagation.

References

[1] J. Zenneck , Ann.Phys 328 (1907) 846.

[2] Gusejn-Zade N.G, A.V. Kukushkin, A.A. Rukhadze, "Fresnel Task and surface waves", Bulletin of the Lebedev Physics Institute 43, Nr.6 (2016) 199-202.

[3] A.F. Alexandrov, L.S. Bogdankevich, A.A. Rukhadze, "Principles of Plasma Electrodynamics", Heidelberg, Springer, 1984.

[4] A.V. Kukushkin, A.A. Rukhadze , K. Z. Rukhadze, "On the existence conditions for a fast surface wave", Physics-Uspekhi 55, Nr.11 (2012) 11241133.

* To the great memory of Prof. Anri A. Rukhadze

† saltanat.sadykova@gmail.com

‡ avkuku@gmail.com

Dynamical properties of dense one-component plasmas revisited*

I.M. Tkachenko[1,#], Yu.V. Arkhipov[2], A.B. Ashikbayeva[2], A. Askaruly[2], A.E. Davletov[2], D.Yu. Dubovtsev[2], S.A. Syzganbayeva[2]

[1]Universitat Politècnica de València, Valencia, Spain; [2]Al-Farabi Kazakh National University, Almaty, Kazakhstan

Dense one-component plasmas are good model systems possessing basic properties of the working bodies of future inertial fusion devices. Contemporary methods of diagnostics of such systems require knowledge of dynamic characteristics of these Coulomb, though classical, systems.

Here, the results on the OCP dynamic properties calculated within the simplified interpolation version of the moment approach are compared to the simulation data of [1]. Thus, the robustness of the self-consistent method based on sum rules and other exact relations, see [2, 3] and references therein, is demonstrated.

Classical one-component Coulomb system are characterized by a coupling parameter

$$\Gamma = \frac{\beta (Ze)^2}{a}. \qquad (1)$$

Here β^{-1} stands for the temperature in energy units, Ze designates the ion charge, and $a = (3/4\pi n)^{1/3}$ is the Wigner-Seitz radius with n being the number density of charged particles.

Plasma is considered to be strongly coupled if $\Gamma > 1$ and is ideal for $\Gamma << 1$. The upper limit of the coupling parameter is determined by the Wigner crystallization.

The interparticle interaction is described by the Coulomb potential:

$$\varphi(r) = \frac{(Ze)^2}{r}, \qquad (2)$$

The central characteristic of dynamic properties of plasmas is the dynamic structure factor (DSF) $S(k,\omega)$, a positive frequency function, which is associated with the dielectric function $\epsilon(k,\omega)$ via (the classical version of) the fluctuation-dissipation theorem):

$$-\frac{Im\ \varepsilon^{-1}(k,\omega)}{\omega} = \frac{(2\pi Ze)^2 \beta}{k^2} S(k,\omega). \qquad (3)$$

Here, the wavenumber k (the system under consideration is presumed to be uniform) is a parameter.

The plasma inverse dielectric function (IDF), $\varepsilon^{-1}(k,\omega)$, was determined in [1] within the moment approach [4] complemented by some physical observations which permitted to express it in terms of only two characteristic frequencies, which are the ratios of the frequency power moments of the IDF imaginary part:

$$\varepsilon^{-1}(k,\omega) = 1 + \frac{\omega_p^2 \left(\sqrt{2}\omega_1 \omega + i\omega_2^2\right)}{\sqrt{2}\omega_1 \omega \left(\omega^2 - \omega_2^2\right) + i\omega_2^2 \left(\omega^2 - \omega_1^2\right)}. \qquad (4)$$

The frequencies ω_1 and ω_2 in (4) can be calculated rigorously as soon as we know the static structure factor (SSF) of the system [1, 4]. Here we employ the following interpolation expressions [5,6]:

$$\omega_1^2 = \omega_1^2(k) = \omega_p^2 \left(1 + k^2 k_D^{-2} + k^4 k_q^{-4}\right), \qquad (5)$$

$$\omega_2^2 = \omega_2^2(k) = \omega_p^2 \left(1 + \frac{\langle v_e^2 \rangle k^2}{\omega_p^2} - \frac{v_{int}^2 k^2}{\omega_p^2}\right). \qquad (6)$$

The interpolation and fitting parameters introduced here are the following:

$$v_{int}^2 = -\frac{4}{15}\frac{\Gamma^{\frac{3}{2}}}{\beta m_e}\left(\frac{-0.9052}{\sqrt{0.6322+\Gamma}} + \frac{0.27243}{1+\Gamma}\right),$$

$k_q^4 = 12 r_s / a^4$, $r_S = a/a_B$, k_D^{-1}, *and* a_B are the Debye and Bohr radii. Under the thermodynamic conditions we deal with here, the system is practically a classical plasma so that all magnitudes can be expressed in terms of the plasma coupling parameter Γ, and we may use for the average electron thermal velocity the Vlasov classical form: $\langle v_e^2 \rangle = 3 k_B T / m_e$.

The numerical results on the dynamic structure factor are compared to the simulation data of [1] and are summarized in Figures 1-6. In all figures the squares correspond to the data of [1] with q=ka being the dimensionless wavenumber.

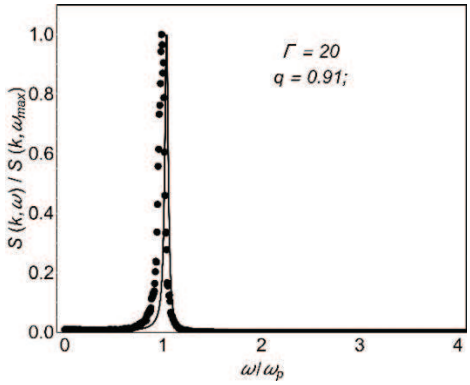

Figure 1: The OCP normalized dynamic structure factor (lines) in comparison with the simulation data of [1] (points) at Γ=20, q=0.91.

* Work supported by Ministry of Education and Science, Kazakhstan Grants AP05132333 and BR05236730.

imtk@mat.upv.es

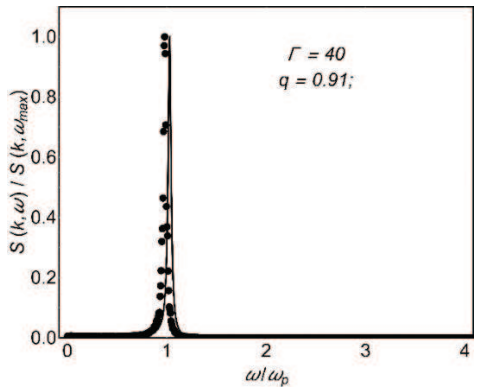

Figure 2: As in Fig.1 but for Γ=40, q=0.91.

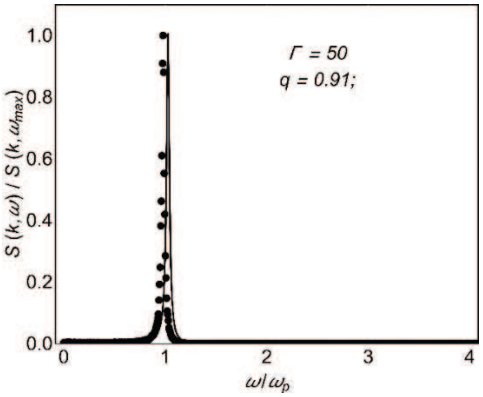

Figure 3: As in Fig.1 but for Γ=50, q=0.91.

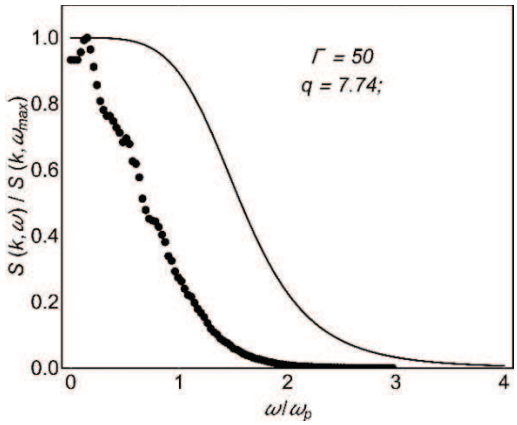

Figure 4: As in Fig.1 but for Γ=50, q=7.74.

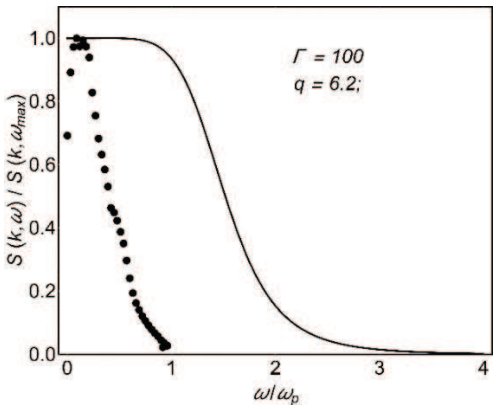

Figure 5: As in Fig.1 but for Γ=100, q=6.20.

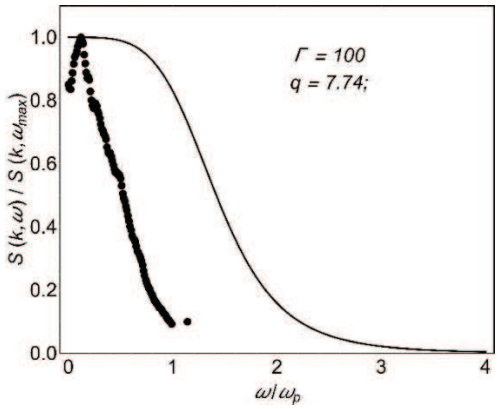

Figure 6: As in Fig.1 but for Γ=100, q=7.74.

In conclusion, the reliability and robustness of the self-consistent moment approach is demonstrated by comparing the results obtained for the OCP dynamic structure factors within the present simplified version of the approach with the simulation data. No adjustment to the latter is employed. Merging of the collective modes at high wavenumbers, when $2\omega_1 < \omega_2$ [1], is described, at least, qualitatively. The method permits to determine also the dispersion and attenuation of plasma waves in plasmas under consideration. Such an outcome can be used in dense plasma diagnostics.

References

[1]. Yu. V. Arkhipov et al., Phys. Rev. Lett., 119, (2017) 045001.

[2]. V. M. Adamyan and I. M. Tkachenko, *Dielectric Conductivity of Nonideal Plasmas*, Lectures on Physics of Nonideal Plasmas: Part I (Odessa State University, Odessa, 1988) in Russian; V. M. Adamyan and I. M. Tkachenko, Contrib. Plasma Phys. 43, 252 (2003).

[3]. S. V. Adamjan and I. M. Tkachenko, Ukr. J. Phys. 36, 1336 (1991)

[4] Igor M. Tkachenko, Yu.V. Arkhipov, A. Askaruly. The Method of Moments and its Applications in Plasma Physics (Lambert, Saarbrücken, 2012) 125 pp.

[5] V.M. Adamyan, I.M. Tkachenko, High Temp., 21 (1983) 307; J. Ortner, I.M. Tkachenko, Phys. Rev. E 63 (2001) 026403.

[6] G. Chabrier, A.Y. Potekhin, Phys. Rev. E 58 (1998) 4941.

2 FAIR related Issues of HED/WDM - Research for Phase-0 and Day-1

A High-Energy Laser Beamline for plasma physics experiments – from PHELIX to the HHT-cave at GSI

Zs. Major[1,2], P. Neumayer[1], U. Eisenbarth[1], B. Zielbauer[1], V. Bagnoud[1,2]
[1]GSI Helmholtzzentrum für Schwerionenforschung GmbH, Planckstraße 1, 64291 Darmstadt, Germany; [2]Helmholtz-Institut Jena, Fröbelstieg 3, 07743 Jena, Germany

Motivation

At the GSI Helmholtzzentrum für Schwerionenforschung (Darmstadt, Germany) one of the unique features of the infrastructure and facilities is the possibility to carry out experiments combining the heavy-ion beam of the accelerator

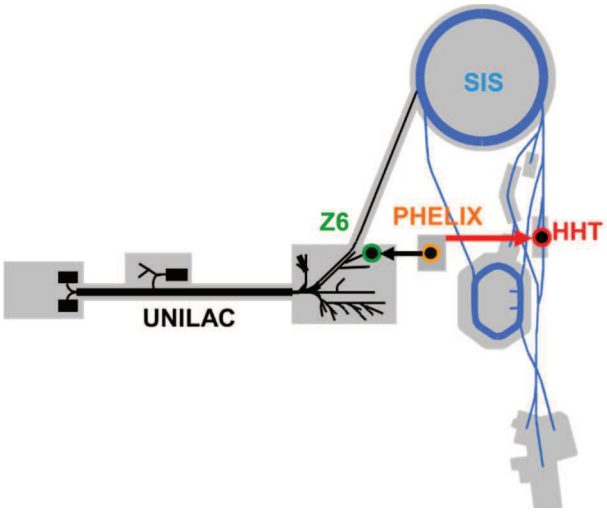

Figure 1: Location of existing infrastructure at GSI, similar to the beamline to the experimental station Z6 the PHELIX long-pulse beam will be transported to the HHT experimental cave located downstream of the SIS18 ion synchrotron.

with the high-power laser PHELIX [1]. PHELIX is a multi-100 J-class glass laser operated as a user facility open to the international scientific community. Through its versatile front-end architecture PHELIX can be operated in both long and short pulse modes, corresponding to ns pulses with up to 1 kJ pulse energy and sub-ps, 200 J pulses, respectively. The short-pulse mode is an ideal driver for the investigation of high-power laser-matter interaction, with the emphasis on driving high-energy secondary sources of ions, neutrons and electrons [2]. The long-pulse mode is mainly used for plasma heating, which can then be investigated by the heavy-ion beam of the linear accelerator of GSI at the experimental station Z6 [3] (cf. Fig. 1) or other diagnostic laser beams.

On the other hand following the linear accelerator, the ions are coupled into the SIS18 ion synchrotron and are further accelerated. The SIS18 ring has recently been upgraded in preparation for seeding the future SIS100 ring of FAIR. The ion beam coming from the SIS18 accelerator ring is sufficiently intense to generate interesting uniformly heated plasma states on the order of several mm in size. For the characterization and investigation of the processes taking place in such a plasma, a laser-driven X-ray backlighter source is very attractive. However, since currently there is no such possibility at GSI, in spite of all necessary facilities being available on site, our plans are to build a new beamline infrastructure that will transport the PHELIX beam to the HHT cave, located downstream of the SIS18 accelerator ring (cf. Fig. 1) mainly for this purpose.

Infrastructure development

The envisaged laser parameters for the pulse delivered by the new beamline to HHT are 200 J pulse energy, 1 ns pulse duration at 527 nm wavelength. A relay imaging telescope will transport the PHELIX pulses across the ESR experimental hall (cf. Fig.2) covering a distance of ~ 65 m while preserving the beam quality. In order to avoid ionization in air at the telescope focus and the detrimental influence of the unfiltered air on the beam quality, the laser pulses will propagate in a vacuum tube along their entire path between the PHELIX building and the HHT cave.

Experiment plans

The PHELIX pulses will drive X-ray sources which can then be used in several diagnostic schemes, such as absorption spectroscopy, scattering, diffraction and radiography to access the high-energy density plasma states generated

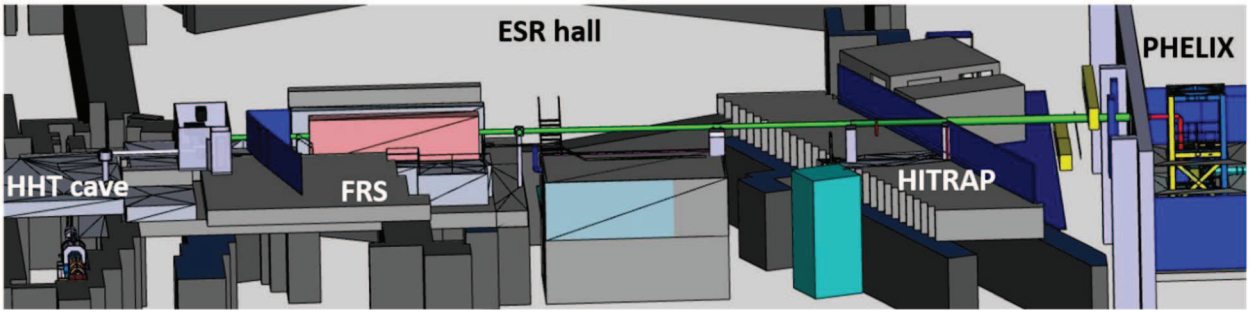

Figure 2: 3D model of the envisaged beamline transporting the PHELIX nanosecond pulses to the HHT experimental cave.

by the high-intensity ion beam. These techniques give information on the electron temperature, the ion temperature and structure, structural phase transitions and plasma expansion characteristics, respectively. In addition to laser-driven X-ray sources, the high-power laser can itself create dynamic states of high energy density matter, which can then be characterized by the proton-radiography capabilities at HHT (PRIOR) [4]. Since these experiments are highly relevant to the research programme planned for the future APPA cave at FAIR, the PHELIX-HHT beamline forms a crucial part of the preparatory "phase-0" activities using existing GSI infrastructure.

References

[1] V. Bagnoud et al., Appl. Phys. B 100 (2010), 137.
[2] L. Antonelli et al., Europhysics Letters 125 (2019), 35002; A. Kleinschmidt et al., Physics of Plasmas 25 (2018), 053101; P. Hilz et al., Nat. Comm. 9 (2018), 423.
[3] W. Cayzac et al., Nat. Comm. 8 (2017), 15693.
[4] D. Varentsov et al., Rev.Sci.Instrum. 87 (2016), 023303.

Development of an Actively Cooled Glass Amplifier at GSI

Marco Patrizio[1], Vincent Bagnoud[2,3], Bernhard Zielbauer[2] and Markus Roth[1,4]

[1]Department of Nuclear Physics, Technical University Darmstadt, 64289 Darmstadt, Germany; [2]Department of Plasma Physics, GSI Helmholtz Centre for Heavy Ion Research, 64291 Darmstadt, Germany; [3]Helmholtz Institute Jena, 07743 Jena, Germany; [4]Facility for Antiproton and Ion Research (FAIR), 64291 Darmstadt, Germany

Background

For plasma physics experiments at FAIR (Facility for Anti-Proton and Ion Research) in Darmstadt, Germany, a new diagnostic laser is needed. This laser is specified with an energy of 200 J at 1053 nm and a repetition rate of at least one shot every 5 minutes. To achieve these goals and using existing know-how at GSI, the main amplifier stage is planned to use Nd:glass as gain medium at an aperture of 315 x 315 mm^2 and the well-established flash lamp pumping technology. Additionally the new amplifier should be compatible with the existing PHELIX laser that can serve as a test bed as well as serving as a potential upgrade.

Development

In the current PHELIX system, thermal loading of the glass is the limiting factor for our repetition rate [1] as the inhomogeneous heat distribution will cause thermal lensing and birefringence effects. These effects strongly affect the wavefront, greatly diminishing the focusability of the beam. To achieve the required repetition rates with such a system, active cooling is required to reduce the heat build-up in the glass discs between shots.

The setup under investigation consists of a split disc design with a liquid coolant film between two glass discs to maximize the surface area of the discs in contact with the coolant while keeping the number of interfaces as low as possible to avoid excessive reflection losses and reduce distortions of the wavefront.

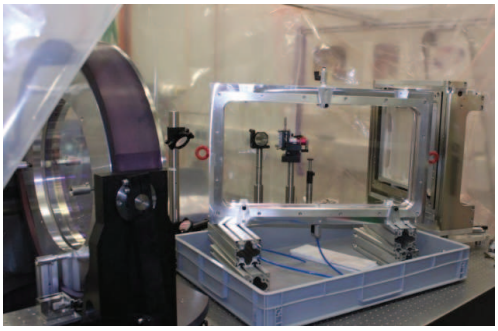

Figure 1: View of the glass module frame on the wavefront measurement bench for initial mechanical and optical tests

Cooling liquid

The cooling liquids investigated for the amplifier play a crucial role in the cooling performance as well as the optical performance of the system. The cooling performance can be characterized by the coolant's heat capacity and its volume exchange rate which is limited by its viscosity. Thus liquids with low heat capacity and low viscosity can be just as viable as liquids with high heat capacity and high viscosity since the higher volume exchange rate can offset the faster increase in coolant temperature. Since the laser beam is passing through the coolant, the optical properties of the coolant have to be considered as well. Optical losses in the amplifier can be divided into absorption and reflection losses which are highly dependent on the absorption characteristics and refractive index of the coolant.

Simulations

After optimizing the coolant flow the simulations were extended to simulate the entire 3D cooling process of the glass discs. From these simulations, it was possible to minimize the cooling time by adjusting the temperature profile of the coolant. The results from these simulations were then processed by a custom C++ script to convert the temperature map of the glass into effective refractive indices. From these indices it was possible to calculate the optical path of each partial beam in the amplifier module resulting in the relative phase shifts and thus the wavefront distortions.

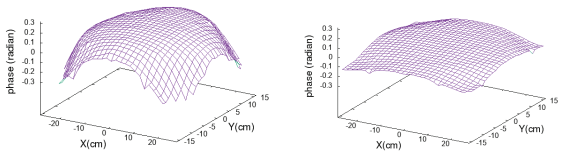

Figure 2: Simulated wavefront deformations. Left: before start of cooling cycle, Right: after 10 min of cooling. Simulations done in CADFEM ANSYS CFD

Status

An optical test bench to measure the wavefront transmitted through a glass module housing two BK7 "dummy" glass discs has been set up. It allows for the verification of the mechanical simulation model as well as a step-by-step implementation of the cooling liquid supply system.

References

[1] D.C. Brown, High-Peak-Power Nd:Glass Laser Systems (Springer, 1981), 1st ed.

Facilities for high energy density experiments at FAIR

S. Neff[*1] *and A. Blazevic*[2]
[1]FAIR, Darmstadt, Germany; [2]GSI, Darmstadt, Germany

At the site of the Gesellschaft fuer Schwerionenforschung (GSI) in Darmstadt, the Facility for Antiproton and Ion Research (FAIR) is currently under construction. FAIR will offer unique experimental possibilities for a wide range of scientific fields, including antiproton experiments, the study of quark-gluon plasmas, nuclear structure studies, atomic physics experiments and high-energy density experiments[1].

High energy density physics research at FAIR

The unique high-intensity heavy-ion beams and high-intensity proton beams that the FAIR facility will offer can be used for the study of high-energy density (HED) samples and warm dense matter (WDM). This research is part of the APPA research pillar, which also includes atomic physics, biophysics and materials science research[2]. Heating with intense heavy-ion beams can be used to generate homogeneous, macroscopic (mm^3-sized) samples of warm dense matter[3]. At FAIR, the SIS-100 heavy-ion synchrotron will provide beams with up to $5 \cdot 10^{11}$ $\mathbf{U}^{28+}$ ions with an energy of 2 AGeV in a 50 ns bunch for plasma physics experiments, where they will be used either to isochorically heat macroscopic samples to eV temperatures or to indirectly compress them to Mbar pressures. In addition, SIS-100 will also provide high-energy protons (up to 10 GeV with up $2.5 \cdot 10^{13}$ protons per bunch in the APPA Cave) which will be used for proton microscopy. This research in the fields of HED physics and WDM is coordinated by the High Energy Density Science at FAIR (HED@FAIR) collaboration, which will focus on four main areas of interest:

1. The study of the properties of materials driven to extreme conditions of pressure and temperature.

2. The study of shocked matter and equations-of-state.

3. The study of the basic properties of strongly coupled plasma and warm dense matter.

4. Nuclear photonics, including the excitation of nuclear processes in plasmas and laser-driven particle acceleration and neutron production.

Key experimental schemes that will be used at FAIR are the HIHEX (*Heavy-Ion Heating and Expansion*)[4], LAPLAS (*Laboratory Planetary Sciences*)[5] and PRIOR (*Proton Microscope for FAIR*)[6] setups.

*The work reported in this paper has been carried out by the research and accelerator departments of GSI and the HED@FAIR collaboration.

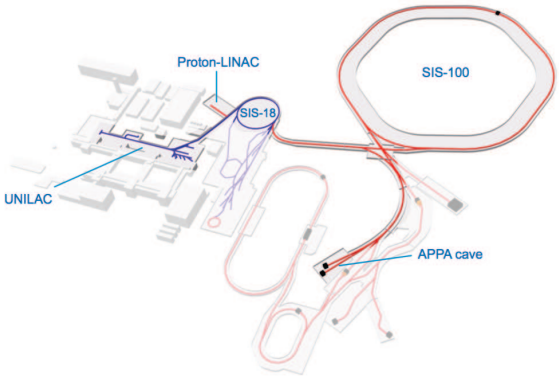

Figure 1: Schematic view of FAIR. The facilities needed for HED and WDM experiments are highlighted. Indicated in blue are facilities already existing at GSI, whereas newly constructed parts are marked in red.

The experimental facilities at FAIR

A schematic of FAIR is shown in Figure 1 (the parts relevant for HED research have been highlighted). Already existing at GSI are the UNILAC linear accelerator and the SIS-18 heavy-ion synchrotron. They will be complemented at FAIR with a proton LINAC and the SIS-100 heavy-ion synchrotron. The beamline for the HED@FAIR experiments are located in the so-called APPA-cave, which also houses a second beamline that is used for atomic physics, biophysics and materials science experiments. The HED@FAIR beamline is shown in Figure 2. Key components are: (i) the beam matching section, (ii) a variable section that can be changed to house setups for various experiments (HIHEX, LAPLAS or PRIOR), (iii) a superconducting final focusing system, (iv) a target chamber and (v) a beam transport line for a diagnostic laser. The ion-optical design of this beamline allows for an efficient transport of a wide variety of ions, ranging from protons to uranium ions. Experiments will use a variety of diagnostics. For laser-based diagnostics, a 100 J, 2ω (532 nm) ns-laser will be available initially. In the long run, it is planned to upgrade to a picosecond short-pulse laser system to allow for better diagnostics of dense samples.

Current status and timeline

Experiments at FAIR are scheduled to start in 2025. Upgrades to the SIS-18 building to improve its radiation shielding and to build the connection to SIS-100 have already been carried out successfully. The construction of the SIS-100 accelerator tunnel is progressing rapidly and the civil construction of the other buildings is scheduled to

start next year and to be finished by 2023. After the installation of components in 2023 and 2024, the commissioning of FAIR is scheduled for 2025. Most accelerator components are currently under construction or have already been delivered. All technical design reports needed for the HED@FAIR setup have been approved by FAIR and the construction of equipment is progressing well.

The building plans for the APPA cave and its support building have been completed and the specifications of the technical building equipment are currently being finalized, so that the civil construction work can be tendered once it has been approved by the FAIR Council. There has also been a review of several experiment components by the Cost Book Working Group. In the case of HED@FAIR, it has recommended that several work packages (beam dump, beam matching section, cryogenic system) should be part of the accelerator work package (the decision by the FAIR Council on these proposed changes is pending).

The ion-optical layout of the beam matching section has recently been optimized, resulting in three fewer quadrupole magnets that are required and corresponding cost reductions. The ordering of the quadrupole magnets for the beam matching section is scheduled for this year.

The superconducting quadrupole magnets for the final focusing system are an Russian in-kind contribution and have been contracted to the Kurchatov Institute IHEP in Protvino. After a first design had been discussed with accelerator experts at GSI, it had been decided to redesign the current lead connectors. The final magnet design has now been finished and a final design review (FDR) will take place at GSI in June 2019. After the completion of the FDR, the production of the four quadrupole magnets will start. The delivery of the last magnet is scheduled for the spring of 2023.

The electromagnets for PRIOR and their power supplies are a German in-kind contribution and have been contracted to two suppliers. The delivery of the magnets and power supplies is scheduled for the fall of 2019, so that the system can be installed at the HHT experimental area for testing and commissioning in the beam time of 2020.

A target chamber for first experiments and a target manipulator have been funded by BMBF Verbundforschung and will be designed and built by TU Darmstadt and GU Frankfurt in collaboration with GSI. The specifications are currently being finished. It is planned to finish construction by 2020 and install that target chamber at the HHT experimental area in order to test and commission it in 2021.

The diagnostic laser is constructed by the PHELIX laser group at GSI in collaboration with the TU Darmstadt and the FSU Jena. The design for the liquid-cooled main amplifiers with high-repetion rate has been finished and will be tested with a prototype at GSI. The first four (out of eight) glass disks for the main amplifier have passed the factory acceptance test at the supplier. Furthermore, R&D work on the laser frontend is carried out at FSU Jena.

There has also recently an expression-of-interest by the IMP in Lanzhou to provide a SOP pyrometer for diagnostics of HED@FAIR experiments.

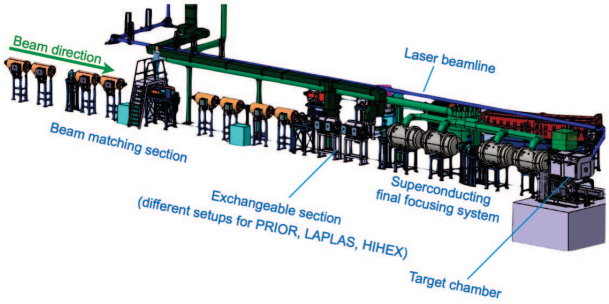

Figure 2: The HED@FAIR beamline in the APPA cave.

Therefore the construction of all components needed for Day-1 experiments in the APPA cave is on track to be ready for installation once the APPA cave is available in 2023.

Experiments at GSI before the start of FAIR

In order to bridge the time gap until the start of FAIR in 2025, scientists can use the upgraded UNILAC and SIS-18 accelerators at GSI in so-called Phase 0 experiments, using the already existing UNILAC and SIS-18 accelerators. These experiments make it also possible to test new detectors and other components that will be used in FAIR experiments. A first round of Phase 0 experiments has already been carried out this year. HED@FAIR will focus on two experiments, PRIOR and HIHEX, that will be carried out at GSI. In the beamtime in 2020, the PRIOR system will be commissioned with static and dynamic targets. A subsequent beamtime with PRIOR is then planned for 2022.

In 2021, first experiments with HIHEX are planned. These experiments will also use a start version of the new target chamber. In addition, a beamline from the existing PHELIX laser to the experimental area at SIS-18 is currently being built, which will allow to use a long-pulse (ns) laser beam in coupled experiments. Even with the limited ion beam intensities available from SIS-18, it will possible to reach temperatures of 1-2 eV in several metals, which makes it possible to study the two-phase region near the critical point[7].

References

[1] M. Durante et. al., Phys. Scr. **94**, 2019, 033001

[2] T. Stöhlker et. al., Nucl. Instr. Meth. B **365**, 2015, 680-685

[3] V.E. Fortov et. al., Phys. Uspekhi **51** (2), 2008, 109-131

[4] N.A. Tahir et. al., Phys. Rev. Lett. **95**, 2005, 035001

[5] N.A. Tahir et. al., Phys. Rev. E **63**, 2000, 016402

[6] D. Varentsov et. al., Rev. Sci. Instr. **87**, 2016, 023303

[7] V.B. Mintsev et. al., Contr. Plasma Phys. **56**, 2016, 281-285

Design of Large Aperture Quadrupole for the HED@FAIR Experiments*

A. Ageev, Y. Altukhov, E. Kashtanov, S. Kozub, L. Tkachenko, S. Zinchenko
NRC "Kurchatov Institute" – IHEP, Protvino, Moscow region, Russia, 142281

Optimization of SC quadrupole design

SC quadrupole magnet design on the basis [1] and superconducting cable dimensions [2] has been calculated. IHEP is developing two types of the end part geometries of SC coil, which is shown in Figure 1 as an involute in the plane $\rho\Theta$-z.

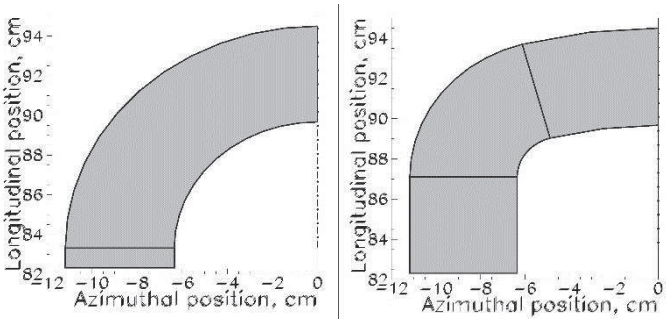

Figure 1: Involutes of the end parts: type 1 is on the left, type 2 is on the right.

The turns on the end parts at $\rho\Theta = 0$ are installed perpendicular to the longitudinal axis Z. The turns in the involute (1) in the plane $\rho\Theta$-Z are bent along the arc of a large radius R, which is equal to the arc length along the outer radius of the layer $R = (r+a)\times(90-\alpha)$, r is the inner radius of the layer, a is thickness of the layer; α is the final angle of the layer. The turns in the involute (2) are bent over a small radius 20 mm at an angle of 75°, then along the conjugate radius to 90°. In the end parts, the longitudinal length of the spacer with width S serves as a parameter for the optimization of the multipole, and to reduce excess field in the end parts. Therefore, there are three coil blocks and eight possible combinations of the end parts. In addition, it is necessary to shorten the iron yoke by ΔL_{Fe} from each end of the coil in order to completely reduce the field excess in the end parts to its value in the central section.

A geometry optimization at the infinite permeability approximation μ and a cylindrical inner radius of the iron yoke was done, using the computer code HARM-3D [3]. Basically, this program uses analytical formulae. In the magnet design, a computer code MULTIC [4] has been employed. This code allows calculating a 3D geometry, taking into account the real dependence of $\mu(B)$ in the iron.

The basic magnetic parameters of the optimized geometry are presented in Table I. The notations in the Table are: B_{max0} and B_{maxe} – maximal field in the central cross section and in the end parts; G_0 – the central gradient; L_{ef} – the effective length of the magnet; I_{op} – the operating current; T_C – the critical temperature of the quadrupole.

TABLE I. Main parameters of 3D geometry.

S, mm	27.89
ΔL_{Fe}, mm	163
B_{max0}, T	5.879
B_{maxe}, T	5.8802
G_0, T/m	37.42
L_{ef}, m	1.764
I_{op}, kA	5.805
T_C, K	5.927

Cooling and heating of SC quadrupole

Heat, which must be withdrawn from the quadrupole in the temperature range of 290-4.5 K, is about $Q = 5.3\ 10^8$ J. This heat will be withdrawn from the quadrupole by two streams of helium: a peripheral flowing through 18 channels with a cross section of 3×18 mm^2 and an internal flow through the annular channel R = 127.5/130 mm. It should be noted, that the total cross-section of the peripheral channel is approximately equal to the cross section of the annular one.

The main quantity of heat of the quadrupole is contained in the iron yoke. The peripheral stream is in direct contact with the iron yoke. Between the inner stream and the iron yoke there are two layers of the superconducting coil with an electrical insulation and a stainless lamination, whose thermal conductivity is much lower than the thermal conductivity of the iron. Therefore, the heat transfer coefficient from iron to the peripheral flow is much larger than the heat transfer coefficient from iron to the inner stream. Consequently, the inner tube R127.5 during cooling, when cold helium is fed to the input of the quadrupole, will cool faster than the outer layer R393. As a result, tensile forces will arise in the inner tube, which, with a certain temperature difference between the outer layer and the inner tube, can cause an irreversible deformation of the inner tube. A similar situation is observed during warming up, when warm helium is supplied to the quadrupole and compressive forces appear in the inner tube.

Calculations have been made to determine the permissible difference between the temperature of the outlet end of the outer layer (To) and of the helium input stream temperature (Ti), at which irreversible deformations in the inner tube do not yet occur. The calculation took into account the provisions of the rules AD2000 and of the European PED [5]. The results of calculations for the inner tube and outer shell of steel 1.4436 are shown in Figure 2.

It is seen from Figure 2 that upon cooling a "warm" (290 K) quadrupole, a stream of cold helium can be fed into with a temperature not lower than 220 K. When the outer layer is cooled to a temperature of 280 K, the temperature of the cooling helium flow at the entrance to the quadrupole can be lowered to 190 K etc. It also follows from Figure 2 that at a temperature of the entire outer layer below 190 K,

* Work supported by the contract "The design, fabrication, transport, assembly, documentation and testing of the Superconducting Final Focusing Quadrupole System of the HEDgeHOB beamline".

a liquid helium stream can be fed to the entrance to the quadrupole.

When heating the "cold" quadrupole, a stream of helium with a temperature no higher than 165 K is initially supplied. When the outer layer is warmed up to 20 K, the temperature of the helium flow at the entrance to the quadrupole can be raised to 170 K, and so on. At an external layer temperature of 245 K, a helium flow can be applied to the entrance to the quadrupole at ambient temperature.

The arguments given above on cooling/heating are valid both for one quadrupole and for a string of four quadrupoles. To control the cooling and heating processes, it is sufficient to know the temperature at three points of the quadrupole: the temperature of the outer layer at the entrance to the quadrupole, the temperature of the outer layer at the exit from the quadrupole, and the temperature of the inner tube at the exit from the quadrupole. As thermal sensors, it is permissible to use platinum thermometers.

Thus, the data of the thermal analysis of the quadrupole design (Figure 2) make it possible to determine the permissible temperatures of the quadrupole and helium flows at the inlet and outlet in the cooling and heating processes. The addition of data on the mass flow rates of helium flows at various temperatures of the "cryogenic plant + local cryogenics" system to these results will allow calculating the cooling and heating times of the quadrupoles.

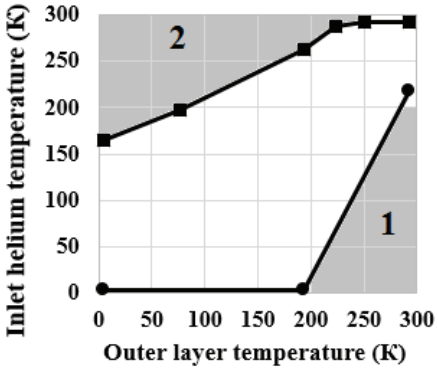

Figure 2: Admissible temperatures of the incoming helium flow T_i when cooling (●) and heating (▪) of the quadrupole as a function of the temperature T_o of the outlet end of the outer layer. The outer shell and the inner tube are 1.4436 steel. 1 - region of unacceptable temperatures of the input helium flow upon cooling. 2 - region of unacceptable temperatures of the input helium flow during heating.

References

[1] "HEDgeHOB SC Quads Detailed Specification", GSI (2016)

[2] News and Reports from High Energy Density generated by Heavy Ion and Laser Beams 2017. GSI-2018-2 Report, July 2018, p.p.13-15.

[3] S.V. Purtov and L.M. Tkachenko. "HARM-3D - a Code to Calculate Magnetic Characteristics of SC Magnets". MT-15, Beijing, China, 1997, Beijing, China, Vol. 1, p.p. 1335-1338.

[4] L.M Tkachenko. Code Package MULTIC for Calculation of Magnetic Field with an Arbitrary Configuration. IHEP preprint 92-28, 1992, 48 pp. (in Russian).

[5] EUROPEAN STANDARD BS EN 10028-7:2016. "Flat products made of steels for pressure purposes" - Part 7: Stainless steels, July 2016

Construction, characterization and optimization of a plasma window for FAIR, status update*

B. F. Bohlender[1#], A. Michel[1], M. Dehmer[1], M. Iberler[1], J. Jacoby[1]

[1]IAP, Goethe University, Frankfurt, Germany

Introduction

The Plasma window is a membrane free beam transition between a region of higher pressure (e.g. Target chamber, gas stripper) and the vacuum of an accelerator. For details on the working principle, the reader is referred to [1], [2], [3].

Experimental results

In comparison to the experimental setup described in the report of last year [4], a new setup featuring an increased aperture of the discharge channel from Ø = 3.3 to 5 mm was developed and tested.

Figure 1 shows a schematic view of the setup including a cross-section of the current window with increased aperture. High pressure side is to the left, as is the cathode.

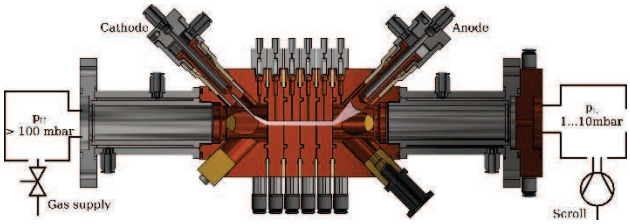

Figure 1: Schematic setup of the experimental setup

The presented data has been collected with a residual gas composed of Ar with 2% H_2. The volume flow ranged from 1 to 4 slm. Currents between 40 A and 60 A have been used. The pressure ranges from 83 mbar to 740 mbar on the high pressure side and from 6.1 mbar to 220 mbar on the low pressure side.

Plasma parameters

Radial spectrometry measurements were carried out along the discharge axis allowing for the simultaneous determination of (radial integrated) plasma parameters. The estimation of the electron temperature yields values between 1.1 eV and 1.2 eV.

Measurements of the electron density were carried out, indicating a strong dependence on the current, pressure, the position inside the discharge channel as well on the volume flow and aperture. Values of n_e vary from $0.09 * 10^{16}$ cm^{-3} to $1.01 * 10^{16}$ cm^{-3} for Ø = 5 mm which shows a decrease of a factor of 4 compared to the values for Ø = 3.3 mm which range from $0.25 * 10^{16}$ cm^{-3} to $4.2 * 10^{16}$ cm^{-3}.

Pressure parameters

The pressure measurements were carried out while holding the pressure on the low pressure side (i.e. pumping side) constant and changing the volume flow on the high pressure side.

The normed pressure quotient q_n, that is p_H over p_L (see Fig. 1.) divided by the pressure quotient q of the plasma window when no discharge is burning, is clearly dependent on the discharge current and on the volume flow. For Ø = 5 mm this quotient ranges from 5.8 to 8 which is below the quotients given for Ø = 3.3 mm, which range up to 12, see Fig. 2.

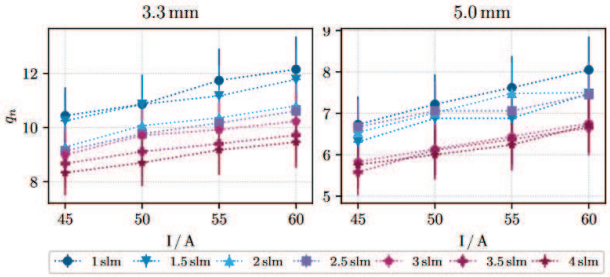

Figure 2: Pressure quotient q_n for different volume flows and currents. Lhs is Ø = 3.3 mm, rhs Ø = 5 mm

The discharge enhances the pressure separation up to a factor of 12 which correlates with the length saving of a sole differential pumping system. Absolute values of the pressure drop increase with increasing current and volume flow.

Conclusion and outlook

The plasma window is operational for well over 10 h now and realizing an improvement in the pressure quotient by a factor of up to 8 for the increased aperture.

In the near future, the complete differential pumping system, including the turbo-stage, will be build and tested. In addition, measurements with 2 to 4 cathodes, higher currents as well as parallel magnetic fields in the discharge column will be carried out to increase the sealing properties for higher apertures.

References

[1] B. F. Bohlender et al GSI HED report 2016
[2] B. F. Bohlender et al GSI HED report 2015
[3] A. Hershcovitch, J. Appl. Phys, 1995
[4] B. F. Bohlender et al GSI HED report 2017

* Work supported by BMBF, Ref.no: 05P15 RFRBA

#bohlender@iap.uni-frankfurt.de

XCOT-system for imaging of the heavy ion beam intensity distribution on target in Phase-0 and at FAIR

O. N. Rosmej[1,2,#], S. Zähter[2] , M. Gyrdymov[2], A. Kantsyrev[3], A. Skobliakov[3], V. Panyushkin[3], A. Bogdanov[3]

[1]Helmholtzzentrum GSI Dartmstadt, Germany, Helmholtzzentrum GSI, Darmstadt, Germany, [2]IAP, Goethe University Frankfurt, Germany, [3] NRC "Kurchatov Institute"-ITEP, Moscow, Russia

In the HIHEX experiment, planned by the HED@FAIR collaboration at FAIR [1], precise knowledge of the energy density distribution deposited by the heavy ion beam into the target is of big importance. The reported experiment U317 was performed in the frame of FAIR Phase-0 at the UNILAC facility at GSI. It was aimed at the development of the FAIR-relevant imaging techniques based on the x-ray target and projectile fluorescence.

The XCOT-system (X-ray Conversion and Transport) is developed at the Goethe University Frankfurt in frame of a BMBF-Project* for application at FAIR, where one expects strong parasitic radiation of particles and gammas capable of destroying the experimental equipment. In the XCOT-concept, the X-ray image of the beam-target interaction region performed by means of a pin-hole or a crystal, is converted by a scintillator into an optical one. The optical image is transported for registration over a meters long distance to the optical detector by using optical fibers or a telescope objective.

In experiment U317, a 11.4 MeV/u Au^{26+} beam was passing through a 10 m thick Cu150-mesh (150 lines per inch). X-ray projectile and target fluorescence that occurs in the interaction region was used for imaging purposes. The 3 mm in diameter Cu-mesh was imaged on to the 100 m thin CsI-scintillator by means of an X-ray pin-hole camera. To increase the signal-to-noise ratio we used a multi-pinhole with 9 holes of 80 μm diameter. Registration was made by means of a sCMOS optical camera with MCP-based image amplifier. The optical image of the Cu-mesh produced at the scintillator was focused at the amplifier phosphor screen by means of the Nikon 80-400 mm objective with Close Up lens. The total distance between the by Au-ions irradiated Cu-mesh and the resulting optical image was around 1m.

Figure 1 a) shows a polychromatic X-ray image of the Cu-mesh irradiated for 10 minutes by Au-ions in the photon energy range above 5 keV obtained by means of the multi-pinhole. Figure 1 b) shows the temporal integration of 18 pictures like in a). Figure 1 c) shows the spatial integration of the six pictures in b). The MTF (modulation transfer function) is about 34% while spatial resolution is about $2\sigma \sim 40$ μm for the obtained image with magnification 1:1. The accumulation time reached 180 min. This corresponds to a number of $10^8 \cdot 180 \cdot 60 = 1.1 \cdot 10^{12}$ Au-ions/mm^2 transmitted through the Cu-mesh with a 30% spacing.

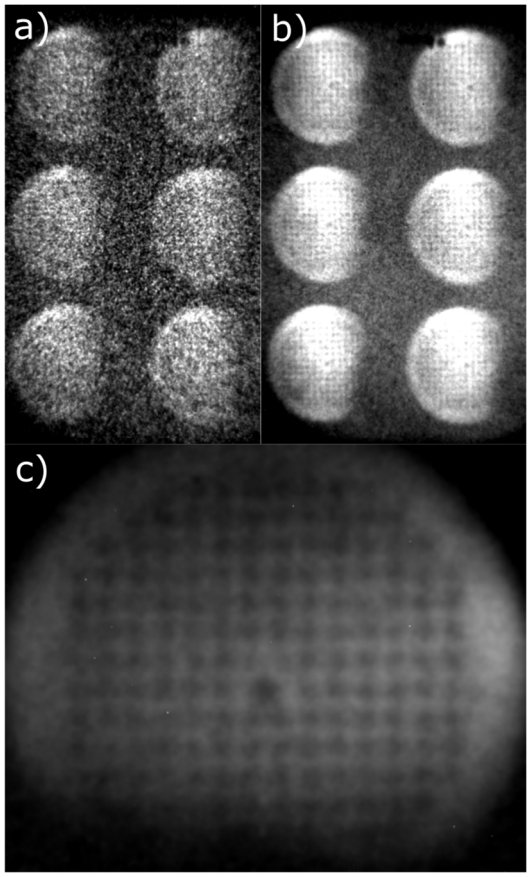

Figure 1: a) Polychromatic X-ray image of the Cu-mesh irradiated by Au-ions with multipinhole, 10 minutes of exposition and registered by means of the XCOT-system (90° rotated). b) Same as a) but 180 minutes exposition. c) Same as b) but sum of six top single pictures as seen in b).

References

[1] V. Mintsev, et al., Non-Ideal Plasma and Early Experiments at FAIR: HIHEX - Heavy Ion Heating and Expansion, Contributions to Plasma Physics, 2016, Vol. 56, I.3-4, pp. 281-285, DOI 10.1002/ctpp.201500105

* Work supported by the BMBF FKz. 05P19RFFA1 project.

#o.rosmej@gsi.de

Numerical simulation of XCOT diagnostic of the heavy ion beam for upcoming HIHEX experiment

A. Skobliakov[1], O. Rosmej[2,3], A. Kantsyrev[1], A. Bogdanov[1], V. Panyushkin[1], D. Kolesnikov[1], A. Golubev[1]
[1] NRC "Kurchatov Institute"-ITEP, Moscow, Russia; [2]Helmholtzzentrum GSI, Darmstadt, Germany; [3]IAP, Goethe University Frankfurt, Germany

In the HIHEX (Heavy Ion HEating and eXpansion) concept, high intensity ion beams are used to heat the target material and to promote phase transitions in unexplored regions of the phase diagram [1]. In these experiments, that will be performed in the frame of HED@FAIR col-laboration during Phase 0 and at FAIR, knowledge about a heavy ion beam cross-profile distribution at target is of big importance. The XCOT diagnostic system (X-ray Conversion to Optical radiation and Transport), developed at the Goethe University Frankfurt, will allow obtaining beam parameters using X-ray fluorescence that occurs in ion beam-target interaction process.

Model of the experimental setup

Numerical modeling plays a crucial role in experimental planning and processing of obtained data. To perform numerical simulation of XCOT diagnostic, the Geant4 toolkit was used. The full-scale model of the experiment U317, which was performed in the frame of FAIR Phase-0 at the UNILAC facility at GSI, was used for simula-tions. In the model, Au^{+26} ion beam with energy of 11.4 MeV/u irradiates Cu-mesh (100 wires per inch) (Fig. 1).

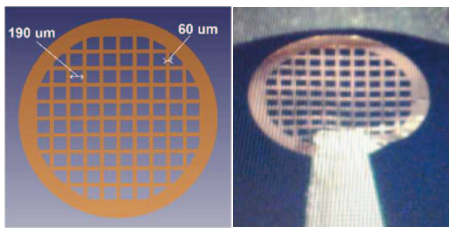

Figure 1: The model of Cu-mesh target in Geant4 (left), experimental target (right)

X-ray image of 3 mm in diameter and 10 um thick mesh was formed by a multi-pinhole with 9 holes of 80 mm in diameter drilled by laser in 75 um thick Ta plate. Distance between holes was 2.5 mm. Such pinhole configuration was used in experiments to increase imaging statistics. The distances between target, pinhole and detector were 65 and 130 mm respectively (pinhole magnification 2:1). In the model, the experimental target chamber was made of stainless steel in form of sphere with inner and outer radius of 0.5 and 0.55 m respectively. An optical aluminum table was set inside the target chamber in order to take into account a potential secondary X-rays and neutrons noise. Also a graphite collimator (inner Ø3.5 mm) was placed in front of the target along the beam as in real experiments. Size of the thin virtual detector was 26x26 mm with 2000x2000 cells, what correspond to the sCMOS optical camera.

Results

The X-ray image of the target was calculated us-ing the full-scale model of experimental setup and multi-pinhole system (Fig. 2, left). Simulation ion statistic is ~ $4*10^{10}$ ions/mm^2, photon statistic at the image is ~ $1.5*10^4$ pht./mm^2. Also the ex-perimental result is present (Fig. 2, right), ions statistic is ~$6*10^{11}$/mm^2.

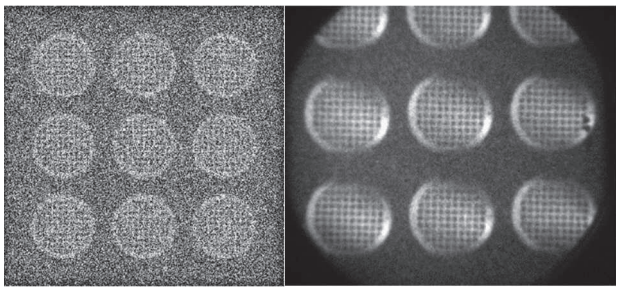

Figure 2: X-Ray images of Cu-mesh target: left - calculated with Geant4, right - experimental image obtained with Au+26 11.4 MeV/u ions.

Fig. 3 shows simulated and experimental mesh-images obtained after folding of 4 images of circles at left bottom corner (Fig.2).

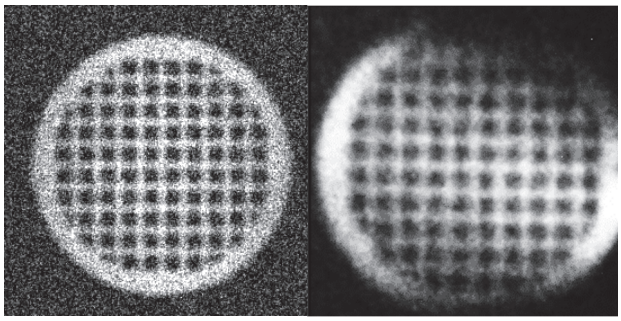

Figure 3: Folded X-ray images: left is the calculated with Geant4, right is the experimental image.

* Work supported by the BMBF FKz. 05P19RFFA1 project
* Work supported by the Ministry of Science and Higher Education of the Russian Federation

#Alexey Kantsyrev [kantsyrev@itep.ru]

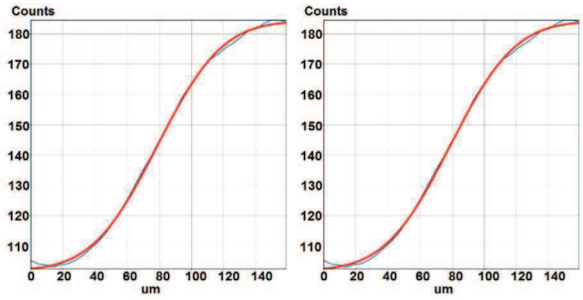

Fig. 4. Horizontal cross-profiles: model (left), experiment (right). Red – is fitting function

The spatial resolutions of images were estimated by fitting of error function on horizontal cross profiles: $\sigma \sim 15$ um for simulated image and $\sigma \sim 30$ um for experimental one (Fig. 4). The difference may be explained as blurring effects in a real detector (CsI). The MTF (modulation transfer function) is about 20% both for experiment and simulation.

References

[1] V. Mintsev, V. at al., Contributions to Plasma Physics, 2016, Vol. 56, I.3-4, DOI 10.1002/

3 Interaction Experiments with Ion- and Laser Beams

Relativistic laser-matter interaction with planar foils at high laser contrast*

Z. Samsonova[1,2,#] , O. N. Rosmej[3,4], S. Höfer[1], D. Kartashov[1], C. Arda[3], D. Khaghani[1], A. Schoenlein[3], S. Zähter[3], A. Hoffmann[1], R. Loetzsch[1,2], A. Saevert[1,2], I. Uschmann[1,2], M. E. Povarnitsyn[5], N. E. Andreev[5,6], L. P. Pugachev[5,6], M. C. Kaluza[1,2], and C. Spielmann[1,2]

[1]IOQ, Abbe Center of Photonics, Friedrich-Schiller-University Jena, Germany; [2]Helmholtz Institute Jena, Germany; [3]GSI, Darmstadt, Germany; [4]IAP, Goethe University Frankfurt, Germany; [5]Joint Institute for High Temperatures of RAS, Moscow, Russia; [6]Moscow Institute of Physics and Technology, Dolgoprudny, Russia.

A significant improvement of the temporal pulse contrast of high-power laser systems has made a remarkable impact on the field of relativistic laser-matter interaction physics. With a high-contrast laser, the pre-plasma formation is strongly reduced and the pulse peak intensity interacts with a sharp density profile. The electron energy distribution function and the hot electron fraction in this case are expected to be very different in comparison with the low-contrast interaction. The resulting plasma parameters and plasma dynamics are subjects of research crucial for better understanding of particle acceleration via radiation pressure [1] and a new regime of interaction with nanostructures [2].

The experiment has been carried out at the Ti:Sapphire laser system JETi-40 (IOQ, Jena) which has an excellent contrast. To improve the contrast further we frequency doubled (@ 400 nm) the laser pulse before focusing onto a 25 µm-thick Ti foil (this thickness ensures no refluxing effect for electrons with energies up to 100 keV). The resulting laser pulse intensity was ~2×10^{19} W/cm^2 with the picosecond pulse contrast of 10^{-9}. The complex diagnostics provided an opportunity to measure X-ray spectra and infer information about different electron fractions in a wide energy range [3].

The Bremsstrahlung emission from the hot electrons traversing the target was measured with the Timepix detector and the spectrum of the run-away electrons characterized with a magnet spectrometer imply a multi-temperature electron energy distribution function. The 3D Particle-in-Cell (PIC) simulations predict up to 4 effective electron temperatures when the peak intensity reaches the target (t=0 fs) (Fig. 1(a)), which agrees with the experimental results.

The total charge of the run-away electrons is estimated to be only 10 pC, which could result in a heating up to tens of eV. However, keV bulk electron temperature Te was retrieved from the K-shell emission spectrum using methods of X-ray spectroscopy (Fig. 1(b)). The simulated emission spectra from the highly charged states (Ti^{19+},Ti^{20+}) obtained with PIC show a good agreement with the experiments for peak values of T_e=1.8 keV and $n_e=2\times10^{23}$ cm^{-3}. However, it was measured [3] that this high-temperature and high-density plasma was generated only within a 150 nm-thick top layer of the target, which is supported by the hydrodynamic simulations. Already ~200 fs after the interaction, the deposited energy is distributed by the heat wave over a larger volume where the electron temperature drops below 1 keV.

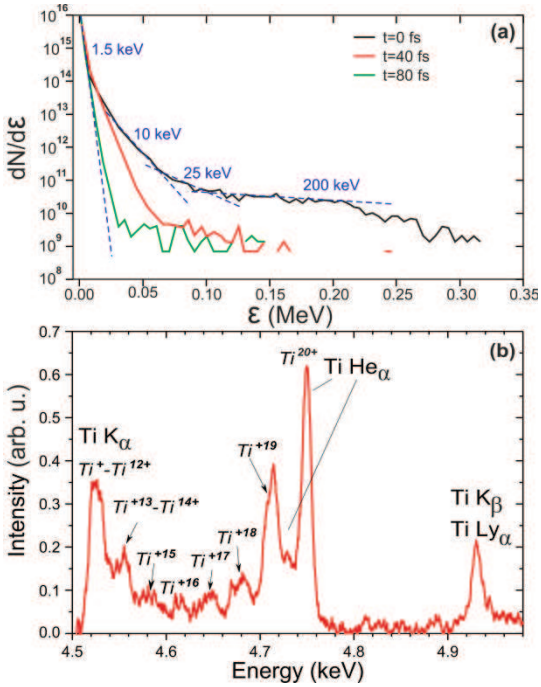

Figure 1: (a) Simulated electron energy spectra at different time steps of the interaction. (b) K-shell emission spectrum from a Ti foil.

The generation of keV-hot bulk electrons can be explained by the collisional mechanism of the laser energy absorption in plasmas with a nearly step-like electron density profile. The laser energy is first deposited into the nm-thin skin-layer and then transported deeper via the electron heat transport. This scenario is opposite to the volumetric heating with supra-thermal electrons, which production was strongly suppressed in the high-contrast interaction.

References

[1] M. Kaluza et al., "Influence of the laser prepulse on proton acceleration in thin-foil experiments", Phys. Rev. Lett. 93, 045003 (2004).

[2] Z. Samsonova et al., "X-ray emission generated by laser-produced plasmas from dielectric nanostructured targets", AIP. Conf. Proc. 1811, 180001 (2017).

[3] O. N. Rosmej et al., "Generation of keV hot near-solid density plasma states at high-contrast laser-matter interaction", Phys. Plasmas 25, 083103 (2018).

* Work supported by the by the BMBF FKz. 05P15SJFA1 and 05P15RGFAA projects.
The report is also submitted to the HI Jena Annual Report 2018.
zhanna.samsonova@uni-jena.de

Ion Source Perturbation and Control in Intense Laser Plasma Interaction

S. Krishnamurthy[1], M. Tayyab[2], K. Makur[1], S. Bagchi[2], T. Mandal[2], J.A. Chakera[2], P.A. Naik[2], B. Ramakrishna[1]

[1]Department of Physics, Indian Institute of Technology Hyderabad, Kandi, Sangareddy,502285, India
[2]Laser Plasma Division, Raja Ramanna Centre for Advanced Technology, Indore 452 013, India

The acceleration of high energy ion beams, (up to several tens of mega electron-volts per nucleon) following the interaction of ultra-short ($t < 1$ ps) and intense ($I\lambda^2 > 10^{18}$ W/cm^{-2}) laser pulses with solid targets, has been one of the most active areas of research in the last few years. Mechanisms leading to forward-accelerated, high quality ion beams, operating at currently accessible intensities in laser - matter interactions, are mainly associated with large electric fields set by the laser-accelerated electrons at the target interface. The emitted ion and, in particular, proton pulses contain large particle numbers (up to 10^{13}) with energies in excess of several MeV [1], have about ps pulse duration [2], and a and a source size of tens to hundreds of microns. In addition, conversion efficiencies (of laser energy to proton energy) up to 7 percent have been reported [3]. Recent experiments have reported deviation in the proton emission characteristics at the highest energy from the target normal direction. They assign that this non-target normal emission of protons at higher energies to a fast directed intra-pulse acceleration mechanism. In this paper, we report on the observation of wiggling in the accelerated proton beam as it traverses through the dense plasma sheath. There are very limited experimental details describing this behaviour of the charged particles. The information about the proton spectrum can give direct correlation on the information of the hot electron sheath evolving at ultra-fast timescale. Experiments on laser irradiated tiny water droplets, as used in [4-6] gave, for all the ions, perfect parabolic traces on a Thomson parabola ionspectrograph. This indicates that the geometry of the deflecting B and E fields of the spectrograph produces no artifacts on the ion trajectories. Further confirmation on this idea is obtained from the foil target experiments showing 5 degree deviation of the proton beam imprint recorded at high energies using complementary detector for ions i.e. radiochromic films (RCFs). This further confirms that the wiggling is mainly due to the fast changes in the accelerating sheath.

Now we discuss the possibility of controlling the pointing of accelerated ion beams using a technique by controlling the laser conditions. The wiggling in proton traces was studied in detail by varying the laser pulse duration, energy, and pre- pulse conditions, for Perspex, Mylar and CD2 target. Figure 1a shows the wiggled proton traces observed using our TPIS for plain poly methyl methacrylate (PMMA), Mylar (CHn), CD2 (deuterated polythelene) targets kept at the best focus. Figure 1b shows the same with pre-pulse added to the main laser pulse. When the target was at the best focus of the laser beam, one can see significant wiggling in the high energy proton spectrum recorded on the MCP and also very significantly for the heavier carbon ions (Fig. 1a). When the ASE pre-pulse was extended by changing the switch-out time of the pulse selector in the laser, the wiggling features in the spectral trace were considerably reduced, with no reduction in the maximum ion energy (Fig. 1b). The Mylar target showed significant wiggling for heavier ions like carbon but not for protons.

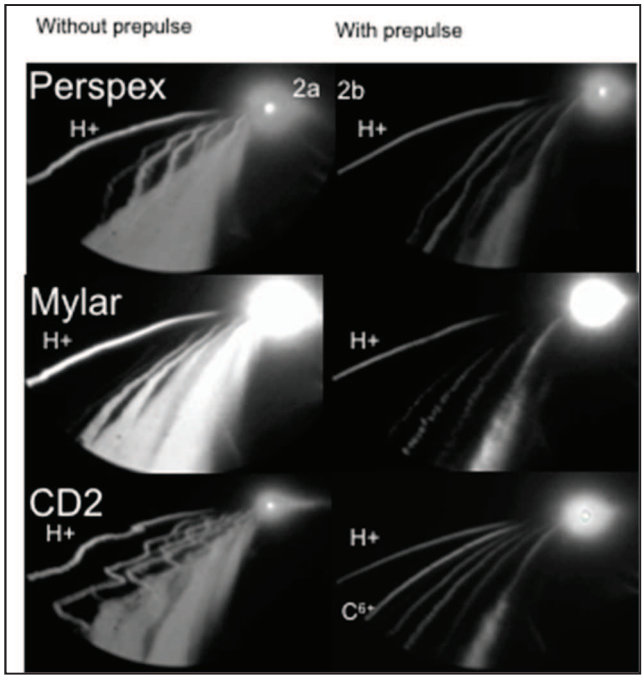

FIG. 1 : Proton beam traces from the Perspex (top), Mylar (center), CD2 (bottom) target front surface, showing the wiggling of the beam for the target kept at best focus, a) without pre-pulse (left), and b) with pre-pulse (right). A comparison of the wiggling of traces shows that with pre-pulse, there is a significant

Robinson et al. [7] proposed a scheme to obtain spectral control of the laser accelerated protons using two collinear intense laser pulses. The first pulse (pre-pulse), lower in intensity a factor of 10 than the second pulse, interacts with target to create a channel of hot electrons which creates an azimuthal magnetic field. The second laser pulse (the main pulse) creates the hot electrons which are guided through the channels already produced by the pre-pulse, thereby effectively decreasing the source instabilities in the proton beam. On similar lines, the wiggling of the traces in our case could be

attributed to the presence of multiple sources which create perturbation in the accelerating sheath (in absence of pre-pulse). The pre-pulse wipes out the source multiplicity occurring at ps time scales. Thus, one can control the ion source perturbation in laser plasma and mitigate the effects by varying the extent of the laser pulse. In other words, by using an extended pre-pulse, one can eliminate wiggling in the proton spectral trace. However, wiggling of the heavier ion beams in our experiment could not be controlled very effectively using this technique, due to their slow response to the sheath field.

In conclusion, we studied the ion emission from the front surface from solid targets interacting with TW class laser pulses. Our study indicates that proton emission from the target front surface is not uniform due to the perturbation in the source arising in intense laser plasma interaction. We have found maximum source perturbation in the proton source for plastic targets can be controlled by adding a proper pre-pulse to the main laser pulse. This study could be useful in understanding the ion acceleration and using these directed proton beams for fast ignition fusion so as to deposit maximum energy in the core to produce viable fusion energy.

References

[1] R. A. Snavely et al., Phys. Rev. Lett. 85, 2945 (2000).
[2] L. Romagnani et al., Phys. Rev. Lett. 95, 195001 (2005).
[3] J. Fuchs et al., Nat Phys 2, 48
[4] J. Schreiber, Phys. Plasmas 13, 033111 (2006);
[5] J. Schreiber, M. Kaluza, B. M. Hegelich Appl. Phys. B: Lasers Opt. 79, 1041 (2004).
[6] S. Ter Avetisyan et al., Phys. Lett. 82, 3354 (2003).
[7] A. P.L. Robinson, D. Neely, P. McKenna, and R. G. Evans. PPCF 49(4):373-384 (2007)

Nonmonotonic oxygen ion energy spectra observed in the interaction of high-intense femto-second laser pulses with CO_2 clusters

T. Pikuz [1,2], S. Bochkarev [3.4], A. Faenov [1,2], A. Brantov [3,4], V. Kovalev [3,4,5], I. Skobelev [2,6], S. Pikuz [2,6], R. Kodama[7], K.Popov [8], and V. Bychenkov [3,4]

[1]OTRI, Osaka University, Osaka, 565-0871, Japan, [2]JIHT, Moscow, 125412, Russia, [3]LPI RAS, Moscow, 119333, Russia, [4]CFAP VNIIA ROSATOM, Russia, [5]KIAM, RAS, 125047, Russia, [6]MEPhI, Moscow, 115409, Russia, [7]GSE and ILE, Osaka University, Osaka, 565-0871, Japan, [8]University of Ottawa, ON K1N 6N5, Canada

The gas cluster plasma offers great potential for various applications, including nuclear reactions, laser driven high-energy ions, sources of hot electrons and x-ray radiation. On the one hand cluster targets possess all practical advantages of gases (easy control, simple replacement, good replication, and so on) and on the other hand they make it possible to investigate all processes characteristic for high material density. Despite long-lasting efforts, a complete understanding of the interaction of short laser pulses with clusters is still far from clear.

For more than twenty years after the first observation, the formation of very pronounced peaks in the contour of the OVIII Ly_α emitted by CO_2 clusters irradiated by the 2ω Ti:Sa pulses with intensity about 10^{18} W/cm^2 remained uncharacterized. In contrary those spectral line shape feature was not presented in the case of heating clusters by laser pulses on the fundamental 1ω frequency (Fig. 1).

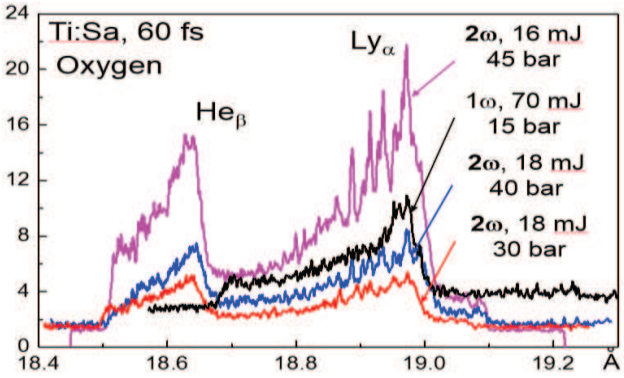

Figure 1. Plasma emission spectra in the spectral range of 18.5– 19.2 Å at different experimental conditions. The contour of the O VIII Ly_α has characteristic intensity modulations in the blue wing of line that are especially conspicuous when the clusters are heated the 2ω. Laser parameters: τ = 60 fs, $E_{1\omega}$ ~ 70 mJ, $E_{2\omega}$ ~ 20 mJ [1]

The key supposition that could explain nonmonotonic behavior of the O^{+8} energy spectra (2ω case) is ion acceleration to different energy from both radially expending a quasi-homogeneouse gas macroplasma of laser caustics and single clusters not fully destroyed by prepulse [2]. In our consideration the averaged energy spectrum of the light ion was found by the solution of the kinetic equation system for two-ion component plasma (the ion bulk with the average charge $\langle Z\rangle_1$=3 and atomic number $\langle A\rangle_1$ =16 and the high-Z impurity with $\langle Z\rangle_2$=8 and $\langle A\rangle_2$=16) and two-temperature electrons (T_{hot} ≈30 keV, T_{hot}/T_{cold} ≈ 90, n_{hot} ≈ 0.1n_{cold}) at quasineutrality approximation for adiabatic expansion of a hot macroscopic gas plasma [3]. The modeling of cluster expansion was done by electrostatic gridless spherical particle code (EGSPC) and by the full 3D relativistic PIC code Mandor which allow to reproduce spectral peaks corresponding to clusters with different size, density and density profiles smoothing due to prepulse effect. The well-pronounces energy peaks (width of ~ 100 keV) shifted to the cutoff energies 300 to 800 keV were obtained for cluster diameters 100,120 and 160 nm (Fig. 2). Corresponding hot electron temperatures are T_{hot} ≈ 140, 120

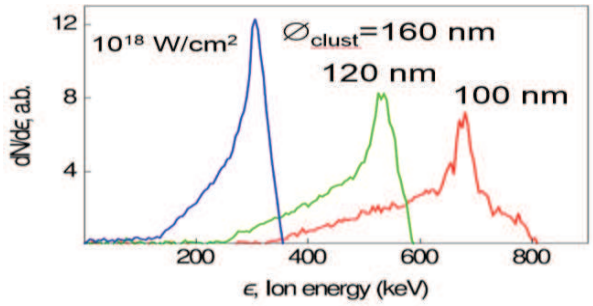

Figure 2. Spectra of impurity cluster ions obtained by 3D PIC simulations (laser: 2ω, 16 mJ, ~10^{18} W/cm^2) [2]

and 80keV. The characteristic peak energies are propor-tional to the T_{hot}. The electron distributions are two-temperature like with T_{cold} ≈ 10 to 30 keV. The smaller cluster size (steeper initial density profile), the high cutoff energy of the spectrum, and corresponding peak energy agree with the qualitative results of the electrostatic mod-eling.

Thus the applied theoretical approach shows that ob-served complicated profile of highly charged state of oxy-gen ions is defined by particles accelerated both from gas and clusters. Ions originating from clusters provide pro-nounced peaks in the spectra for 2ω high-contrast radia-tion. It cannot be excluded that strongly expanded but not entirely destroyed clusters from prepulse could also lead to a weak modulation in the profile of spectral line in the case of 1ω laser pulses.

References

[1] S. Dobosz et al. JTEP Letters, 68 (1998) 454
[2] S. Bochkarev et al. Scientific Reports, 8:9404 (2018)
[3] V.F. Kovalev te al. PRL, 90 (2003) 185004

Reaching an extreme regime of the light-matter interaction

C. Baumann[*1] *and A. Pukhov*[1]

[1]Institut für Theoretische Physik I, Heinrich-Heine-Universität Düsseldorf, 40225 Düsseldorf, Germany

A new generation of laser facilities is currently under construction around the globe, and the laser facilities aim at surpassing at least intensities of the order of 10^{23} Wcm^{-2} (see, for instance, the European project ELI [1]). Besides, there is the plan to build new accelerators providing electrons with energy above 100 GeV [2]. Consequently, the combination of both has the potential to explore a variety of novel regimes of the light-matter interaction. For example, it would be conceivable that electrons might experience electromagnetic fields in their current rest frame that are 1000 times stronger than the critical field of QED $E_{\mathrm{crit}} = 1.3 \times 10^{16}\ \mathrm{Vcm}^{-1}$). However, note that in order to make such an experiment indeed realizable, it is essential to reduce the field-electron interaction time to a minimum. The reason behind this is the ultra-fast time characterizing the radiation losses due to synchrotron radiation ($t_{\mathrm{rad}} \approx 200$ as, see [3]). The radiation losses reduce the electron energy and thus also the electromagnetic field that is seen by the electron in its current rest frame. Getting access to such a regime is therefore closely related to finding experimental configurations in which the interaction time is sufficiently shortened. After decades of assuming that this is experimentally not possible, first proposal have been presented just recently [3, 4, 5, 6]. The present contribution gives a brief overview on these attempts.

The characteristic radiation time is ultra-short ($t_{\mathrm{rad}} \approx 200$ as) in comparison with the duration of normal optical laser pulses ($\tau \sim 10$ fs). To get nonetheless access to the regime described above, it is necessary either to convert the optical laser radiation into shorter pulses or to use other sources of strong electromagnetic fields. The latter has been proposed by Yakimenko *et al*. [3] [see sketch in Fig. 1(a)]. The proposal is based on a future electron-electron collider with 125 GeV electron beams. The colliding beams are supposed to be tightly focused in the transverse direction (rms width $\sigma_\perp = 10$ nm) and to be extremely dense, resulting in a peak current of 1.7 MA. Such a charged beam generates an electromagnetic field that is as intense as a laser of the next generation. To ensure the ultra-short interaction time, the beams are also extremely compressed along the longitudinal direction (rms length $\sigma_\parallel = 10$ nm). Numerical simulations emphasize the feasibility of the proposal.

The conversion of an optical laser pulse into an ultra-intense attosecond pulse is discussed in [5] [see sketch in Fig. 1(b)]. It is shown that illuminating an over-dense plasma surface at oblique incidence with an intense optical laser pulse can efficiently trigger the generation of higher harmonics. In particular, it is found that the generated electromagnetic pulse has a duration of $\tau \approx 150$ as and an intensity of $I = 2.9 \times 10^{24}\ \ \mathrm{Wcm}^{-2}$. A probing ultra-relativistic electron beam could get access to the super strong-field regime which is again underlined by numerical simulations.

A third proposal can be found in [6] [see sketch in Fig. 1(c)]. Instead of converting the optical pulse into an attosecond pulse via high harmonics, the idea there is to use the shielding properties of the plasma itself. It is well known that the penetration depth in an over-dense plasma is restricted by the (relativistic) skin depth. As a result, the plasma is almost field-free since no external electromagnetic wave can propagate inside. This means that if the skin depth is short enough, a counter-propagating electron beam will experience the strong laser field almost instantaneously. Numerical simulations support the proposal.

In conclusion, an extreme and almost unexplored strong-field regime may become accessible in the future.

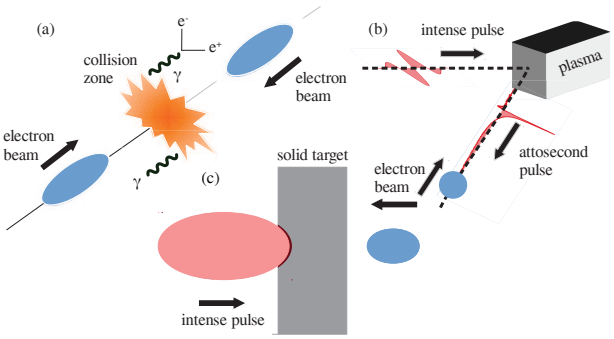

Figure 1: Sketches of the proposed experimental schemes. See [3, 5, 6] for more information.

References

[1] Extreme Light Infrastructure, https://www.eli-laser.eu/

[2] H. Baer *et al*., arXiv:1306.6352 (2013)

[3] V. Yakimenko *et al*., Phys. Rev. Lett. 122, 190404 (2019)

[4] T. G. Blackburn *et al*., New J. Phys. in press (2019), https://doi.org/10.1088/1367-2630/ab1e0d

[5] C. Baumann *et al*., arXiv:1811.03990 (2018)

[6] C. Baumann and A. Pukhov, "Laser-solid interaction and its potential for probing radiative corrections in strong-field QED", accepted for publication in Plasma Phys. Control. Fusion (2019)

* Christoph.Baumann@tp1.uni-duesseldorf.de

Stopping power measurement for 100 keV/u Fe ions in hydrogen plasma

R.O Gavrilin*, A.O. Khurchiev, D.S. Kolesnikov, S.A. Visotskiy, R.P. Kuibeda, P.A. Fedin, A.V. Bogdanov, V.A. Panyushkin A.V. Kantsyrev, I.V. Roudskoy, S.M. Savin, A.A. Golubev
NRC «Kurchatov Institute» - ITEP, Moscow, Russia

Introduction

Interaction of heavy ion beam with matter is important in a various area of knowledge. In the field of inertial confinement fusion the experimental investigation of ion beam stopping in ionized matter is important for verification and improving of existing theoretical models of ions stopping [1]. Also ionized gas targets is a candidate as ion beam stripper devices on FAIR [2]. This work will update of existing experimental data of ion beam stopping in hydrogen plasma for low energy (101 keV/u) of heavy ion beams. We present results obtained by two beam-times at ITEP in 2017 and 2018 years [3].

Plasma target

The plasma target (PT) was developed at ITEP. Plasma is generated by igniting of electrical discharge in two collinear quartz tubes filled with hydrogen gas. Such PT design provides to neutralize of ion beam focusing effect caused by the magnetic field of the discharge current. Capacitors bank is charged up to 2-5 kV and discharging by thyratron switch. Maximum discharge current is up to 3kA. The two coils are installed opposite are used for current symmetrization in collinear PT tubes.

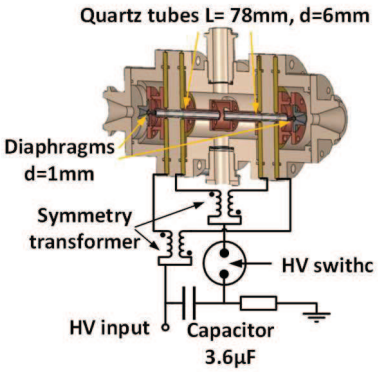

Figure 1: Principal scheme of plasma target.

The plasma parameters were measured with two-wavelength laser interferometry [4]. The maximal linear electron density was reached $(6.6\pm0.7)10^{17}$ cm^{-2}, maximum degree of ionization 0.35±0.01 was achieved.

Experimental setup

The Heavy Ion Prototype (HIPr-1) RFQ linac facility at ITEP provide of heavy ions acceleration with A/Z~60 and energy 101 keV/u. The MEVVA ion source is used at HIPr-1. The ion beam pulse with duration up to 450 μs consists of 27 MHz micro bunch structure. The beam pulse repetition rate is 0.25 Hz. Ion beam line includes three electro-magnetic quadrupole lenses and two diagnostic chambers. The Faraday cups (FC) were used for beam current measurement. The ion beam dynamic numerical simulation was performed for improves of beam transmission through the plasma target [5].

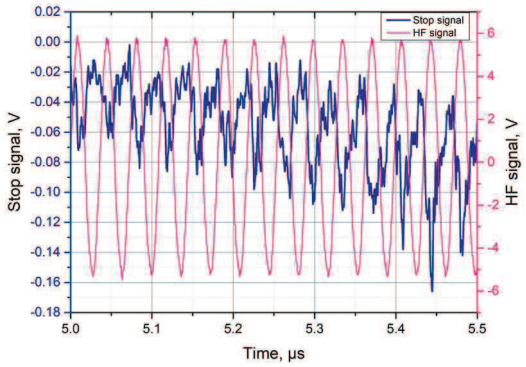

Figure 2: PMT signal of ion beam corresponding with frequency signal.

The scheme of experimental setup presented on fig.4. The Fe^{+2} ion beam with 5.6 MeV energy and origin current of 4 mA was used in experiments. Ion beam is passing through the diaphragms of differential vacuum system and plasma target. The transmitted beam current, measured by FC3 is in range of 10-30 uA depends of initial gas pressure in PT. The maximal hydrogen pressure in PT is limited with 4 torrs by pumping system efficiency and diaphragm D1-4 apertures. The time of flight method was used for energy loss measurement. The sapphire scintillator, FEU-87 photomultiplier (PMT) and DPO3054 oscilloscope were used for ion beam microbunch temporal structure measurement (fig.2). Time resolution of TOF system was 0.4 ns. In last beam time the PMT detector and all measurement equipment were additionally protect from electrical PT and RFQ noises. It provide of tenfold decrease of noise signal at PMT. The data acquisition system [6] provides remotely control experiment synchronization , data reading and saving. Shot to shot beam current fluctuation due to the instability of ion source curent was suppressed by averaging over a measurement series 40-60 shots.

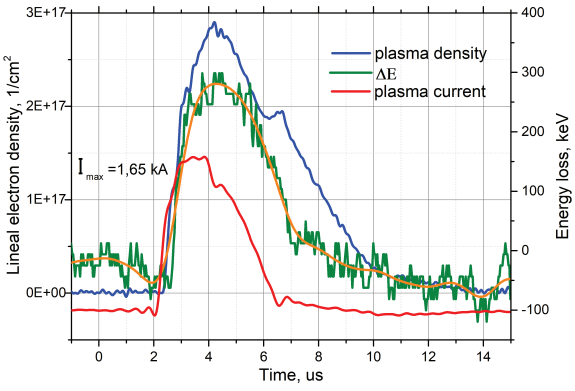

Figure 3: Measured ion beam energy losses in plasma orresponding with plasma density and discharge current

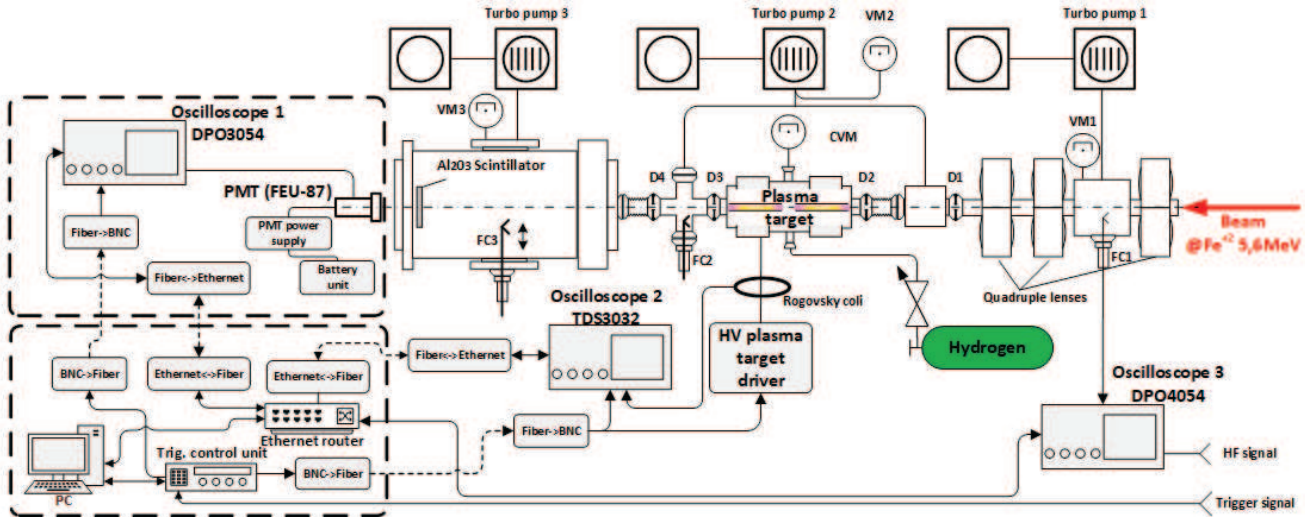

Figure 4: Principal scheme of experimental setup. FC-faraday cup. VM- vacuum meters device. D1-4 differential pumping system diaphragms, CVM –gas independent vacuum meter

Data analysis

The data processing includes Fourier analysis and filtering of PMT signals, determination of beam microstructure peak positions and finding the time delay of this peaks compare with the reference HF signal. Example of obtained energy losses curve (ΔE) presented on fig.3, decreasing of energy loss value to negative, after the end of discharge, may caused by gas flowing out from discharge tube.

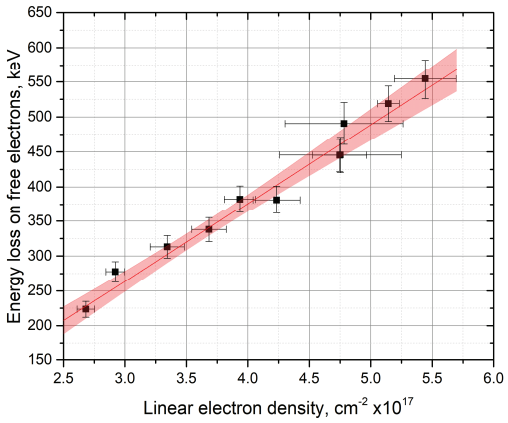

Figure 5: Ion beam energy loses caused by free electrons of plasma

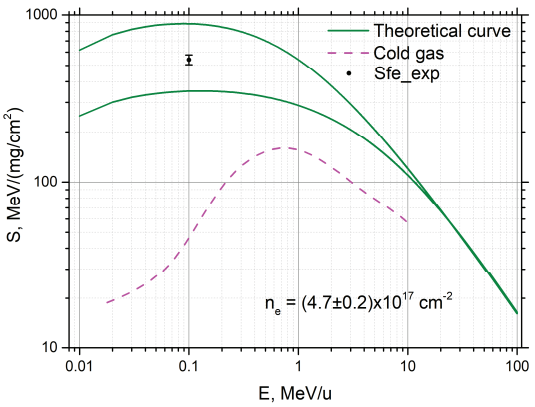

Figure 6. Comparison of experimental result for the hydro -gen plasma stopping power with theory calculations

The ion beam energy losses caused by free electrons of plasma are presented on the fig.5. The bound plasma electrons contribution to the ions energy loss value was subtracted using previously obtained plasma ionization degree [4]. The obtained average stopping power value of hydrogen plasma is S_{fe}= (546±45) MeV/(mg/cm^2). On figure 6 presented calculation of S_{fe} plasma stopping power by projectile ion energy. Curves on graph calculated for different effective ion charge, upper curve for Z_{eff}=8.6 given by theoretical estimation [7], lower for other estimation Z_{eff}=5.3 given by [8]. Charge state corresponding experimental result is Z_{eff}=7.

Beamtimes with other ion types and application of spectrometry plasma diagnostic methods is planned in near future.

References

[1] C. Deutsch, G. Maynard, M. Chabot et al., The Open Plasma Physics Journal 3, 88-115 , (2010)

[2] K.Cistakov et al. GSI Report 2016, p.22

[3] R.O. Gavrilin et al., GSI Report 2018-2, p.34

[4] A.O. Khurchiev, GSI Report 2019, in print.

[5] E Khabibullina et al. 26th RUPAC2018, Protvino, Russia doi:10.18429/JACoW-RUPAC2018-TUPSA61

[6] A. V. Kantsyrev, et al. Instruments and Experimental Techniques, 2010, Vol. 53, No. 5, pp. 663-674

[7] M.M.Basko, Stopping of fast ions in dense plasmas , Sov. J. Plasma Phys., 10 (6) (1984) 689-694

[8] Gus'kov S.Y. et al. Plasma Physics Reports. 2009. Т. 35. № 9. С. 709-718 DOI: 10.1134/S1063780X09090013

Supported by RFBR grand №18-02-00967

Ablation of plastics by intense pulsed ion beam and its shielding on energy deposition*

X. Yu[1], S. Zhang[1], S. Yan[2], G.E. Remnev[1], X. Le[1,#]
[1]Beihang University, Beijing, China; [2]Peking University, Beijing, China

Intense pulsed ion beam (IPIB), with ion energy of up to 1 MeV, beam current density of several hundred A/cm^2 and pulsed length of several hundred ns, can induce strong thermal shock in the surface region of target, leading to fast surface melting or even evaporation [1]. These effects can be used for surface treatment and material preparation with ablation plasma..

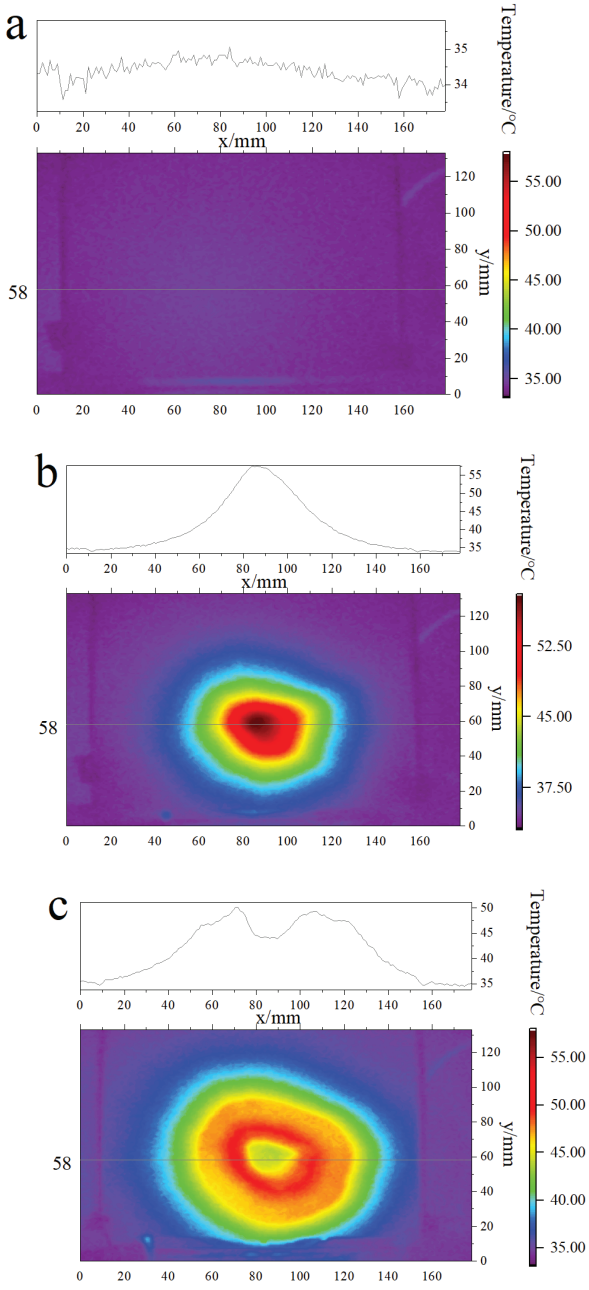

Figure 1: Target before irradiation (a), thermal prints of IPIB on 304 stainless steel (b) and PC (c).

When ablation is induced by IPIB irradiation, calorimetric diagnostics, such as calorimeters and infrared diagnostics may be attenuated. Especially by recent numerical research [2], ablation plasma may be formed during IPIB irradiation and thus the energy of the beam may be shielded by the ablation plasma. In this work, infrared imaging diagnostics [2] was carried out with 100 μm thick 304 stainless steel and 125 μm thick polycarbonate (PC) target to study the energy deposition of IPIB. The experiment was carried out on pulse ion beam accelerator BIPPAB-450. The pulse length of IPIB was 130 ns, cross-sectional energy density under 1 J/cm^2. Thermal prints by single pulse of IPIB irradiation was captured by a FLUKE Ti25 thermal camera within 0.1 s after pulse emission

The thermal prints on stainless steel generally exhibits quasi-Gaussian distribution. In the beam focus IPIB generates a temperature rise of 22 K, corresponding to an energy density of 0.91 J/cm^2. Under this energy density, no obvious surface ablation happens on the target surface [2]. However, on PC target, when the energy density exceeds 0.28 J/cm^2, according to energy density distribution on stainless steel target, with higher energy density comes lower energy deposition on the PC target. In the beam focus less than 0.15 J/cm^2 was deposited on the target. That means over 80 % of the beam energy cannot be deposited on the target.

The decrease of energy deposition on PC may be induced by the surface ablation due to its lower thermal conductivity and thermal evaporation temperature compared with metals and alloys. During IPIB irradiation, surface ablation plume can be generated on the target surface and a shielding layer can be formed by the ablation products and the energy of ions are largely dissipated in it. This phenomenon may also appear when irradiate metals under higher beam power density under which a dense ablation plume can be generated at the early stage of IPIB irradiation.

References

[1] G. E. Remnev, I. F. Isakov, M. S. Opekounov, et al. “High intensity pulsed ion beam sources and their industrial applications,” Surface & Coatings Technology, 1999, vol 114(2–3), pp. 206-212.

[2] X. Yu, J. Shen, M. Qu, et al. “Characterization and analysis of infrared imaging diagnostics for intense pulsed ion and electron beams,” Vacuum, 2015, vol 113, pp. 36-42.

* Work supported by China, NSFC contract No. 11875084.
#xyle@buaa.edu.cn

Research on Plasma Lens with Discharge Initiation by an Electron Beam

A. Drozdovsky[1], P.Sasorov[2], A.Bogdanov[1], S. Drozdovsky[1], R. Gavrilin[1], A.Kantsyrev[1], V. Panyushkin[1], I.Roudskoy[1], S.Savin[1], V.Yanenko[1]

[1]NRC «Kurchatov Institute» - Institute of theoretical and experimental physics, Moscow, Russia, [2]Keldysh Institute of Applied Mathematics, Moscow

The usual process of Z-pinch formation in the existent plasma lenses begins with a breakdown on the surface of the discharge tube [1, 2]. We study the discharge process when an injected electron beam creates a plasma channel after the application of high voltage pulse to the discharge tube. That causes the breakdown throughout the tube cross section.

The installation (fig. 1) consists of the electron gun with magnetic lenses, the experimental chamber with the scintillators located in it and the chamber of Z-pinch formation [3]. The amplitude of beam current is 100 A, the electrons energy is 250 kV and the duration of the beam at the peak is 60 ns.

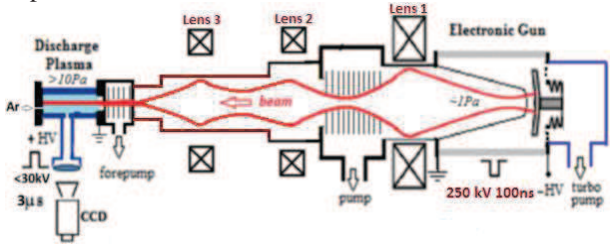

Figure 1: Installation for the research of plasma lens

Studies are expected to be performed in a wide range of pressures, from 0.1 to 10 mbar. The problem is that the pressure in the electron gun should not exceed 0.02 mbar. The easiest way to solve it consists in installation of the decouple mylar film. To prevent a significant increase of the beam phase volume, the film thickness should be about 1 μm. For studies in the field of low pressures, up to 0.5 mbar, it is possible to manage without the film due to the pressure gradient created by the used differential pumping system: packages of diaphragms are set near the crossover of electron beam. As a result, the ratio of pressure in the discharge tube and in the gun was reached up to 10.

Observations of the process of pinching of the 0.2 mbar argon plasma discharge in a quartz tube a length of 14 cm, an diameter of 4 cm were carried out by the recording CCD camera. The duration of the sinusoidal half-wave of the discharge was 3 μs. Beam parameters: inlet current ~ 10 A, beam diameter ~1.5 cm. Figure 2 shows the beam track luminosity before the breakdown.

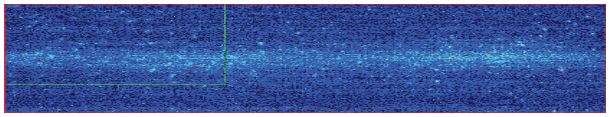

Figure 2: Luminosity of the beam track (frame duration – 200 ns)

Figure 3 shows the time scan of the discharge luminosity and corresponding waveforms at the supplied voltage 17 kV and the discharge current amplitude -120 kA. Figure 4 The results of observations in the initial discharge stage were compared with numerical simulations using the shows the same characteristics without the initiation beam.

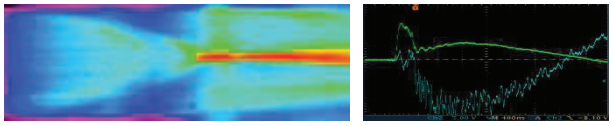

Figure 3: Plasma luminosity in 2 μs Current and voltage

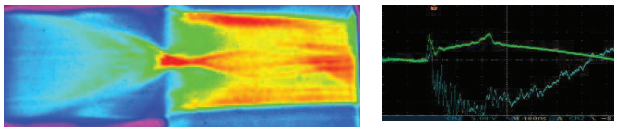

Figure 4: Plasma luminosity in 2 μs Current and voltage

MHD code NPINCH [4]. The experimental data were carried out with the application of the Abelian transform. Fig. 5 and 6 shows experimental and calculation results for radial distributions of the electron density of the discharge plasma at some moments after the beginning of the discharge.

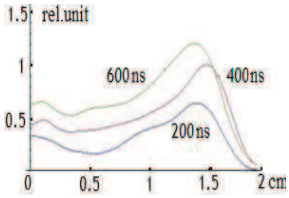

Figure 5: Experimental distribution of emitters

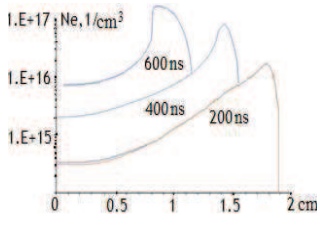

Figure 6: MHD - distribution electron density

MHD-calculations well describe the traditional z-pinch discharge. But this technique does not give qualitatively correct predictions in the case of a discharge with electron beam initiation. For the case of electron beam discharge initiation the plasma distribution is quite uniform during a large time interval. This distribution is more desirable for the purpose of creating a plasma lens with linear focusing forces.

References

[1] E.Boggasch, M.Dornik, D.H.H.Hoffmann, M.de Magistris, W.Laux, A.Tauschwitz, H.Wetzler, IEEE Trans.on Plasma Sci. 23, 388-392 (1995)

[2] J. van Tilborg et al, \Nonuniform discharge currents in active plasma lenses. Physical Review, Accelerators and Beams 20, 032803 (2017)

[3] A.A. Drozdovsky et al, Installation for Studying the Plasma of Z-Pinch Initiated by an Electron Beam. Physics of Particles and Nuclei Letters, 2016, Vol. 13, No. 7.

[4] N.A. Bobrova, S.V.Bulanova, T.L.Razinkova, P.V. Sasorov, Dynamics of a Pinch Discharge in Capillarics Plasma Physics Reports, 1996, vol. 22

* Work supported by the Russian Foundation for Basic Research (grant 18-02-01187/18)

Particle-in-cell simulation of propagation of intense proton beams in gas plasmas: role of hydrodynamic instabilities

B. Chen[1], D. Wu[2,1,*], J. Ren[1], D. Hoffmann[1], W. Liu[1], S. Xu[1], X. Wang[1], Z. Xu[1], X. Ren[1],

R. Cheng[3], X. Zhou[3], Y. Lei[3], X. Qi[3], G. Xiao[3], Z. Hu[4], F. Gao[4], Y. Wang[4], and Y. Zhao[1,#]

[1]School of Science, Xi'an Jiaotong University, Xi'an 710049, China

[2]State Key Laboratory of High Field Laser Physics, Shanghai Institute of Optics and Fine Mechanics, Chinese Academy of Sciences, Shanghai 201800, China

[3]Institute of Modern Physics, Chinese Academy of Sciences, Lanzhou 730000, China

[4]School of Physics and Optoelectronic Technology, Dalian University of Technology, Dalian 116024, China

The transport of particles in matter and their interaction are among the most significant research interests in physics, due to their wide applications to many fields such as high energy density physics, accelerator physics, and inertial confinement fusion (ICF). One of the key factors affecting the particle transport in matter is beam-plasma instabilities, which are of great varieties and significantly influence the distribution, movement and interaction of particles. They certainly should be controlled when it comes to fast ignition and plasma wakefield acceleration. To effectively uncover the complicated beam-plasma instabilities, one needs to take into account both collective electromagnetic effects and close interactions among electron-electron, electron-ion and ion-ion. Therefore, among all the possible solutions, PIC simulation is a promising candidate.

In this work, the transport of proton beams through hydrogen plasmas with density of 10^{22} m^{-3} is simulated (see Fig.1) with a 2D PIC code. The formation and development of sausage instability and kink instability during the interaction are studied. The simulation reveals that density of proton beams increases due to the focusing effect. The focusing positions are fixed, which can be explained by sausage instability. When the beam density increases, proton beams are bended by the kink instability due to the different magnetic pressures on the two sides of the beam. By adjusting the injection velocity, using heavier ion beams and applying appropriate primary magnetic field, the kink instability can certainly be suppressed. Our finding may have important applications in proton fast ignition, ICF, high energy density physics, and accelerator physics.

* E-mail: wudong@siom.ac.cn
# E-mail: zhaoyongtao@xjtu.edu.cn

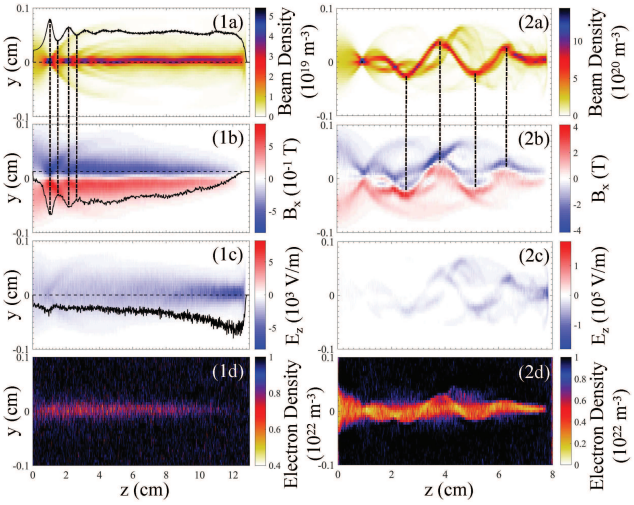

Figure 1: The transport of proton beams in plasmas. By row, (a)-(d) correspond to proton beam density, magnetic field, electric field and background electron density. Column (1) and (2) correspond to proton beams with densities of 10^{19} and 10^{20} m^{-3} and injection energies of 200 and 400 keV. Pictures of column (1) and (2) are token at 20.7 and 9 ns respectively. The black curves in (1a), (1b) and (1c) represent the relative intensity along

References

[1] Y. Zhao, R. Cheng, Y. Wang, *et al.*, High Power Laser Science and Engineering 2 (2014).
[2] D. Wu, X. T. He, W. Yu, et al., High Power Laser Science and Engineering 6 (2018).
[3] D. Wu, X. T. He, W. Yu, and S. Fritzsche, Physical Review E 95 (2017).

Time-dependent simulation of the energy loss experiment for alpha particles moving in discharged H-plasmas*

Y.N. Zhang[1,2], B. He[2#], C.S. Liu[2], and Y.T. Zhao[1]

[1] Xi'an Jiaotong University, China; [2]Beijing Institue of Applied Physics and Computational Mathematics, China

The energy loss ΔE of ions moving in discharged H plasmas has been measured for more than 20 years [1-3]. The first relevant experiment [1] confirmed the theoretical stopping power predictions close to the expected maximum in fully ionized plasmas, which is much higher than that in neutral gas. Later similar results were found by Golubev *et al.* [2] with 3 MeV protons as the projectile. In recent years a series of such experiments were made in the Institute of Modern Physics in China [3] with the projectile energy E_p equal to 100keV/u. Especially ΔE evolution for alpha particles in partially ionized H plasmas were measured, which could not be described by Bethe equation in atomic units

$$-\frac{\mathrm{d}E}{\mathrm{d}x}=\frac{4\pi Z_{eff}^{2}}{v_p^{2}}\left\{n_{be}Log\frac{2V_p^{2}}{I}+n_{fe}Log\frac{2V_p^{2}}{\omega_p}\right\}.$$

Here Z_{eff}, v_p, n_{be}, n_{bf}, I and ω_p are the projectile effective charge, velocity, bound and free electron density, mean ionization energy of H, and the plasma frequency, respectively. How to explain the experiment is the aim of the present work. In order to do this time-dependent simulations with the rate equations of the projectile charge states have been made and the above equation is also revised since v_p (=2) is not much higher than Bohr velocity. Some details of our simulation are listed in the following.

First the fraction evolution for the possible states of the projectiles in the plasmas including He^{2+}, $He^{+}(1s)$, $He^{+}(2l)$, $He^{+}(2l)$, $He(1s^2)$ and He(1s2l), are obtained according to the time-dependent rate equations of the states [4]. In the simulation the main processes which have strong influences on the projectile states are considered, which include charge transfer, ionization and excitation by electron, proton and H(1s), spontaneous radiation, impact de-excitation, recombination, etc. Besides this all the relevant cross sections and transition rates are obtained by non-perturbative methods and FAC code. The data for n_{be} and n_{bf} evolution are determined by initial energy loss at gas and Ref. [5].

Next the respective stopping powers due to He^{2+}, He^{+}, and $He(1s^2)$ in H gas are found by classical trajectory Monte Carlo [6] with total stopping power and the fraction of the projectile states in good agreement with the recommended [7] and experimental data [8], respectively. The corresponding stopping powers in electron plasmas are obtained with the influence of bound electrons included. Based on these the evolution for ΔE is found, which agree well with the experiment and better than those by the assumption of steady state approximation for the projectile, which is shown in Fig.1. The fractions for He^{+} and He^{2+} charge states are found slowly increase and decrease with time as ΔE rises up gradually when the projectile moves in the plasmas. Electron capture, Ionization and spontaneous radiation are found the most important processes which affect the projectile charge state. All the recombination processes are very weak in this case.

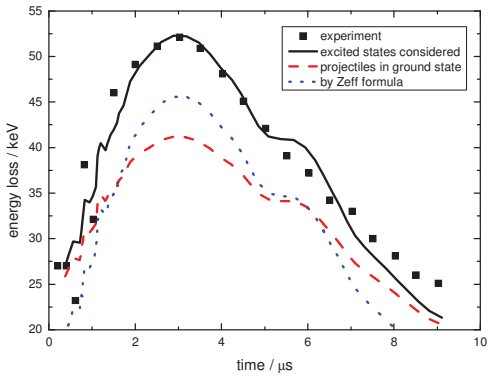

Figure 1: Experimental data (full squares), our simulation results with all the states (solid line) and only ground states included (dash line), and the result from Bethe equation (dots).

References

[1] J. Jacoby et al., Phys. Rev. Lett. 74 (1995) 1550.
[2] A. Golubev et al., Phys. Rev. E 57 (1998) 3363.
[3] R. Cheng et al. Laser & Particle Beams.36 (2018) 247
[4] T. Peter and J. Meyer-ter-Vehn 1998 Phys. Rev. A 43 (1991) 2015
[5] A.P. Kuznetsov et.al., Plasma Phys. Rep. 39 (2013) 248
[6] R.E. Olson and A. Salop, Phys. Rev. A 16, (1977) 531
[7] J.F. Ziegler 1977 Helium Stopping powers and Ranges in All Elemental Matter
[8] S.K. Allison, Rev. Mod. Phys. 30 (1958)1137

*Work supported by National Key R & D Program of China under Grant Nos. 2017YFA0402300 and 2017YFA0403200
#hebin-rc@163.com

Simulations of Beam-Plasma Interactions in Plasma-Based Particle Accelerators*

Kookjin Moon and Moses Chung †
Ulsan National Institute of Science and Technology (UNIST), Ulsan 44919, Korea

Introduction

Ideas of plasma-based particle accelerators have been developed for decades with the promise of ultrahigh acceleration capability which is orders of magnitude higher than those of any conventional accelerators. Despite the great merit of this technology, many challenges have delayed its successful realization in the level of practical use. They are not only technical issues that arise in the laboratory, but also theoretically inherent challenges. The well-known issues are extreme spatio-temporal alignment requirement, transverse phase space matching, inherent substantial energy spread, beam-plasma instabilities, and limited amount of energy delivered from the driver beam to the witness beam (for the case of the beam-driven plasma wakefield, BD-PWFA). In this paper, we introduce two topics of BD-PWFA which are relevant to above issues using FBPIC code [1].

Self-modulation instability

The greater the energy of the driver beam, the greater the expected energy gain of the witness beam. High energy proton beams from hundreds of GeV to tens of TeV are already available at CERN, but its bunch length is too long for the optimum condition of the BD-PWFA. Therefore, the self-modulation instability (SMI), which occurs when the driver beam length is much longer than the plasma wavelength ($\lambda_p \ll L_b$), has been intensively studied to harness the beams ($\sim$10 cm) from the Super Proton Synchrotron (SPS) of CERN after the first theoretical modeling work was published [2].

Trojan Horse injection scenario

The Trojan Horse (TH) injection method uses a laser pulse with a small normalized vector potential ($a_0 \ll 1$) to ionize the residual gas inside the accelerating region of the plasma wakefield induced by a dense ($n_0 \ll n_b$) driver beam [3]. This TH injection method makes it possible to separate the physics of the driver and witness beams. For the parameters of interest, the TH injection could deliver the accelerating fields around the wave-breaking limit $E_0\ [\mathrm{V/cm}] \propto \sqrt{n_0\ [\mathrm{cm}^{-3}]}$, and the witness beams with tens of nm transverse emittances and a few kA of peak currents.

* Work supported by the National Research Foundation of Korea (NRF) Grant (No. NRF-2016R1A5A1013277).
† mchung@unist.ac.kr

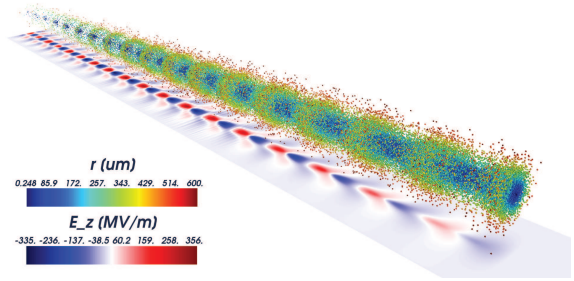

Figure 1: Simulation of the self-modulation instability. A long half-cut Gaussian proton beam is modulated by the self-induced plasma wakefields. The physical parameters of SPS proton beam are used except the reduced total charge and length.

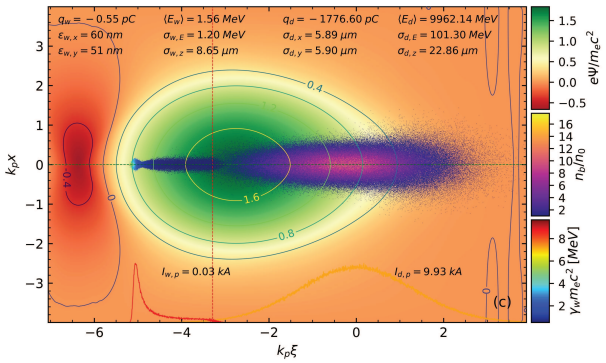

Figure 2: Simulation of the Trojan Horse injection. A driving electron beam induces accelerating and focusing wakefield region. A laser pulse ionizes residual Helium gas inside the ion cavity (or wake potential). The released electrons are trapped and accelerated in the wake potential.

References

[1] R. Lehe, M. Kirchen, I.A. Andriyash, B.B. Godfrey, and J.-L. Vay, Comput. Phys. Comm. 203, 66-82 (2016).

[2] N. Kumar, A. Pukhov, and K. Lotov, Phys. Rev. Lett. 104, 255003 (2010).

[3] B. Hidding, G. Pretzler, J. B. Rosenzweig, T. Konigstein, D. Schiller, and D. L. Bruhwiler, Phys. Rev. Lett. 108, 035001 (2012).

Photon Energy Inducing Different Absorption Channels in Gold

P. D. Ndione[1], *S. T. Weber*[1], *D. O. Gericke*[2], *and B. Rethfeld*[1]

[1]Fachbereich Physik und Landesforschungszentrum OPTIMAS, Technische Universität Kaiserslautern, Germany;
[2]Centre for Fusion, Space and Astrophysics, Department of Physics, University of Warwick, UK

Short laser pulses are able to drive materials out of thermodynamic equilibrium. Then, electronic scattering, as well as electron-phonon scattering, contribute to establishing a new equilibrium. Boltzmann collisions integrals have successfully been applied to obtain the electrons and phonons distributions. However, for many experiments, the optical properties are probed in the optical limit, meaning that the photons are assumed to transfer no momentum. In such a limit, the knowledge of the full electrons' distribution is not necessary anymore. Hence, the band occupation numbers are the only important quantities that determine the transient change of the optical properties during the excitation and relaxation process of the electrons.

In this report, we investigate the time evolution of the conduction band density in gold excited with a short light pulse. For optical photons, we only consider two active bands: the $5d$ valence band and the $6sp$ conduction band. The model assumes that shortly after excitation, both bands will establish a joint electronic temperature due to fast energy exchange between the bands. However, since particles exchange require much longer times, the chemical potential of the involved bands and their occupation numbers will stay much longer in nonequilibrium. We trace carrier balance as well as the electrons and phonons energy using a set of rate equations [1]

$$\frac{dn_{sp}}{dt} = \frac{\alpha_{\text{inter}}}{\hbar\omega_L} I_L - \frac{1}{\tau_{\text{relax}}} \left[n_{sp} - n_{sp}^{eq}(T_e) \right] , \tag{1a}$$

$$C_e \frac{dT_e}{dt} = \left[\alpha_{\text{intra}} + \alpha_{\text{inter}} \right] I_L - g_{ei}(T_e) \left[T_e - T_i \right] , \tag{1b}$$

$$C_i \frac{dT_i}{dt} = g_{ei}(T_e) \left[T_e - T_i \right] . \tag{1c}$$

Here, Eq. (1a) traces the time evolution of the density in the sp-band. The first term corresponds to the increase of the sp-density due to direct excitation of d-band electrons into the conduction band by the laser. The interband absorption coefficient α_{inter} is obtained by counting the number of accessible states at a given photon energy as described in Ref. [1]. The absorbed energy via interband process $\alpha_{\text{inter}} I_L$ and the energy of one photon $\hbar\omega_L$ determine the number of absorbed photons. In addition, we use the relaxation time approximation to describe the transfer of electrons from the d-band into the sp-band or vice versa, until an equilibrium density $n_{sp}^{eq}(T_e)$ is reached within a time τ_{relax}. The equilibrium density is determined by the electrons temperature and is obtained via, $n_{sp}^{eq}(T_e) = \int dE\, D_{sp}(E) f(E,t)$. The energy equations (1b) and (1c) describe the time evolution of the electrons and phonons temperature. We solve the rate equations (1) for gold. As input parameter, a relaxation time of 600 fs is used, a value consistent with some experiments previously observed in gold [2]. Fig. 1 illustrates the transient change of the sp-density in gold excited with a 45-fs FWHM Gaussian pulse. Two different photon energies are used. To allow direct comparison, all cases have the same absorbed energy of about 0.53 MJ/kg. For a photon energy of $\hbar\omega_L = 3.1$ eV, the sp-density exhibits an initial fast increase due to excitation of d-electrons into the conduction band. Small photon energies induce a large number of absorbed photons. The sp-band is therefore overpopulated and needs to relax towards an equilibrium density.

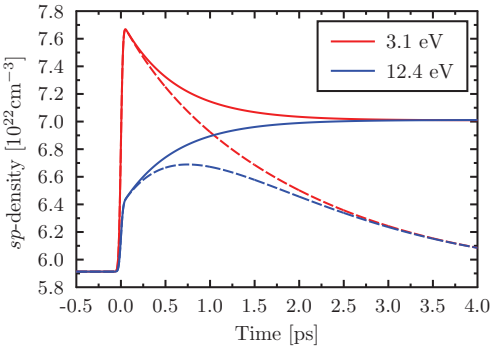

Figure 1: Time-dependent sp-density in gold calculated with Eqs. (1) for an absorbed energy of 0.53 MJ/kg. Solid lines consider only the electron system whereas dashed lines include coupling to the phonons.

For high energy optical photons (12.4 eV), the sp-density also fastly increases during the laser excitation, but we also observed a slow secondary increase at the end of the pulse due to high energy input per photon. Secondary electrons are generated by impact ionization. If now the electrons couple to the lattice (dashed lines), one observes a further decrease of the sp-equilibrium density in case of low photon energies, whereas for high energy optical photons, the secondary increase is completely reversed due to decrease of the electrons temperature.

Our model for the band occupation numbers shows therefore that depending on the photon energy of the driving laser, different absorption channels as well as additional time scales of the electrons dynamics are observed.

References

[1] P. D. Ndione, S. T. Weber, B. Rethfeld and D. O. Gericke, *CPP*, DOI:10.1002/ctpp.201800186 (2019).

[2] C. -K. Sun et *al.*, *PRB*, **48**, 12365(R) (1993).

Mode-Resolved Electron-Phonon Coupling in Aluminium at Elevated Temperatures

T. Held[1], *S. T. Weber*[1], *J. Vorberger*[2], *and B. Rethfeld*[1]

[1]Fachbereich Physik und Landesforschungszentrum OPTIMAS, Technische Universität Kaiserslautern, Germany;
[2]Institut für Strahlenphysik, Helmholtz-Zentrum Dresden-Rossendorf e.V., 01328 Dresden, Germany

In the case of a solid being irradiated by a short-pulsed visible light laser, the energy is almost entirely absorbed by the electrons while the lattice remains cold. The resulting energy flow between electrons and phonons is commonly described by the electron-phonon coupling parameter G_{ep}.

Different methods are available to calculate the coupling parameter. One solution is provided by Boltzmann collision integrals with an analytic plane wave matrix element [1]

$$|M_{ep}(q)|^2 = \frac{e^2}{2\epsilon_0 \Omega} \frac{E_q}{q^2 + \kappa^2} \quad , \tag{1}$$

which can only describe the coupling to the longitudinal phonon mode, assumed to carry the largest contribution.

E_q is the phonon energy, q is the phonon wave vector, κ is the screening and Ω is the volume of the unit cell.

Another method is calculating the coupling through the material-specific Eliashberg function, obtained via density functional theory (DFT). It includes all phonon modes but involves a low temperature approximation,

$$\alpha^2F(E, E_1, \omega) = \frac{D(E)D(E_1)}{D^2(E_F)} \alpha^2F(E_F, E_F, \omega)\,, \tag{2}$$

where $D(E)$ denotes the electronic density of states.

Recent DFT results [2] suggested that a phonon mode-resolved model is necessary to fully capture the process.

In this report we investigate the differences between both descriptions. We obtain the coupling parameters

$$G_{ep} = \frac{1}{T_p - T_e} \frac{du_e}{dt} = \frac{1}{T_p - T_e} \int dE \frac{df}{dt} D(E) E\,, \tag{3}$$

by integrating the respective collision integrals.

The calculations [3] were done for Aluminium, assuming a Free Electron Gas density of states, Debye dispersion for the phonons and the respective thermal distribution for each system. The total coupling with the Eliashberg approach is significantly higher than Boltzmann coupling, which can be attributed to the inclusion of all phonon modes, as the longitudinal coupling compares well to the analytic description.

We also see a difference in temperature dependence. For both descriptions the coupling steeply increases at low temperatures with a diminishing slope. But while the Boltzmann coupling adopts a linear increase for upwards of 5000 K, the Eliashberg coupling parameter reaches a maximum at 7500 K and then slowly decreases.

We assume that this difference in behavior is caused by missing temperature dependence in the Eliashberg description. Most collisions happen at the chemical potential, which for low temperatures lies at the Fermi edge. This justifies the initial approximation Eq. (2). For higher temperatures however, the chemical potential is shifted with regards to the Fermi energy, so the approximation may no longer hold. Additionally the electron screening influences the scattering probability and depends on the electron distribution and thus the temperature.

Modifications are done to the Eliashberg function, approximating it around the chemical potential and including an additional term to account for the screening change, incorporating similar dependence as the analytic expression,

$$\alpha^2F(E, E_1, \omega) = \frac{\kappa^2(0)}{\kappa^2(T)} \frac{D(E)D(E_1)}{D^2(\mu)} \alpha^2F(E_F, E_F, \omega)\,. \tag{4}$$

The resulting coupling parameters are shown in Fig. 1, and we see good agreement in the qualitative behavior and overall good agreement for the longitudinal mode.

In summary, we see that the contributions from the transversal modes are not negligible and we find good agreement for the description of the energy transfer to the longitudinal mode, provided one compensates the missing temperature dependence of the Eliashberg description.

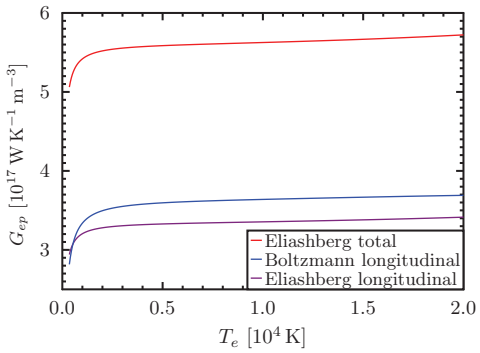

Figure 1: Electron-phonon coupling parameters for Aluminium. They are calculated using the matrix element Eq. (1) (blue), the total Eliashberg function (red) and the partial longitudinal Eliashberg function (purple). Both Eliashberg curves use approximation Eq. (4) instead of Eq. (2)

References

[1] G. Czycholl, Theoretische Festkörperphysik (2008)

[2] L. Waldecker and R. Bertoni and R. Ernstorfer and J. Vorberger, *PRX*, **6(2)**, 021003 (2016)

[3] T. Held, Bachelor Thesis, TU Kaiserslautern (2018)

Energy relaxation and electron phonon coupling in laser heated solids

J. Vorberger[1] *and T.A. Butcher*[1]
[1]Helmholtz-Zentrum Dresden-Rossendorf e.V., Dresden, Germany

A laser interacting with matter will leave the electrons in the target in an energetically enhanced state compared to the ions. A shock wave entering a system will heat the ions but leave the electrons in their ground state as before the shock wave. In any case, a non-equilibrium state is formed that will lead to a relaxation process towards a new thermodynamic equilibrium state. This relaxation is a multi stage process usually starting with the formation of an equilibrium electron distribution due to fast electron-electron collisions. Afterwards, the relaxation of the ionization state and the equilibration in between species take place along with the establishment of ion equilibrium momentum distributions.

Here, we focus on the special situation in which the conduction electrons in a metal have already established a high temperature in the electron volt range due to past optical laser irradiation and are significantly hotter than the lattice which, at the beginning of the modelling, is still at room temperature. Such a situation might be described using a two-temperature model (or by extension a multi-temperature model with different temperatures for different phonon modes). The energy transfer can be calculated by considering a set of Boltzmann equations for the electrons and different phonon modes. Important input quantities are the electronic density of states (DOS) $g(\varepsilon)$ and the occupation numbers of the electronic states $f(\varepsilon)$ in order to determine what the electronic states around the Fermi edge ε_F actually contribute to the energy transfer. The phonon states receiving the energy are determined by the phonon DOS and the electron-phonon coupling as incorporated in the Eliashberg function $\alpha^2F(\omega)$. The actual occupation of each phonon mode is given by the Bose distribution $n_B^p(\omega, T_p)$ [1, 2]

$$Z_{ep}(T_e, T_l, t) = \frac{2\pi N_c}{g(\varepsilon_F)} \int_{-\infty}^{\infty} d\varepsilon \, g^2(\varepsilon) \frac{\partial f_e(\varepsilon, T_e)}{\partial \varepsilon}$$

$$\times \int_0^{\infty} d\omega (\hbar\omega)^2 \alpha^2 F(\omega, T_e, T_l, t) \left[n_B^e(\omega, T_e) - n_B^p(\omega, T_p) \right].$$

The input quantities can be computed using density functional theory and the linear response formalism so that the lattice symmetries, ion-ion, electron-ion, and electron-electron correlations in a metal can be taken into account [3]. The electron-phonon coupling factor is then obtained from the energy transfer rate by dividing it by the temperature difference $G_{ep} = Z_{ep}/(T_e - T_p)$.

In Fig. 1, we show data for the electron-phonon coupling in copper with a fcc lattice structure. For these calculations, a stable lattice and DOS as at room temperature was assumed for all electron temperatures. The low temperature value of the electron-phonon coupling is in agreement with values given in Refs. [5, 6]. The values reported by Lin [4] are based on calculations by Savrasov et al. [7]. For higher electron temperatures, the obtained values are not in agreement with experimental results by Cho *et al.* and by Brown *et al.* [8, 9].

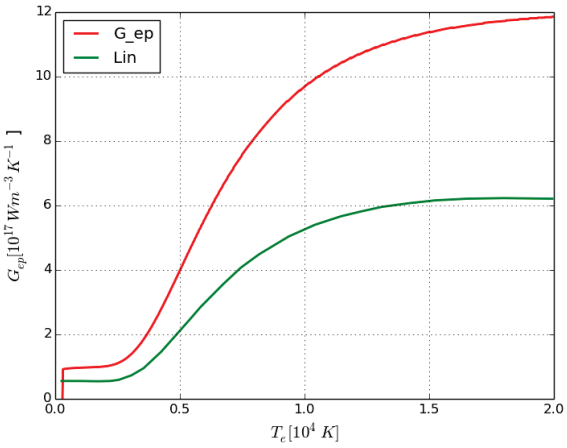

Figure 1: Electron-phonon coupling factor in fcc copper as a function of the electron temperature. The result of Lin *et al.* is taken vom Ref. [4].

Possible improvements in the theoretical description are the use of electronic DOS for the appropriate electron and ion temperatures as well as of temperature dependent electron-phonon coupling matrix elements.

References

[1] P. B. Allen, Phys. Rev. Lett. **59**, 1460 (1987).

[2] L. Waldecker, R. Betoni, R. Ernstorfer, J. Vorberger, Phys. Rev. X **6**, 021003 (2016).

[3] X. Gonze et al., Comput. Phys. Commun. **180**, 2582 (2009).

[4] Z. Lin, L.V. Zhigilei, Vittorio Celli, Phys. Rev. B **77**, 075113 (2008).

[5] H. E. Elsayed-Ali, T. B. Norris, M. A. Pessot, and G. A. Mourou, Phys. Rev. Lett. **58**, 1212 (1987).

[6] J.Hohlfeld, S.-S.Wellershoff, J.Güdde, U.Conrad, V.Jähnke, E.Matthias, J. Chem. Phys. **251**, 237 (2000).

[7] S.Y. Savrasov, D.Y. Savrasov, Phys. Rev. B **54**, 16487 (1996).

[8] B.I. Cho, T. Ogitsu, K. Engelhorn, A.A. Correa, Y. Ping, J.W. Lee, L.J. Bae, D. Prendergast, R.W. Falcone, P.A. Heimann, Scientific Rep. **6**, 18843 (2016).

[9] A.M. Brown, R. Sundararaman, P. Narang, W.A. Goddard III, H.A. Atwater, Phys. Rev. B **94**, 075120 (2016)

4 Particle-, Radiation- and Plasma Sources

Laser Driven Protons with Gamma Ray Flash*

D.F. Gordon[1], K. Spohr[2], D. Stutman[2], T. Grismayer[3], M. Vranic[3], A. Davidson[1], and T. A. Mehlhorn[1]
[1]Naval Research Laboratory, Washington, DC, USA; [2]Extreme Light Infrastructure Nuclear Physics, Bucharest-Magurele, Romania; [3]Instituto Superior Tecnico, Lisbon, Portugal

Pulsed lasers attain peak powers as high as 10 petawatts [1]. Strong focusing of such pulses enables experiments in the radiation dominated regime, the onset of which is expected to occur at about 10^{23} W/cm^2. If the target is a thin solid density slab, radiation pressure acceleration (RPA) of the ions is expected to be accompanied by a powerful burst of gamma rays due to nonlinear Compton scattering. The conversion efficiency of laser to gamma ray energy is computed to be as high as tens of percent [2].

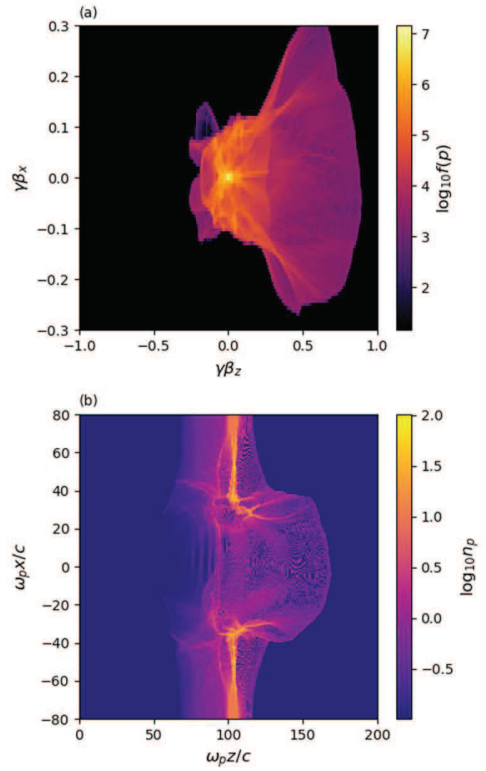

Figure 1. Momentum distribution (a) and spatial distribution (b) of protons after a few tens of femtoseconds of interaction.

Simulations of such an interaction have to be carried out using an extension of the particle-in-cell (PIC) method which uses nonlinear quantum electrodynamics (QED) cross sections to track the creation and subsequent interactions of high energy photons and electron-positron pairs. Currently there are a few such QED-PIC codes, including EPOCH [3] and OSIRIS [4]. Sample results from OSIRIS are shown in Figures 1 and 2 for peak laser intensity 10^{23} W/cm^2, pulse duration 25 fs and laser energy 300 J. The target is a 1 micron slab of solid density hydrogen, with a several micron long pre-plasma. This example case was carried out in 2D slab geometry, but 3D simulations are possible using large scale high performance computing systems.

The proton distribution in momentum space is shown in Fig. 1(a), while the distribution in real space is in Fig. 1(b). The laser pulse propagates in the positive z-direction. The fastest protons approach the threshold for relativistic motion, $\gamma\beta$=1, where γ is the relativistic Lorentz factor and β = v/c. The real space image illustrates the RPA-like deformation of the target. Fig. 2 shows the distribution of gamma ray momentum in terms of wavenumbers referenced to the reduced Compton wavelength, λ_c. The gamma ray spectrum can extend to GeV scale.

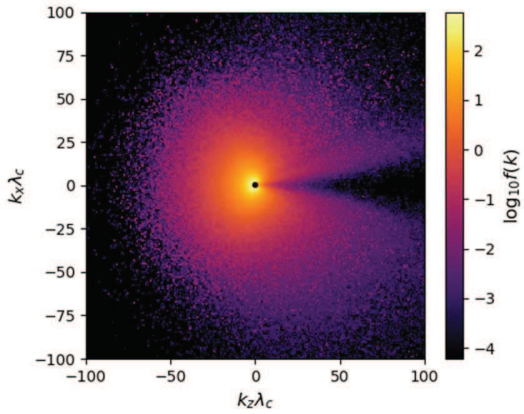

Figure 2. Momentum (wavenumber) distribution of the gamma rays.

In conclusion, ten petawatt scale lasers will enable the exploration of fundamentally new regimes of laser-plasma interactions where QED effects cannot be neglected. Moreover, the QED effects themselves are in an under-explored, highly nonlinear regime. One outcome predicted by QED-PIC simulations is the simultaneous generation of bright gamma rays and energetic protons.

References

[1] https://www.eli-np.ro/documents/press_releases/Comunicat_Presa_Eng_10PW.pdf
[2] K.V. Lezhnin et al., Phys. Plasmas **25**, 123105 (2018)
[3] C.P. Ridgers et al., Phys. Rev. Lett. 108, 165006 (2012)
[4] T. Grismayer et al., Phys. Plasmas **23**, 056706 (2016)

* Work supported by US DOE Office of Science under Interagency Agreement 89243018SSC000006

Recent progress on proton acceleration with PHELIX

J. Hornung[1,2,3], V. Bagnoud[1,2], C. Brabetz[2], U. Eisenbarth[2], M. Guenther[1], J. B. Ohland[4], V. A. Schanz[4], M. Shi[1], M. Zepf[1,3,5], B. Zielbauer[2], Y. Zobus[4]

[1]HI-Jena, Jena, Germany; [2]GSI, Darmstadt, Germany; [3]Friedrich-Schiller-Universität Jena, Jena, Germany; [4]TU-Darmstadt, Darmstadt, Germany; [5]School of Mathematics and Physics, Queens University Belfast, UK

A main research topic of the upcoming FAIR-facility focusses on the study of warm dense matter (WDM) states. Proton and light-ion beams generated with high-intensity lasers play an important role in this field as they can be used either as a WDM driver [1] or as a diagnostic tool. These applications require high particles numbers and a highly energetic particle beam. Despite very positive estimates delivered by numerical simulations, a significant discrepancy is found in the experimental realization so far, which requires further investigations. This motivates a series of experimental campaigns using PHELIX to determine the scaling of proton generation with parameters like laser intensity, or laser temporal contrast.

The performance of the laser system has been evaluated by scanning different laser and target parameters and measuring the maxmum reachable proton energy. The results, showing the scaling of the proton energy for different laser intensities, can be seen in figure 1. We initially used 300-nm-thick CH_2 targets for the proton acceleration, which showed a maximum proton energy in simulations done for the PHELIX parameters [2].

Using the standard copper parabola as a focusing optic (black points, figure 1), enabled intensities up to $3 \cdot 10^{20}$ W/cm² on target, accelerating protons up to 80 MeV. When switching to the glass parabola the intensity could be increased up to $5 \cdot 10^{20}$ W/cm² (red and blue points). Due to the increased intensity, the thin targets undergo a significant pre-expansion, which limits the maximum reachable proton energy. This obstacle was overcome by increasing the target thickness to 1.5 µm (red points).

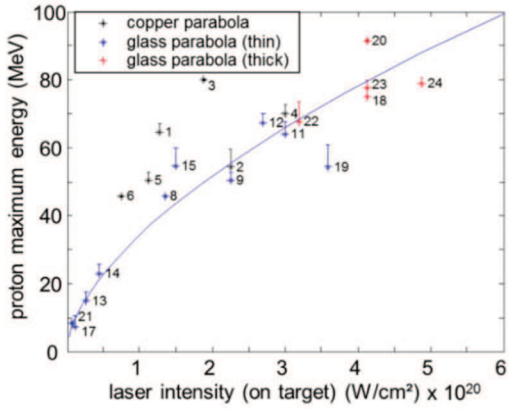

Figure 1: Maximum proton energy for different laser intensities on target. The different colors indicate the use of different focussing optics and target thicknesses.

Due to the higher intensity on target, record-high maximum proton energies of at least 90 MeV have been observed. The square root scaling of proton energy and intensity (blue curve) fits for both thickness parameters, indicating target normal sheath acceleration (TNSA) as the main acceleration mechanism for both regions. The Radiochromic film (RCF) of the record-shot, used to measure the particle energy, can be seen in figure 2. It shows a proton signal at 90 MeV covered by a strong electron background extending to the 96-MeV film and beyond. This aggravates the analysis of the RCF and the estimation of the maximum reached proton energy.

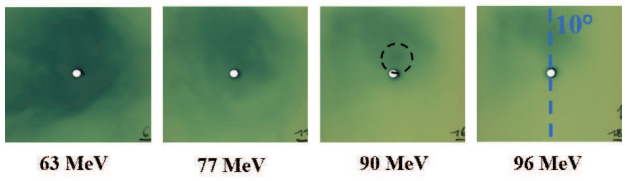

Figure 2: Radiochromic films showing the record proton energy for the PHELIX facility above 90 Mev (black circle). The films show a strong electron background covering the signal at energies beyond 90 MeV.

To reduce the pre-expansion of the targets when such intensities are used, and therefore enable different acceleration mechanisms, an improved temporal contrast is needed. We improved the contrast of the laser system by four orders of magnitude and reduced the rise time of the pulse by using a double plasma mirror. This setup changes the interaction nature between target and laser, enabling a fully opaque interaction for targets above 50 nm, for example. Despite similar intensity conditions, the maximum reachable proton energy is significantly reduced. This effect could occur due to reduced absorption and therefore a decrease of the coupling efficiency of laser energy into particles.

This strong change in the interaction was also observed by advanced optical diagnostics, measuring the time resolved spectrum of the transmitted and back-reflected light during the interaction, as well as the reflectivity and transmissivity of the plasma. This will give additional insight into the relativistic laser plasma interaction, enabling possibilities to reach proton beam parameters necessary for the upcoming applications.

References

[1] K. Schoenberg, et. al., Emmi Workshop Report: Plasmaphysics at FAIR 2017, 10.15120/GSI-2019-00611, 2017

[2] F. Wagner, et. al., Maximum Proton Energy above 85 MeV from the Relativistic Interaction of Laser Pulses with Micrometer Thick CH_2 Targets, Phys. Rev. Lett. 116(20), 2016

Overview of achieved proton beam parameters using the laser-driven ion beamline (LIGHT)

D. Jahn[1,2], D. Schumacher[2], C. Brabetz[2], J. Ding[1], R. Leonhardt[1], F. Kroll[3,4], F.E. Brack[3,4], U. Schramm[3,4], A. Blazevic[2,5], and M. Roth[1]

[1]Technische Universität Darmstadt, Darmstadt, Germany; [2]GSI Helmholtzzentrum für Schwerionenforschung, Darmstadt, Germany; [3]Technische Universität Dresden, Dresden, Germany; [4]Helmholtzzentrum Dresden-Rossendorf, Dresden, Germany; [5]Helmholtz-Institut Jena, Jena, Germany

The LIGHT collaboration combines laser-driven ion sources with conventional accelerator technology for the beam shaping of laser-driven ion beams. Therefore, a test beamline was realized at the GSI Helmholtzzentrum für Schwerionenforschung GmbH. Figure 1 presents its scheme, which is based on a laser-driven ion source, two pulsed high-field solenoids and an rf cavity. This report presents the achieved proton beam parameters. Especially, the parameters at the interaction point for future applications are specified, which is 6 m behind the source.

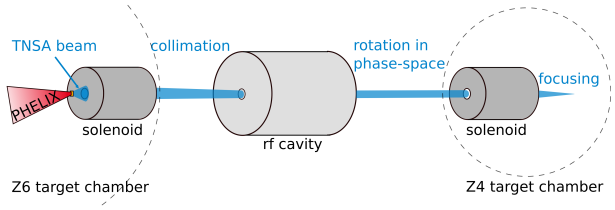

Figure 1: Scheme of the laser-driven ion beamline

The PHELIX laser ($\lambda = 1053$ nm, $\tau = 650$ fs, E ≈ 15 J) was focused on a 10 μm thin gold target with a focal spot size of 3.5 x 3.5 mm^2 driving the TNSA mechanism. The source characterization with an RCF stack showed an exponentially decaying spectrum with a cut-off energy of $\approx$21.5 MeV. The fit p arameters of dN/dE = N_0/E exp(-E/k_BT) were the maximum number of protons $N_0 = (4.48 \pm 1.10) \times 10^{11}$ and the temperature k_BT = (19.35$\pm$8.64) MeV. Analysing the spectrum, the half envelope divergence angle had a value up to $\approx$28° directly behind the target.

The generated beam was collimated with the first solenoid, which was positioned 4 cm behind the source and was operated at 6.5 T. A central energy $E_0 = 9.6$ MeV was selected. An Gaussian energy distribution with an energy spread of ΔE=(18$\pm$3)% at FWHM was measured [1].

Afterwards, the beam is injected into an rf cavity. Inside this element, the beam is rotated in longitudinal phase space around its central energy. For the ideal phase rotation, a beam injection at a synchronous phase Φ_s=90° is desired. Through setting the rf amplitude, the proton beam can be energy-compressed to a few percent spread or temporally focused in a certain distance. The energy compression was measured with a dipole spectrometer and showed an energy spread of ΔE=(2.7$\pm$1.7)% (FWHM) around a central energy of E_0=(9.7$\pm$0.1) MeV [1].

For temporal compression, proton bunch durations below 600 ps were reproducibly measured. With the current setup, a duration of τ_p =(593$\pm$40) ps was measured with a specially developed diamond detector [2].

The last step in beam shaping is the final transverse focusing system by a second solenoid, which was operated at 5.8 T. The beam was collimated with the first solenoid and transported without an operating rf cavity along the beamline. In a distance of 6 m from the source, the beam was focused down to a round-shaped focal spot size of 1.1 mm x 1.2 mm at FWHM containing $(3.5 \pm 0.22) \times 10^8$ protons [3]. In future, the phase rotation (energy compression or temporal focusing) and final focusing will be demonstrated simultaneously. Using temporal focusing, this will enable proton intensities up to 5.8 x 10^{19} protons/(s$\times$cm^2). Table 1 summarizes the important experimental achievements.

parameters of	**experimental achievements**
TNSA source	exponential spectrum, $N_0 = 4.5 \cdot 10^{11}$, $k_BT = 19.4$ MeV, divergence up to 27.7°
collimation	$E_0 = (9.7 \pm 0.1)$ MeV, $\Delta E = (18 \pm 3)$% (FWHM)
energy compression	$E_0 = (9.7 \pm 0.1)$ MeV, $\Delta E = (2.7 \pm 1.7)$% (FWHM)
temporal focus	τ_p = (593 $\pm$ 40) ps (FWHM)
transverse focus	A = 1.1 mm x 1.2 mm at FWHM

Table 1: Overview of achieved beam parameters

References

[1] S. Busold, D. Schumacher, C. Brabetz, D. Jahn, F. Kroll, O. Deppert, U.Schramm, T. E. Cowan, A. Blažević, V. Bagnoud, M. Roth: Towards highest peak intensities for ultra-short MeV-range ion bunches, Scientific Reports 5, 1 (2015)

[2] D. Jahn, M. Träger, M. Kis, M. Ciobanu, M. Pomorski, C. Brabetz, D. Schumacher, U. Bonnes, S. Busold, Blažević und M. Roth: Chemical-vapor deposited ultra-fast diamond detectors for temporal measurements of ion bunches, Rev. Sci. Instrum. 89, 093304 (2018)

[3] D. Jahn, D. Schumacher, C. Brabetz, F. Kroll, F.-E. Brack, J. Ding, R. Leonhardt, I. Semmler, Blažević, U. Schramm, M. Roth: Focusing of multi-MeV, subnanosecond proton bunches from a laser-driven source, Phys. Rev. Accel. Beams 22, 011301 (2019)

PIC Simulation of laser irradiated Micro-Plasma with varying density*

V. Pauw† [1,2], *P. Hilz*[1], *J. Schreiber*[1], *and H. Ruhl*[2]
[1]LMU, Munich, Germany; [2]LRZ, Garching, Germany

We present a preliminary result of our current work in which we use particle-in-cell simulations to investigate the fast ions produced by irradiating hydrogen-clusters (μm-radius) with short ultra-strong laser pulses (30 fs FWHM, 100 J).

Computational Set-Up and Resource Use

The simulation domain in our set-up measures 36x36x64 microns, 2304x4032 grid cells, a grid cell width of 15,625 nm (64 points per laser wavelength at $\lambda = 1000nm$). A cell contains 10 quasi-particles. They are run on the HPC system SuperMUC at LRZ in Garching (Munich) on 8192 compute nodes.

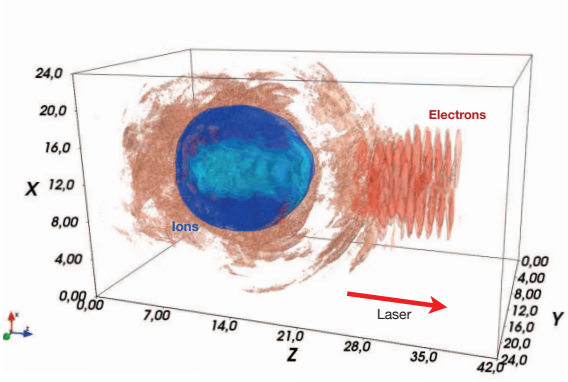

Figure 1: A PIC simulation of ion acceleration in a laser irradiated micro target

Varying the Density of a Proton Target

Scanning a region of densities from $2n_c$ (n_c is the non-relativistic critical electron density) to solid densities ($228n_c$), we observe different acceleration mechanisms. At very low and very high densities (below $5n_c$ or over the relativistic transparency threshold $n_e > n_c/\sqrt{1+a_0^2/2}$), a predominantly isotropic expansion/coulomb explosion takes place which produces inferior energies and beam directionality. In the region of relativistic transparency, a collisionless shock forms at the irradiated target side and transverses the interior, gaining further momentum from the coulomb explosion reaching energies up to 360 MeV.

Target size and density are varied while the laser focal spot is matched to the sphere size for optimal energy transfer. The density scan is done for a short (30fs) and a long

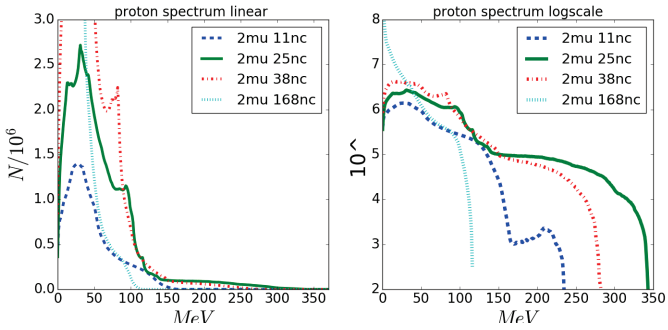

Figure 2: Spectral plot of accelerated ions for the $2\mu m$ target (number of protons per MeV)

(90fs, FWHM field intensity) gaussian pulse for three target sizes (1333 nm, 2000nm and 3000nm radius) targets. Varying a_0 for the different pulse lengths and focus sizes keeps the total pulse energy constant. Figure 3 shows the maximal proton energies obtained in the density scan for the different target types.

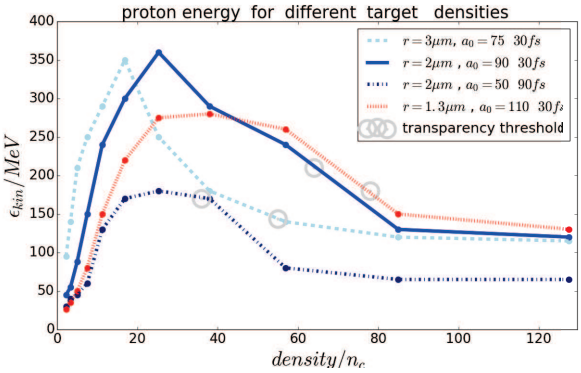

Figure 3: Maximal proton energy at different densities (multiples of the critical electron density n_c for different target and laser parameters

References

[1] K. Germaschewski, H. Ruhl, A.Bhattacharjee, , et al "The Plasma Simulation Code: A modern particle-in-cell code with patch-based load-balancing", Journal of Computational Physics 318 (2016)

[2] T.M. Ostermayr , et al, 'Proton acceleration by irradiation of isolated spheres with an intense laser pulse", Phys. Rev. E 94, 033208 (2016).

[3] P. Hilz, et al "Isolated proton bunch acceleration by a petawatt laser pulse", Nat. Comm. (2018)9:423.

* Computing resources provided by GCS project pr74si
† viktoria.pauw@physik.uni-muenchen.de

Towards neutron resonance imaging with laser-driven neutron sources

A. Kleinschmidt[1,2], S. Aumüller[3], M. Zimmer[3], and M. Roth[3]
[1]GSI, Darmstadt, Germany; [2]HI Jena, Jena, Germany; [3]TU Darmstadt, Darmstadt, Germany

Introduction

Conventional neutron sources, such as fission reactors or accelerator-based spallation sources, are well established and utilized in a wide field of applications. However, they also have their disadvantages and limitations. These include inflexibility, a high radiation background, and limited neutron pulse duration. In contrast, laser-driven neutron sources provide a cost-efficient and compact complement to large-scale neutron facilities, allowing their installation in small institutions and their transport to analyze unmovable objects, such as buildings and sensitive archeological material.
Neutron imaging is a useful technique to identify the position of objects inside a compound. Resonance imaging additionally enables the identification of different elements and isotopes on the detected images. This technique could become important for the investigation of heated or shocked materials in the warm dense matter state, for example used in experiments at the future FAIR facility. Especially the properties of low-Z materials encapsulated in a high-Z case are not accessible with established methods, such as X-ray or proton diagnostics. The application of very short neutron pulses however, could be the clue to studying these transient states of matter, e.g. inside a LAPLAS target [1].

Experimental results

The experiment was conducted at the PHELIX laser at GSI Helmholtzzentrum für Schwerionenforschung GmbH. Neutrons were generated by nuclear reactions of laser-accelerated protons and deuterons inside a beryllium catcher. A moderator made of high density polyethylene (HDPE) was used to slow down the high-energy component of the emitted neutron spectrum. A sketch of the setup is shown in Figure 1.

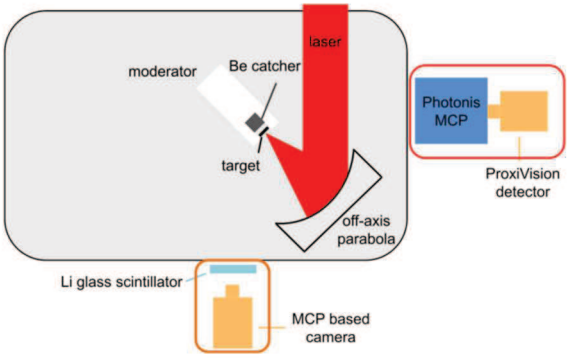

Figure 1: Experimental setup with the positions of the two imaging detectors.

* Work supported by EU, EURONS contract No. 506065.

Different sample materials were investigated by neutron imaging within various time intervals. The images were recorded with two independent detector systems, one based on a two-step boron-doped microchannel plate (MCP) system, the other working with a lithium glass scintillator. Boronated HDPE was used as a collimator to limit the field of view from the source to the detector. The samples were placed directly in front of the detector systems. Figure 2 displays an accumulated background-corrected neutron image of a 1mm cadmium and a 1mm indium sample measured with the boron-doped MCP detector system. The exposure time was about 760µs, covering an energy range from 9.9meV to 1.97eV and thus the most pronounced resonances in the neutron reaction cross sections of both materials. The neutron attenuation inside the samples, resulting in darker areas on the imaging system, is clearly visible.
A resonance radiography measurement was not possible in this experiment, as the emitted neutron numbers were more than one order of magnitude lower compared to previous campaigns at PHELIX [2].

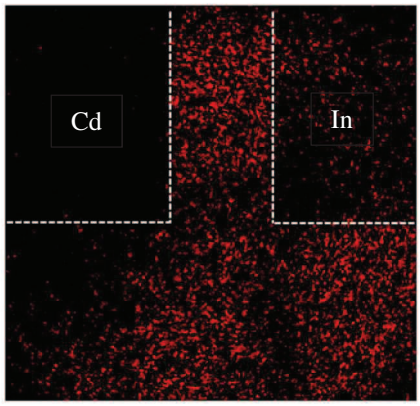

Figure 2: Over three shots accumulated neutron image of a 1mm cadmium (upper left corner) and a 1mm indium (upper right corner) sample.

Similar images were obtained with the lithium-glass detector system, underlining the reliability of our results. Despite lower neutron numbers compared to similar experiments, the clear distinction of the samples in our measurements reinforces the feasibility of a laser-driven neutron source for neutron imaging applications.

References

[1] N. Tahir et al., *Phys. Lett. A* **249**, 489-494 (1998)
[2] A. Kleinschmidt et al., *Phys. Plasmas* **25**, 053101 (2018)

Prospects of Laser-Based Neutron Sources for Neutron Resonance Spectroscopy

M. Zimmer[1], A. Kleinschmidt[2,3], S. Scheuren[1] and M. Roth[1]
[1]TU Darmstadt, Darmstadt, Germany, [2]GSI, Darmstadt, Germany, [3]HI Jena, Jena, Germany

Introduction

In recent years the demand for small sized neutron sources has grown immensely, which is caused by several factors. On one side, as technology advances, structures become more complex and an in-situ diagnostic is required that promises a sensitivity to small material variations while maintaining a high transmission range. On the other side, safety is a great concern in our days and at great transshipment points many containers move from country to country without the possibility to identify fissile materials or certain explosives.

Neutrons are able to solve both problems as they are capable of penetrating deep into samples since they do not interact electromagnetically. They are also highly sensitive to variations in the isotopic mass number inside the probed object. This can not only be used to identify materials but also to trace them back to their origin since isotopic compositions vary strongly depending on geographic composition.

While conventional neutron sources are large in size, expensive and produce strong background radiation with large pulse widths, it is more desirable for this purpose to have additional sources, that are smaller, transportable and with short pulse lengths.

With laser-based neutron sources this advantage can be achieved and with the current development of lasers, the amount of neutrons per pulse will be increasing drastically in the next years as well as will be the repetition rate of the upcoming laser systems all over the world. This will soon lead to a point where laser-based neutron sources will become a serious competition to existing sources because they provide capabilities and opportunities where conventional sources have their limits.

Experimental results

In August 2018, an experimental campaign at the PHELIX laser facility was conducted in which sub µm deuterated polymer foils were irradiated with a short laser pulse (200 J, 500 fs, 4 µm focus diameter). The produced deuterons were directed onto a beryllium catcher to convert them into neutrons via nuclear processes. For the shielding of the beryllium against ablation from the laser plasma, a 1mm layer of Kapton poly-amide was inserted between target and catcher. Kapton does have the advantage that its components, mainly carbon, do have a high neutron yield when irradiated with deuterons while at the same time being very robust against high temperatures.

The produced neutrons were decelerated by the use of a high density polyethylene moderator surrounding the catcher. The emitted neutrons do follow a 1/E energy dependence towards higher energies and can be used for neutron resonance spectroscopy. The detector used to observe the neutron spectrum was a borated multi channel plate which has a fast response time below 10ns and a high thermal detection efficiency which decreases with $1/E^{0.5}$. In figure 1 the neutron spectrum before and after the correction of the 1/v dependency can be seen in comparison to a FLUKA simulation of the same experiment. Although there is a good agreement between simulation and experiment in the thermal region, the epithermal neutrons decrease much faster than with $1/E^{1.32}$ in comparison to the $1/E^{0.94}$ predicted by the simulation. This is most probably explained by an over saturation of the detector during the γ – flash produced by the laser-target-interaction.

Although total neutron numbers up to $5*10^{10}$ were expected, a pre-pulse in the laser system 1.4 ns before the main pulse damaged the target, so about a factor of 25 times less neutrons were produced. With this low neutron number, the original goal of resolving the nuclear resonance of ^{182}W with high enough accuracy to determine the temperature from Doppler broadening, could not be archived. Nonetheless it was possible to identify an absence of neutrons at the resonant energies. With an increased contrast and in addition to that, thinner tungsten samples, it will not only be possible to identify materials via laser-based neutron resonance spectroscopy but as well measuring the temperature of shocked materials which is of high scientific interest[1].

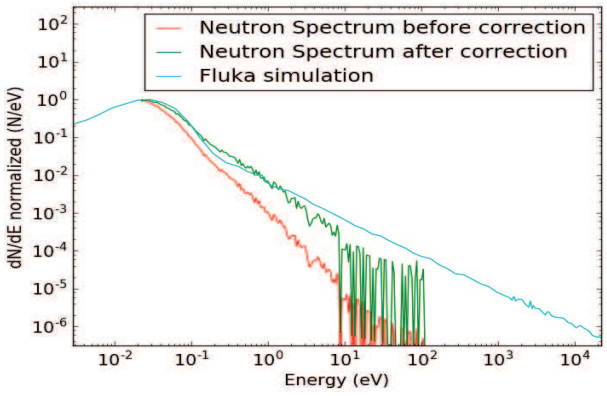

Figure 1: Comparison of the detected, corrected and simulated neutron spectrum.

References

[1] J. C. Fernández et al., LA-UR-18-20686 DOI: 10.2172/1419717 (2018)

Collimated electron beam generation in relativistic laser-solid interaction*

I. Tsymbalov[1,2], D. Gorlova[1,2], A. Zavorotniy[1], S. Shulyapov[1], K. Ivanov[1], R. Volkov[1], and A. Savel'ev[1]

[1]Faculty of Physics and International Laser Center, M.V. Lomonosov Moscow State University, Moscow, Russia;
[2]Institute for Nuclear Research of the Russian Academy of Sciences, Moscow, Russia

Laser-plasma interaction is now routinely used to accelerate electrons to high energies (up to several GeV [1]). This allows laser-plasma based sources to be considered as compact and relatively low-cost accelerators and leads to a wide range of potential applications, such as Thomson and bremsstrahlung X-ray sources, laboratory astrophysics, ultrafast electron microscopy to name a few. For many of these applications it is of great importance to generate electrons in the form of a beam with a relatively small divergence and a narrow energy spectrum i.e. having parameters comparable to those of a beam at a traditional accelerator.

Here we present experimental research on the electron bunch generation at intensity around 10^{18} W/cm^2 in a long-scale undercritical plasma, formed by additional nanosecond laser pulse with controlled parameters. Choosing appropriate parameters of main laser pulse and artificial prepulse we can change interaction regimes and thereby optimize beam parameters for different applications.

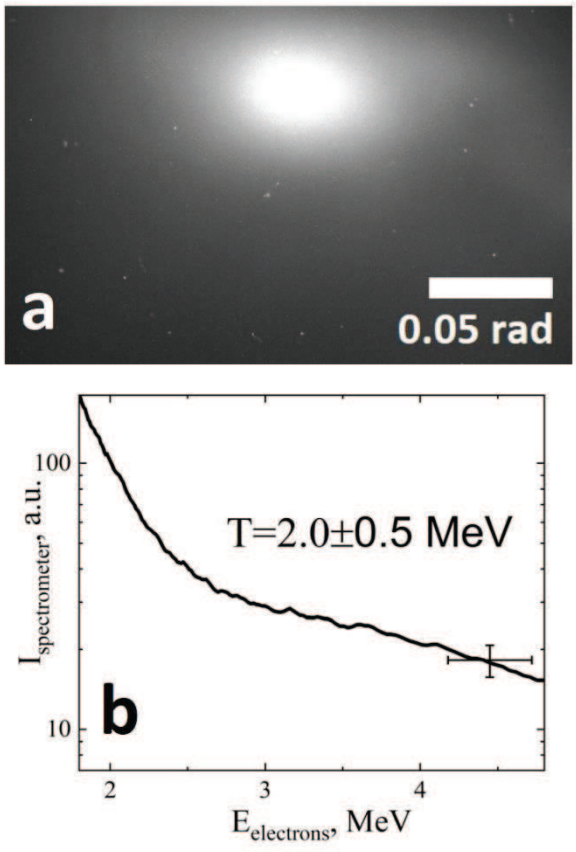

Figure 1: Electron beam spatial profile (a) and energy spectra (b)

In our experiments we used Ti:Sapphire laser system (800nm, 10Hz, 40mJ, 45±5fs, $5\cdot10^{18}$ W/cm^2, level of contrast on ps time scale – 10^{-8}). Laser radiation was focused by off-axis parabolic mirror (F~5cm) onto the target. To create pre-plasma layer on the target surface we used Nd:YAG laser (1064nm, 10Hz, 200mJ, 6 ns, 10^{12} W/cm^2, level of contrast on ns time scale – 10^{-5}). Varying delay between main pulse and prepulse we changed preplasma scale in the large range of values. All experiments were performed in a vacuum chamber at a pressure not higher than 10^{-2} Torr. Spatial distribution of hot electrons was visualized by the LANEX screen and detected by CCD camera. To measure electrons energy spectra, we used magnetic spectrometer. We also measured electron beam charge by two different methods: directly by using a simple Faraday cup (3 cm copper cylinder with a 1 nF capacitor and 130 μm W filter to cut off electrons with E<1 MeV) and indirectly via measuring neutron production in (γ,n) photonuclear reaction in beryllium. To detect neutrons, we used an array of ^{3}He-counters and a polyethylene moderator.

It is shown that by optimizing preplasma profile one can obtain collimated (~0.05 rad) electron beam with temperature around 2 MeV [2]. The beam charge was 30±10 pC (for Faraday cup measurements) and 10±4 pC for neutron yield measurements (E>1.7 MeV, as it's the reaction threshold). Both charge values are in good agreement with each other. The mechanism that leads to the additional collimation of electron beam is considered to be direct laser acceleration (DLA) in plasma channel formed in long low-density preplasma corona.

Using this beam, we had started research on excitation of spin isomers in the pygmy-resonance region [3]. We're also planning on implementing it to create a positron source on our setup. According to GEANT4 simulation, the flux of low-energy (up to few MeV) positrons can be as high as 10^6 s^{-1} for electron temperature of 2 MeV, which is enough to be considered useful for practical applications.

References

[1] K. W. D. Ledingham and W. Galster, "Laser-driven particle and photon beams and some applications", New J. Phys. 12 (2010)

[2] I. Tsymbalov et.al., "Well collimated MeV electron beam generation in the plasma channel from relativistic laser-solid interaction", accepted to Plasma Physics and Controlled Fusion (2019)

[3] V. Nedorezov et. al., "Photoexcitation of spin isomers of In and Cd nuclei in the pigmy resonance region", Physica Scripta, 94(1), p.015303 (2019)

* Work supported by RFBR grants 19-02-00104 and 18-32-00416.
#ivankrupenin2@gmail.com

Simulations of hard X-ray generation by hot electrons in silver targets

*O. F. Kostenko**
JIHT RAS, Moscow, Russia

To radiograph substances with a high energy density, use is made of X-rays in the 10–100 keV range. Radiographing the dense plasma which is to be produced by heavy ion beams on the FAIR under construction calls for X-rays with photon energies above 100 keV. In Ref. [1] we determined a two-temperature hot-electron energy distribution function by modelling the data of bremsstrahlung and K_α radiation measurements for silver targets with no recirculation of hot electrons, which were produced by s-polarised subpicosecond laser pulses with a peak intensity of about 2×10^{19} W/cm^2 on the PHELIX laser facility. The temperature of the high-energy component is described by the ponderomotive scaling. The temperature of the low-energy component is well below the ponderomotive scaling and the Beg's law. We obtained relatively low conversion efficiency of laser energy into the energy of hot electrons propagating through the solid target of about 2%.

In the present work [2], we consider a semi-analytical model of X-ray bremsstrahlung generation in metallic targets with the inclusion of hot electron recirculation. We calculated the yield of X-ray bremsstrahlung in the 10–100 keV and 0.1–1 MeV photon energy ranges as well as the yield of 22.1-keV K_α radiation from the front and rear sides of silver targets of different thickness, with and without the inclusion of hot electron recirculation. The effect of hot electron recirculation in thin foils was shown to significantly improve the K_α radiation and bremsstrahlung yields in the 10–100 keV photon energy range. By contrast, the bremsstrahlung photon yield in the 0.1–1 MeV energy range from 10–20 μm thick foils, in which the hot electrons recirculate, corresponds approximately to the photon yield from the rear sides of 1–2 mm thick targets, in which the recirculation is insignificant (Fig. 1).

To radiograph cylindrical samples, use is made of foils of about 10 μm thickness, which makes it possible to measure the density of Warm Dense Matter with a high spatial resolution. The laser-to-K_α radiation energy conversion coefficient with the use of a 10-μm thick silver foil, in which the recirculation is implemented, amounts to 3×10^{-5}. This is consistent with the data obtained on the Titan laser facility [3]. The ratio of the number of K_α radiation photons emitted from the front surface of the above target to the number of bremsstrahlung photons in the 1.8-keV wide range centred at the K_α radiation photon energy of 22.1 keV is equal to 10. This estimate of the spectral contrast of the K_α radiation is also consistent with the data of Ref. [3].

When use is made of the specified target, the hot electron to 10 keV–1 MeV bremsstrahlung energy conversion efficiency is equal to 2.7%, the 0.1–1 MeV range accounting for 73% of the bremsstrahlung energy. In view of the efficiency of laser energy conversion to the energy of hot electrons that penetrate deep into the target, $\eta_{\mathrm{L}\to\mathrm{e}} = 2\%$ [1], the laser to 0.1–1 MeV bremsstrahlung energy conversion efficiency is 4×10^{-4}. As follows from Ref. [4], with this conversion efficiency it is possible to obtain high-quality radiographic images of millimetre-sized lead samples heated by heavy ion beams to a high energy density state.

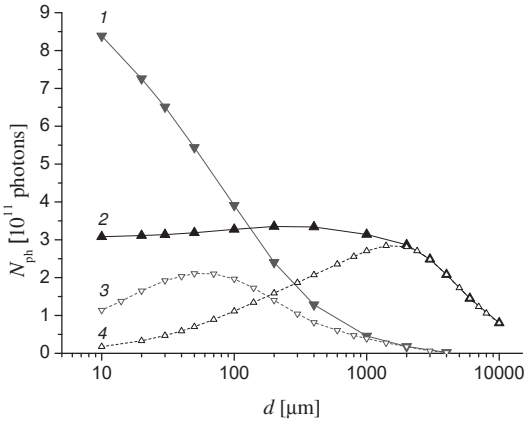

Figure 1: Photon yield, in relation to the target thickness, from the rear side of the silver target in the energy intervals (*1*, *3*) 10–100 keV and (*2*, *4*) 0.1–1 MeV with (*1*, *2*) and without (*3*, *4*) the inclusion of hot electron recirculation.

To summarise, we note that an order of magnitude higher $\eta_{\mathrm{L}\to\mathrm{e}}$ coefficient was obtained in Ref. [5] in the oblique incidence of p-polarised picosecond laser pulse of close intensity 3×10^{19} W/cm^2 on a 5-μm thick aluminium foil (it was placed in front of a silver foil in a multilayer target, in which there was no recirculation of hot electrons). The prospect of obtaining an order of magnitude higher laser to 0.1–1 MeV bremsstrahlung energy conversion efficiency with the use of a layered target consisting of aluminium and silver foils with the recirculation of hot electrons lends impetus to further research.

References

[1] O. F. Kostenko, N. E. Andreev, O. N. Rosmej, Phys. Plasmas **25** (2018) 033105.

[2] O. F. Kostenko, Quantum Electronics **49** (2019) 216.

[3] B. Westover et al., Phys. Plasmas **17** (2010) 082703.

[4] K. Li et al., Laser Part. Beams **32** (2014) 631.

[5] B. Vauzour et al., Phys. Plasmas **21** (2014) 033101.

* olegkost@ihed.ras.ru

Studies in High Density Degenerate Plasma

Punit Kumar, Shiv Singh and Nafees Ahmad
Department of Physics, University of Lucknow, Lucknow, Lucknow-226007, India

The growing interest in investigating new aspects of high density (quantum) plasmas is motivated by its potential applications in modern technology e.g., quantum well and quantum dots, quantum plasma echoes, metallic nanostructures, microelectronics devices, thin metal films, metal clusters, nano-plasmonic devices, quantum x-ray free electron lasers, in high intensity laser produced plasmas, in nonlinear quantum optics, in metallic nanostructures, in super dense astrophysical environment (e.g. in the interior of Jupiter, white dwarfs, and neutron stars), in dusty plasmas and in next generation of laser based plasma compression experiment (LBPC), etc. The studies involving interaction of intense laser beams with quantum plasma were carried out by the quantum plasma group.

Studies using QHD Model

The interaction models were developed on the recently developed quantum hydrodynamic (QHD) model which consists of a set of equations dealing with transport of charge, momentum and energy in a plasma. The effects of quantum Bohm potential, the Fermi statistical pressure and the electron spin were incorporated.

Third Harmonic Generation in Magnetized Quantum Plasma

Study of third harmonic generation resulting from propagation of circularly polarized laser beam in homogeneous high density quantum plasma immersed in an externally applied magnetic field was carried out. The oscillatory electron velocities, perturbed density and non-linear current density for the propagation of laser beam in high density plasma were setup. The field amplitude of third harmonic of the whistler with respect to fundamental wave and the conversion efficiency for phase-mismatch was analyzed and higher conversion efficiency was observed in degenerate plasma for lower values of static magnetic field as compared to classical plasma.

Acceleration of Electrons in Quantum Dusty Magnetoplasma

A detailed study of ponderomotive acceleration of electrons in magnetized quantum dusty plasma was performed. A simple energy exchange solution in electron acceleration was established. It is noticed that the electron acceleration by circularly polarized laser pulse is significantly affected by presence of magnetic field, laser field amplitude and dust charge grains. It is found that an electron gains energy during rising part and losses energy during trailing part of laser pulse and presence of dust grains increase the growth of ponderomotive acceleration in quantum dusty plasma as compare to quantum plasma.

Studies using SSE-QHD Model

All the prevalent models considered electrons as a single fluid of macroscopically averaged spin-1/2 plasma. The earlier papers did not show a full picture and didn't took spin-up and spin-down interaction force into account. Very recently, a modified separate spin evolution (SSE) treatment of electrons in accordance with Pauli equation has been developed.

Surface Plasma Wave in Semiconductor Quantum Plasma

A scheme of stimulated SPW excitation in magnetized quantum plasma via stimulated electron-hole recombination in the proximity of the guiding surface was proposed. The dispersion and pointing flux of the surface plasma wave in quantum magnetized plasma was evaluated. It was found that the dispersion and pointing flux properties differ slightly in spin-polarized and unpolarized plasmas. The electron-hole instability of semiconductor in quantum plasma with the spin-polarization can be a problem of interest but we left for a future work. This result may be important for the ultra-small electronic devices like travelling wave amplifier and solid density plasmas.

Electron-Hole Instability in Semiconductor Quantum Plasma

The Instability of electron-hole in quantum semiconductor plasma was examined. The growth rate of the wave depends on varying the parameters normalized by cyclotron- plasma frequency, like the angle between propagation vector and external magnetic field parallel to and speed of the externally injected electron beam parallel to the propagation vector. We derived a dispersion relation from which it was shown that inclusion of streaming effects in finite geometry opens up the possibility of a number of wave modes. Some of these modes were found to be linearly unstable. It has been shown that the finite boundary, stream velocity of plasma particles, quantum diffraction parameter, electron-hole mass ratio and the charge imbalance parameter all have significant effects on the instability growth rate.

Filamentation of a Short Laser Pulse

Filamentation of a short laser pulse in a magnetized quantum plasma was studied. The direction of the external field has been taken to be along the direction of electron beam propagation in the first case and oblique in the second case. The dispersion for both the cases have been obtained and growth rate evaluated. The numerical analysis for growth rate has been carried out. The results of both the cases have been compared and analysed.

Comparison has also been done with earlier studies and the difference is critically analysed and interpreted. The Filamentation instability of a short pulse laser in magnetized quantum plasma is significantly enhanced by the ambient magnetic field. The growth rate is increase with spin polarization in case of longitudinal wave, but in case of oblique the growth rate is reduced with the increase angle. The growth rate increase with magnetic field strength and the laser intensity. The growth rate in fully polarized plasma is about 18-24% more than that in unpolarized quantum plasmas.

Circularly Polarized Modes in Dusty Quantum Plasma

The possibilites of circularly polarized mode due to propagation of electromagnetic wave in quantum dusty magnetoplasma with two different spin states of electrons were explored. The longitudnal dispersion relation for electromagnetic waves in dusty magnetoplasma was setup. The right circularly polarized, left circularly polarized wave, ordinary mode and extra-ordinary mode were analyzed. Growth rate was calculated and effect of spin polarization was studied. It has been observed that the e. m. wave is more dispersed in spin polarized plasma than unpolarized plasma because the Fermi pressure is about 1.6 times than that of unpolarized electrons. The frequency of left circularly polarized wave is more by about 16% in spin polarized quantum dusty plasma than unpolarized quantum dusty plasma and the frequency of right circularly polarized wave is more by about 20% in spin polarized quantum dusty plasma than unpolarized quantum dusty plasma.

Simulation Studies

QED cascade structure in the field of a standing linearly polarized wave was studied in collaboration with Prof. A. V. Kim and A. Bashinov from Institute of Applied Physics, Nizhny Novgorod, Russia. Based on the numerical modelling of the electron dynamics in the focal region of a dipole wave, we have found the confinement time of electrons in the region of the strongest electric field in a wide (up to 200 PW) power range. By comparing confinement times of particles and the spatial structures of their escape, we have determined the regimes of ponderomotive escape and radiation dominated escape corresponding to normal and anomalous radiative trapping, as well as the threshold powers of these regimes. It is shown that in the regimes of ponderomotive escape, the confinement time decreases with increasing power and stabilises at the level of one third of the wave period with the particles leaving the focal region predominantly across the electric field. In the radiation dominated regime, the confinement time, on the contrary, increases with increasing power, the rate of transverse particles' escape decreases, and the particles leave the focal region in the form of compact beams.

High Intensity Stored Beams of ^{238}Th and the Excitation of the Isomeric State at 7.6 eV

Shizeng Zhang and Dieter H.H. Hoffmann

Xi'an Jiaotong University, School of Science, Dept. Laser and Particle Beams, Xi'an 710049, P.R. China
National Research Nuclear University MEPhI, Moscow, Russia

Atomic clocks are currently our most precise timekeepers and could be accurate to within a single second in 20 billion years, while a greater level of accuracy could be achieved with the help of the nuclear clock, based on oscillations in the atomic nucleus itself rather than oscillations in the electron shells surrounding the nucleus. Due to technical reasons such a level must be within reach of available lasers to set up a frequency comb. At the moment the only nuclear level known and predicted by theory is the M1 nuclear transition between the low-energy isomeric state and the ground state in the ^{229}Th nucleus, with the energy approximately 7.6 eV [1].

In order to get more knowledge about this isomeric state, we made a calculation about the excitation cross-section of the ^{229}Th when a beam of high charged ^{229}Th circulating in a storage ring with a ^{12}C target:

$$\sigma_0 = \int \sigma_{ph}(\varepsilon) d(\varepsilon) = n_i \frac{2\pi^2 e^2 \hbar}{mc}$$

$$\sigma_{exc} = \int \sigma_0 N_{ww}(\varepsilon) \frac{\Gamma/2\pi}{(E - E_{Res})^2 + (\Gamma/2\pi)^2} d\varepsilon$$

where

$$N(\hbar w) = \frac{2\alpha}{\pi} \frac{Z^2}{\beta^2(\hbar w)} [\ln(\frac{1.123\beta\gamma\hbar c}{(\hbar w) b_{min}}) - \frac{\beta^2}{2}]$$

is the number of virtual photon which are used to describe the intense electromagetic pulse generated by the fast charge particles with the relativistic velocity during the collision.

As shown in Figure 1, in the low frequency limit there is a high number of low energy level photons, and $N(\hbar w = 7.6eV) \simeq 10^{18}$, then we could find the cross-section at 7.6 eV is $\sigma_{exc} \sim 10^{-8} cm^2$, which is a quite large number. If we consider a target with the thickness 1 cm, the excitation rate will be about $\lambda_{exc} \sim 10^{15}$ while the decay rate of the isomeric state is about $\lambda_{dec} \sim 10^5$ when the half-life of the ^{229m}Th is around 7.5 μs [2] .It is obvious that $\lambda_{exc} \gg \lambda_{dec}$,which means that nearly all the Th nucleus will be excited to the isomeric state at an extremely short interval while the number of stored Th particles is 10^4.

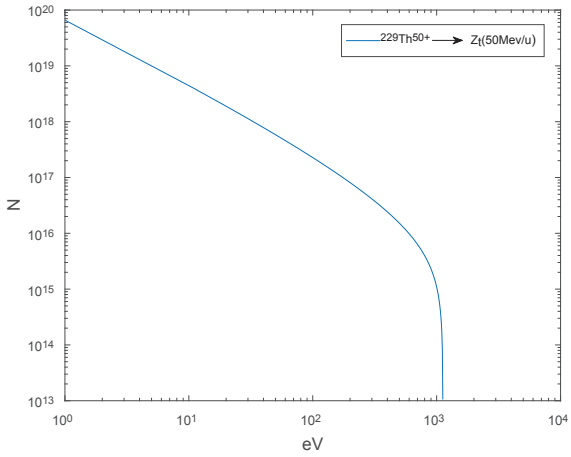

Figure 1: Virtual photon spectrum of ^{229}Th^{50+} at 50 MeV/u

Next some experiments will be performed to check whether the simulation is reasonable or not.

References

[1] B.R.Beck et al.,Phys.Rev.Lett.98,142501(2007)

[2] Seiferle et al.,Phys.Rev.Lett.118,042501(2017)

5 Fusion related Issues of Plasma Physics

Thermonuclear ignition and the onset of propagating burn in inertial fusion implosions

A. R. Christopherson[1,3],R. Betti[1,2,3], S. Miller[1,3], V. Gopalaswamy[1,3], J. D. Lindl[4]

[1]Dept. Mechanical Engineering, University of Rochester, Rochester NY 14627
[2]Dept. Physics and Astronomy, University of Rochester, Rochester NY 14627
[3]Laboratory for Laser Energetics, University of Rochester, Rochester NY 14623
[4]Lawrence Livermore National Laboratory, Livermore, California 94550, USA

A large effort is currently under way to demonstrate thermonuclear ignition in the laboratory via inertial confinement fusion (ICF) [1]. ICF uses laser-driven implosions of a solid deuterium-tritium (DT) shell to achieve ignition conditions [2, 3]. Ignition is a thermal instability of a DT plasma driven by the energy deposition of the alpha particles ("alpha heating") produced by the fusion reaction D+T=α(3.5MeV)+n(14.1MeV). Ignition has never been achieved in a laboratory plasma and its demonstration is widely viewed as a major scientific achievement with important applications to fusion energy generation and to the stewardship of the nuclear stockpile. Unlike in steady state plasmas, as those envisioned for magnetic confinement fusion [4], assessing ignition in ICF is greatly complicated by the transient nature of implosions and the fact that ignition starts from the central hot region ("hot spot ignition") and then propagates to the cold and dense surrounding fuel ("burn wave propagation"). The fundamental mechanism at the basis of ignition is alpha heating of the DT fuel and its positive feedback on the fusion reaction rate.

Current experiments at the National Ignition Facility (NIF) have demonstrated significant alpha heating leading to amplifications of the fusion yield close to 3 folds [5–7]. Despite much work on assessing and measuring the degree of alpha heating, there are two crucial questions still unanswered with regard to ignition: (1) what is ignition in inertial fusion and (2) what fusion yields are required in ICF to claim that ignition has taken place. In the past, common metrics for ignition have related the fusion yield to the incident laser energy on target. The so-called *target gain*=1 condition has been widely used as the ultimate indicator of ignition [8]. Here, target gain is the ratio of the fusion energy output to the laser energy on target. Such a metric is not rooted in the burning-plasma physics of DT fuel and is unrelated to the onset of ignition. It is only motivated by its implications to fusion energy, where an energy output greater than the input is required for any viable fusion scheme. This metric is not an indicator of the onset of the thermonuclear instability and therefore it cannot be used to measure the ignition point.

In this work, we provide a physical definition of hot spot ignition in ICF which is of general validity for laser fusion. This definition of ignition identifies the onset of the thermal runaway within the hot spot of an ICF implosion just prior to the burn propagation in the dense fuel. To identify the ignition point, we first search for qualitative features distinguishing runaway burn in the entire fuel volume from sub-ignition alpha heating. The

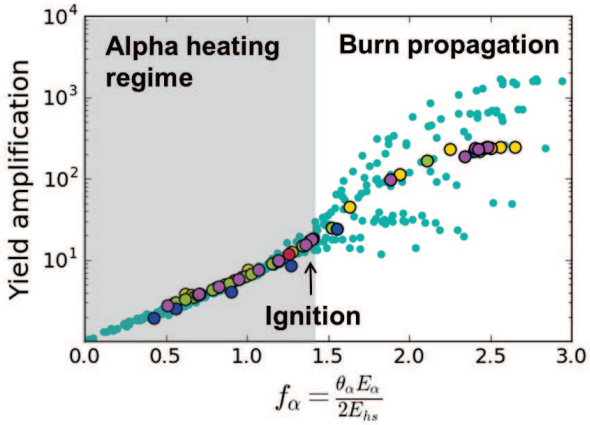

FIG. 1: The yield amplification is plotted as a function of f_α for the ensemble of 1-D LILAC [14] simulations (turquoise points). In the alpha-heating regime ($f_\alpha < 1.4$), the yield amplification depends uniquely on f_α regardless of the target mass, areal density, and temperature. After $f_\alpha = 1.4$, shell mass and burnup fraction determine the maximum fusion yield. The yellow, red, green, and dark blue points respectively represent 2-D DRACO [15] single mode simulations of modes 2, 4, 6, and 10. The purple points are multi-mode simulations perturbed by modes 2 and 4.

first distinctive feature is related to the different behavior of the yield amplification for implosions in the alpha heating regime versus implosions with propagating burn. Here the yield amplification = $Y_\alpha/Y_{no\alpha}$ where Y_α is the fusion yield measured in an experiment and $Y_{no\alpha}$ is the estimated yield without accounting for alpha particle energy deposition. It was shown in Ref [9] that in the alpha heating regime, the yield amplification depends uniquely on the dimensionless parameter f_α given by

$$f_\alpha \equiv \frac{1}{2}\frac{\theta_\alpha E_\alpha}{E_{hs}}, \tag{1}$$

where E_α is the total alpha-particle energy, θ_α is the fraction of alpha particles deposited into the hot spot, and E_{hs} is the hot spot internal energy at bang time (when the neutron production rate is maximized). The parameter f_α is designed to compare the deposited alpha energy to the hot spot internal energy at bang time. In the numerator, $E_\alpha = \varepsilon_\alpha Yield$ where $\varepsilon_\alpha = 3.5$ MeV and $Yield$ is the neutron yield. The factor 1/2 accounts for the fact that approximately one half of all of the fusion alphas produced have deposited their energy into the hot spot at bang time. In defining E_{hs}, the hot spot radius

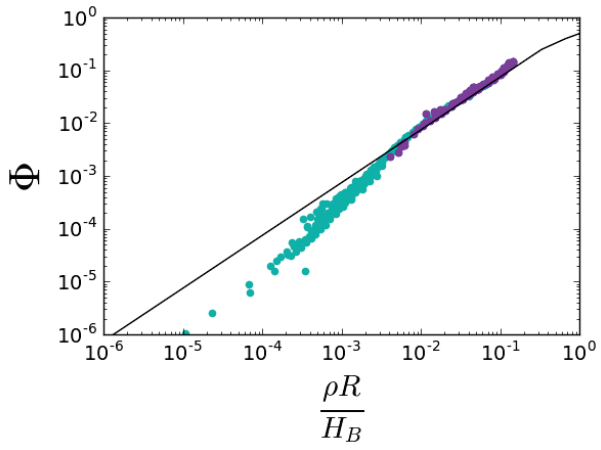

FIG. 2: In the burn propagation phase, the fuel burnup fraction Φ depends uniquely on the parameter $\rho R/H_B$ and follows the same scaling as predicted by theory (Eq. (2)). The dark violet points correspond to implosions with yield amplifications larger than 25 and the black line is the analytic curve from Eq. (2).

is the point where the neutron production rate drops to 17% of its maximum value. The lagrangian trajectory of this hot spot is then back calculated in time to determine the fraction of alpha particles absorbed in the hot spot, as was done in Refs. [12, 13].

In Fig. 1, the yield amplification due to alpha heating is plotted as a function of f_α where the yield amplification curves for many different targets are shown to overlap up to a critical value of $f_\alpha \simeq 1.4$. The 1-D simulation ensemble shown here contains implosion velocities between 200 km/s and 600 km/s, laser energies between 30 kJ and 10 MJ, and adiabats between 1 and 6 where the adiabat is given for DT by $\alpha = P/2.2\rho^{5/3}$, with the shell pressure P in megabars and the plasma density in g/cm^3 [11]. The 1-D database was generated by creating many ignited implosions with a variety of different target gains and then degrading them by reducing the implosion velocity or increasing the adiabat. The red, purple, green, dark blue, and yellow points are 2-D simulations of ignited targets degraded by single modes applied to the inner shell surface. Ignition occurs at the critical value $f_\alpha \approx 1.4$ corresponding to a yield amplification due to alpha heating of about 15x to 25x. For $f_\alpha < 1.4$, alpha-heating is mostly confined to the hot spot while for $f_\alpha > 1.4$, ablation of shell mass into the neutron producing region increases the fusion output significantly. The parameter f_α can be inferred from experimental observables and it can be used to identify ignition of the hot spot in all ICF implosions of DT-layered targets.

To investigate the nature of these qualitative changes occurring at $f_\alpha = 1.4$ and $\hat{Y}_{amp} = 15$ to 25, the dependence of the fusion yield on the areal density and temperature must be considered. In the runaway burn phase, rapid ablation of shell material into the hot spot qualitatively changes the fuel assembly into a system where the hot spot density is comparable to the shell density. The fnal burnup fraction Φ = neutron yield/NDT is then determined by considering the amount of fusion reactions that occur in the unablated compressed plasma before it disassembles. This calculation is described in Ref. [2] and gives

$$\Phi \simeq \frac{\rho R}{\rho R + H_B}, \tag{2}$$

where ρR is the total fuel areal density, $H_B \sim \sqrt{T}/\langle\sigma v\rangle$ is the burn parameter, T is the plasma temperature, and $\langle\sigma v\rangle$ is the fusion reactivity [10] (typically H_B is taken to be 6 or 7). In this case, the burn-up fraction becomes the dominant factor in determining the yield amplification. Therefore, given the unique role that f_α plays in describing the alpha heating regime, it is expected that this would no longer be the case after ignition and subsequent burn propagation. This is illustrated in Fig. 2 where the fuel burnup fraction Φ is plotted against the parameter $\rho R/H_B$ and compared with Eq. (2). Implosions in the alpha heating phase (where the burnup fraction is low) deviate from Eq. (2), while in the burn propagation phase (with yield amplifications > 25), a close relationship is observed between the fuel burnup Φ and the parameter $\rho R/H_B$ following Eq. (2). This supports the conclusion that after burn propagation occurs, the fusion yield is determined by Eq. (2) instead of the ignition parameter f_α.

References

[1] J.H. Nuckolls, et al, Nature **239**, 139(1972)
[2] S. Atzeni and J. Meyer-ter-vehn, *The Physics of Inertial Fusion* (Clarendon, Oxford, 2004); J. D. Lindl, *Inertial Confinement Fusion* (Springer, New York, 1998)
[3] J.D. Lawson, *Proc. Phys. Soc. London* B **70**, 6 (1957)
[4] J. Ongen, et al, Nature Physics, **12**, 398-410 (2016).[5]
S. Le Pape et al, Phys. Rev. Lett. **120**, 245003 (2018).[6]
T. Doppner et al, Phys Rev Let, **115**, 055001 (2015).[7] O. A. Hurricane et al, Nature **506**, 343 (2014)
[8] "An assessment of the prospects for Inertial Fusion Energy", National Research Council, The National Academies Press, Washington DC (2013).
[9] A. R. Christopherson et al, Phys. Plasmas **25**, 072704 (2018).
[10] H. S. Bosch and G. M. Hale, Nucl Fusion **32** 611 (1992).
[11] M. C. Hermann, M. Tabak, and J. D. Lindl, Nucl. Fusion **41**, 99 (2001).
[12] A. R. Christopherson et al, Phys. Plasmas. **25**, 012703 (2018).
[13] A. R. Christopherson, R. Betti, and J. D. Lindl, Phys. Rev. E, **99**, 021201(R) (2019).
[14] J. Delettrez et al, Phys. Rev. A **36**, 3926 (1987)
[15] P. B. Radha et al., Phys. Plasmas **12**, 056307 (2005).

Octahedral Spherical Hohlraum for Rev. 6 NIF Beryllium Capsule

Guoli Ren[1], Ke Lan[1,2,3]*, Yao-Hua Chen[1], Yongsheng Li[1], Chuanlei Zhai[1], and Jie Liu[1,2,3]

[1]Institute of Applied Physics and Computational Mathematics, Beijing, 100088, China
[2]Center for Applied Physics and Technology, Peking University, Beijing, 100871, China and
[3]Collaborative Innovation Center of IFSA, Shanghai Jiao Tong University, Shanghai 200240, China

For the indirect-drive inertial confinement fusion (ICF), the primary goal is to achieve ignition through sufficiently compressing the DT fuel capsule to ignition condition with laser-converted x-rays inside the high-Z hohlraum. For the National Ignition Facility (NIF) igni-tion experiments utilizing gas-filled cylindrical hohlraum, the primary obstacles are indicated to be time-dependent low-mode drive asymmetry complicated by the inner beam laser plasma instabilities (LPI), and hydrodynamic instabilities (HI) growth [1, 2].

To address the issue of radiation asymmetry, a new concept of octahedral spherical hohlraum [3] was pro-posed recently, which has been studied extensively through experiments and simulations and has present-ed inherent high radiation drive symmetry, high energy coupling efficiency and low level of LPI [4]. For another dominant concern of the growth of HI, the NIF exper-iments show that it is quite difficult to simultaneously achieve a high fuel compression and an effective HI sup-pression with the CH capsules [1]. On the other hand, the Beryllium ablator is a superior ablator as compared to the carbon based ablator such as CH and high density carbon (HDC), mainly due to its lower opacity, higher ablation pressure [5] and higher ablation front velocity.

We design an octahedral spherical hohlraum with 6 laser entrance holes (LEHs) for the Rev. 6 Be ignition capsule [5]. With an Au spherical hohlraum of 4400 μm in radius and six LEHs of 1200 μm in radius, a laser pulse of 2.15 MJ energy and 630 TW power is required to deliver the radiation drive for the Rev. 6 Be ignition capsule. Both our 1D and 2D simulations show that the expansion of Be capsule is slightly slower than that of the CH capsule under the same radiation drive in the spherical hohlraum, in spite of the higher ablation rate of Be. The reason is that the CH capsule has a higher opacity which causes a hotter ablated plasma and then a faster expansion of the CH ablated plasmas. The large volume of spherical hohlraum, together with the incident angle of 55° in its laser arrangement, leaves enough room for the laser transportation, thus avoiding the laser being absorbed by the Be capsule plasma and the con-sequent high risk of LPI. That means the higher mass ablation rate of Be does not affect the hohlraum energet-ics and symmetries inside the spherical hohlraum. With the high radiation drive symmetry and low risk of LPI of the octahedral spherical hohlraum, the superior ablation properties of Be capsule can be fully exploited and will have a higher opportunity to achieve ignition.

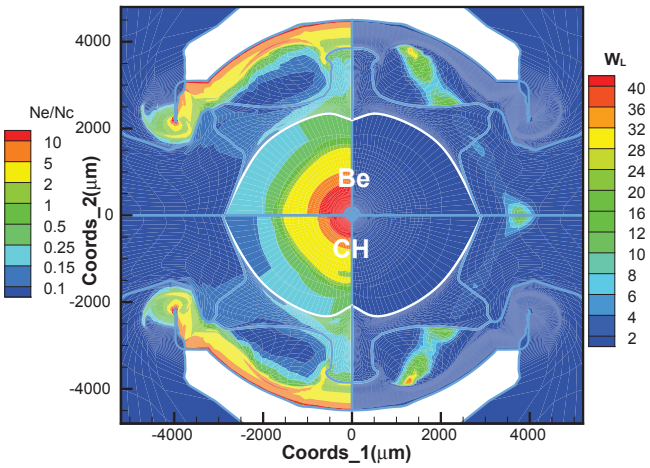

FIG. 1: Spherical hohlraum N_e (left side) and laser deposition item W_L (right side) maps for Be target (upper) and CH target (lower) at laser peak time. The outer boundaries of the capsules are shown in white lines.

References

[1] O.A.Hurricane, D.A.Callahan, D.T.Casey, P.M.Celliers, C.Cerjan, et al., Nature 506,343 (2014)

[2] D. S. Clark, C. R. Weber, J. L. Milovich, J. D. Salmonson, A. L. Kritcher et al., Phys. Plasmas 21, 010704 (2014)

[3] K. Lan, J. Liu, X. T. He, W. D. Zheng, D. X. Lai, Phys. Plasmas 21, 010704 (2014)

[4] Ke Lan, Zhichao Li, Xufei Xie, Yao-Hua Chen, Chunyang Zheng, et al., Phys. Rev. E 95, 031202 (2017).

[5] A. N. Simakov, D. C. Wilson, S. A. Yi, J. L. Kline, D. S. Clark et al., Phys. Plasmas 21, 022701 (2014)

[6] J. L. Kline, S. A. Yi, A. N. Simakov, R. E. Olson,D. C. Wilson et al., Phys. Plasmas 23, 056310 (2016)

*lan_ke@iapcm.ac.cn

Transmission-type bandpass filter for X-ray and its application in ICF diagnostics

Zhurong Cao*, Bo Deng, Qiangqiang Wang, Zhen Yuan, Tao Chen, Keli Deng, Yukun Li, Feng Wang, Jiamin Yang, Shaoen Jiang
Laser Fusion Research Center, China Academy of Engineering Physics, Mianyang, Sichuan, China

In the researches of indirect drive inertial confinement fusion (ICF), the detailed information of the x-ray radiation from the hohlraums is usually concerned [1-2]. Such information can be obtained from the X-ray images of the hohlraum. Before the X- ray images are obtained, it's important to firstly select the proper wavelength of the X-ray. The selection of X-ray wavelength can be achieved by monochromatic method, the bandpass method, or the method of whole spectral planar response [3-5]. The monochromatic method includes gratings and crystals, in which the strengths and spectral characteristics are generally needed to be considered. The method of whole spectral planar response can only be used to diagnose the radiative flux whose spectrum is known. The bandpass methods which include planar mirrors and filters is at present the most widely used method for selection of X-ray wavelength. However, there exist several shortcomings. Firstly, the multichannel x-ray instrument is often composed of multiple planar mirrors. Because the structures and the assembly of the mirrors may lead to some uncertainties, the calibrations and applications need very high accuracy due to the angular sensitivity of the mirrors. Secondly, since the view angle of the spectral instrument is too large, it is almost impossible to correct the differences caused by the angular factor of the channels. Thirdly, in research of plasma dynamics using the bandpass methods where the mirrors and pinhole are combined to image the plasma source, the system focusing and the intrinsic angle of the image lead to difficulties in system designs and practical applications.

A novel transmission-type bandpass filter has been proposed and developed to overcome the shortcomings mentioned above. The key component of such filter is a square-pore microchannel plate (MCP) [6–8], the working principle of which is shown in Figure 1(a) [6]. When X-ray lights are incident from a certain angle, the number of reflections vary with the incidence position. The deeper the position, the lesser the number of the reflections will be. Obviously, the number of reflections is determined by the length and the width of the channel as well as the incidence angle and the position at the gate. If we neglect the x-ray transmissions through the channel walls, the transport efficiency of the microchannel could be expressed as

$$R_n(\lambda, \theta) = k\prod_{i=1}^{n} R_S(\lambda, \theta) \qquad (1)$$

where λ is the wavelength of the x-ray, k is the open area fraction of the MCP, n is the number of reflections, and $R_S(\lambda,\theta)$ refers to the reflectivity of single reflection at incidence angle θ.

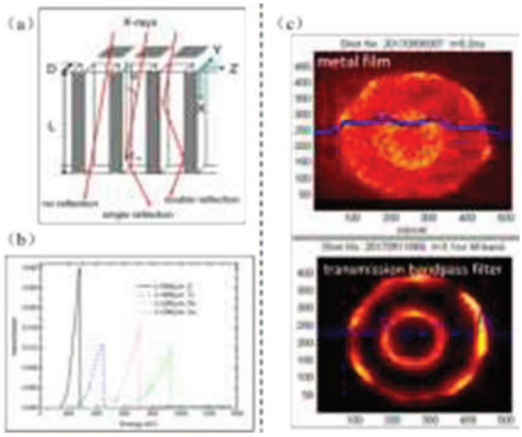

Fig 1 (a) working principle of the novel transmission bandpass filter with square-pore MCP; (b) The bandpass spectra of MCP combined with different filters; (c) Comparison of the X-ray images from metal films and the novel bandpass filter

We have calibrated the transport efficiency of the MCP devices on the Beijing Synchrotron Radiation Facility (BSRF). Using the 4B7B soft x-ray calibration beam (cover 50 to 1500 eV and has a resolution power of 200) on BSRF, we got accurate experimental results of transmission ratio of MCP for X-ray. Part of the results are shown in fig 1(b), from which we can see, when combined with filters, the square pore MCP can act as an excellent bandpass filter. It shows that in the case of L= 500 μm and θ = 61 mrad, the MCP has a narrow energy bandpass of the width 48 eV around 280 eV when it is combined with a 3 μm thick C filter. For L= 500 μm and θ = 44 mrad, the MCP combined with a 6 μm thick Ti filter achieves an energy bandpass of the width 80 eV around 450 eV. For L=250 μm and θ=34 mrad, the MCP combined with a 9 μm thick Fe filter achieved an energy band-

*cao33jin@aliyun.com

pass of the width 75 eV around 705 eV. For L=250 μm and θ =34 mrad, the MCP combined with a 15 μm thick Cu filter achieves an energy bandpass of the width 97 eV around 930 eV. In fact, we have combined this technology with gated X-ray detectors to develop a new type of transmission spectrally selective X-ray framing camera, which has been successfully applied in ICF hohlraum physics experiments in China. Fig. 1 (c) shows a comparison of the X-ray image of laser entrance hole of a gas filled cylindrical Au hohlraum obtained from the transmission-type bandpass technology with the data obtained from metal films. As can be seen from the figure, the signal-to-noise ratio (SNR) of the image obtained by the new energy selection technology has been significantly improved. From the linouts along the radial direction of the hohlraum we can see, the X-ray image obtained by transmission band-pass technique can more clearly show the position of LEH edge and plasma motion front in the hohlraum. The transmission-type X-ray band-pass technology enables the X-ray framing camera to acquire more detailed knowledge of hohlraum physics.

References

[1] K. Lan, J. Liu, D. Lai, et al. Phys. Plasmas, 21(1):3933(2014)
[2] K. Lan, Z. C. Li, X. F. Xie, et al. Physical Review E, 2017, 95(3):031202
[3] J. D. Lindl, P. Amendt, R. L. Berger, et al, Phys. Plasmas 11, 339 (2004)
[4] K. M. Campbell, F. A. Weber, E. L. Dewald, et al, Rev. Sci. Instrum. 75, 3768 (2004)
[5] A. Rindby, Nucl. Instrum. Methods Phys. Res. A 249, 536 (1986)
[6] Z. Cao, F. Jin, J. Dong ,et al. Optics Letters, 2013, 38(9):1509

This research was supported by Natural Science Fund of China (No. 11675157and No.11805180).

Progress on weakly nonlinear hydrodynamic instabilities in spherical geometry

L. F. Wang*[1,2], J. Zhang[1], K. G. Zhao[1], J. F. Wu[1], W. H. Ye[1,2], C. Xue[1], Y. K. Ding[1,2], W. Y. Zhang[1,2], and X. T. He[1,2]

[1] Institute of Applied Physics and Computational Mathematics, Beijing 100094, China, [2] Center for Applied Physics and Technology, Peking University, Beijing 100871, China

In the ICF central ignition implosion, a spherical target is uniformly irradiated and ablatively compressed, creating the temperature and density conditions necessary to achieve thermonuclear ignition. Throughout the entire ICF implosions, the integrity of the compressed shell is of critical importance. The final fuel assembly must consist of a low-density, high-temperature core surrounded by a high-density, low-temperature shell to maximize the number of fusion reactions that can occur while the fuel is inertially confined. To create the fusion hot-spot, the shell must maintain its integrity throughout the implosion to prevent significant shell deformation, ablator material mixing into the central region, and thermal mixing between the hot core and cold fuel. Hydrodynamic instabilities are of significant concern when trying to achieve the highest integrity of the compressed shell possible in ICF implosions, which can compromise the shell's integrity throughout the implosion, rupturing the shell or quenching the hot-spot before the target maximum gain is achieved. In this report, we summarize the progress of theoretical research of hydrodynamic instabilities in spherical geometry in our group over the past several years.

First, a weakly nonlinear (WN) model for the incompressible Rayleigh-Taylor instability in spherical geometry is developed [1]. The evolution of the interface with an initial small-amplitude single-mode perturbation in the form of Legendre mode (Pn) is analyzed with the third-order WN solutions. The transition of the small-amplitude perturbed spherical interface to the bubble-and-spike structure can be observed by our model. For single-mode perturbation Pn, besides the generation of P2n and P3n, which are similar to the second and third harmonics in planar and cylindrical geometries, many other modes in the range of P0–P3n are generated by mode-coupling effects up to the third order. With the same initial amplitude, the bubbles at the pole grow faster than those at the equator in the WN regime. Furthermore, it is found that the behavior of the bubbles at the pole is similar to that of three dimensional axisymmetric bubbles, while the behavior of the bubbles at the equator is similar to that of two-dimensional bubbles.

Second, a WN model is proposed for the multi-mode incompressible Rayleigh-Taylor instability in two-dimensional spherical geometry. The cosine-type and the Gaussian-type perturbations are discussed in detail. The growth of perturbations at the pole and that at the equator are compared, and the geometry effect is analyzed. It is found that the initial identical perturbation at the pole and the equator in the cross-sectional view will grow asymmetrically. In the linear regime, the perturbation amplitudes at the pole grow faster than those at the equator due to the different topologies. The geometry effect accelerates the ingoing motion and slows down the outgoing motion in the weakly nonlinear regime. This effect is stronger at the pole than that at the equator.

Third, a two-dimensional thin shell model has been developed for the Rayleigh-Taylor instability in spherical geometry. The present model generalizes the work of Ott to the case of spherical geometry. The governing equations for the shell motion and the deformation are obtained analytically and solved numerically. The linear growth rates from our model agree well with those from Mikaelian's work but are slightly larger than those from the classical prediction for low-mode perturbations. The perturbation amplitudes and bubble velocities from our model are in general agreement with those from the weakly nonlinear model of Zhang and Layzer's model, respectively. Moreover, the present model can investigate the shell evolution initialized by multimode axisymmetric perturbations in spherical geometry.

References

[1] J. Zhang, L. F. Wang, W. H. Ye, et al. Weakly nonlinear multi-mode Rayleigh-Taylor instability in two-dimensional spherical geometry. Phys. Plasmas, 2018, 25:082713

[2] J. Zhang, L. F. Wang, W. H. Ye, et al. Weakly nonlinear incompressible Rayleigh-Taylor instability in spherical and planar geometries. Phys. Plasmas, 2018, 25:022701

[3] J. Zhang, L. F. Wang, W. H. Ye, et al. Weakly nonlinear incompressible Rayleigh-Taylor instability in spherical geometry. Phys. Plasmas, 2017, 24:062703

[4] K. G. Zhao, C. Xue, L. F. Wang, et al. Two-dimensional thin shell model for the Rayleigh-Taylor instability in spherical geometry. Phys. Plasmas, 2019, 26:022710

[5] K. G. Zhao, C. Xue, L. F. Wang, et al. Thin shell model for the nonlinear fluid instability of cylindrical shells. Phys. Plasmas, 2018, 25:092703

[6] K. G. Zhao, L. F. Wang, C. Xue, et al. Thin layer model for nonlinear evolution of the Rayleigh-Taylor instability. Phys. Plasmas, 2018, 25:032708

*wang_lifeng@iapcm.ac.cn

CPA-Laser Pulses for Non-Thermal Initiation of Laser-Boron-Fusion

J. Krasa[1], D.H.H. Hoffmann[2], H. Hora*[3,4], S. Eliezer[5] , N. Nissim[5], J. Kirchhoff[3], G.J. Kirchhoff[3], W. McKenzie[3], D. Margarone[1], A. Picciotto[6], L. Giuffrida[1], G.A.P. Cirrone[7], G. Korn[1], B. Liu[8,9]

[1]Inst. of Physics, Academy of Science, Prague, Czech Republic [2], Institute of Nuclear Physics Tech. Univ. Darmstadt, Germany and Xian Jiao Tong University, Xian, China [3]Dept. Theoret. Physics, Univ. of NSW, Sydney, Australia [4]HB11 Energy P/L Sydney, Australia [5]SOREQ Research Center, Yavne, Israel [6]Fondazione Bruno Kessler, Micro-Nano Facility, Povo-Trento, Italy [7]INFN-Laboratori Nazionali dei Sud, Catania, Italy

[8]Hebei Key Laboratory of Compact Fusion, Langfang 065001, China [9]ENN Science and Technology Co., Ltd. LangFang, 065001, China

The key problem for controlled generation of nuclear fusion energy in a reactor for generating electricity is the needed temperature of hundrreds of million degrees Kelvin for thermal pressures. The sixty-five years of research has well achieved these temperatures under conditions in laboratories, both for ITER-like magnetic confinement as well as for NIF-like ICF when using nanosecond laser pulses. The temperatures were produced, but for too short times such that a breakthrough for a reactor has not yet been reached.

The need for million degrees temperatures is no surprise. The temperature for chemical reactions - as the burning of carbon - is in the range of eV needing ignition temperatures of few hundred of degrees Kelvin. Nuclear reactions are at ten million times higher energies. Nuclear burning needs then dozens of million degrees under thermal pressures. The sun burns hydrogen to helium at 15 Million degrees and the first deuterium fusion reactions at thermal equilibrium in a stellarator were measured in 1980 at 10 Million degrees.

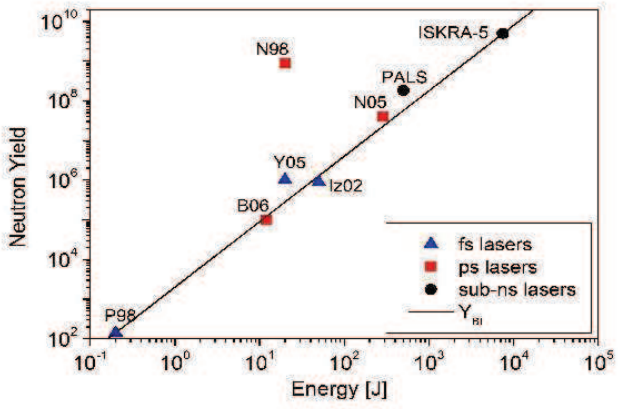

Fig.1.Neutrons from irradiation of laser pulses of fs to 100ps on the irradiated energy from targets with deuterium as fusion fuel [7] showing about 10,000 thousand higher yield with ps-CPA pulses (N98: P.Norreys et al 1998) than from thermal plasmas.

The laser initiated that ultra-extreme energy densities in pulses of picosecond ps duration will solve the nuclear fusion. Referring to the hydrodynamic equation of motion for the force density

$$\mathbf{f} = -\nabla p + \mathbf{f}_{NL}$$

contains the gasdynamic pressure p with the product of density and temperature T and the nonlinear force $\mathbf{f}_{NL}= \nabla\bullet\mathbf{M}$ with Maxwell's stress tensor **M** containing the electric and magnetic fields **E** and **H** of the laser, the laser frequency and the optical refractive index *n* of the plasma. To understand early measured nonlinear interaction, most general hydrodynamics resulted at interaction of 10^{18}W/cm^2 laser pulses, that within 1.5ps plasma blocks reached velocities of about 10^{10}cm/s without much heating, see Fig. 8.4 [1], confirming the dominance of the nonlinear force driven plasma block acceleration by ps against thermal pressures. The ultrahigh acceleration was 100,000 times higher than from best laser heating. Thanks to the Chirped Pulse Amplification CPA [2] the accelerations were measured at the predicted values [3].

Including the triple-alpha avalanche reaction of HB11 resulted in an increase by further four magnitudes [5] explaining the measurements, leading to the design of a fusion reactor see Fig. 16 of [6] – avoiding the hundred million degrees Kelvin of thermal pressures. For an environmentally clean, absolute safe, low-cost and inexhaustive electricity supply.

The nonlinear effect (see R. Feynman in Chapter 6.3 of [1]) of the plasma-block acceleration with the extreme ultrahigh ps CPA laser pulses can be seen in the diagram of Fig. 1 in the re-evaluation [7] of earlier DD-fusion measurements under the aspects of the recent results [6].

The non-thermal properties of the ultrahigh picosecond acceleration of plasma blocks by nonlinear-force acceleration resulted in ten-thousand times higher fusion neutron generation [3] than by thermal interaction, confirmed by much lower temperatures measured, clarified by comparison in the diagram, Fig. 1 [4]. Computations on non-thermal plasma-block ignition arrived at the surprising result that the well known extremely low classical thermal energy gain from fusion of hydrogen H with the boron isotope 11 with producing

*h.hora@unsw.edu.au

three alpha particles (HB11 fusion) arrived at about fife orders of magnitudes higher gains than classical up to the level of deuterium-tritium fusion. Including the three alpha avalanche increased the gain by further 4 magnitudes. This explains the measured billion times increased fusion yields of HB11 [5] than classically.

The fact that the measured bremsstrahlung was significantly lower than at thermal conditions (Fig. 1) and also at [6], indicated the extreme non-equilibrium properties of plasmas for the generators during times of less than several 100ps, as discussed as conclusion [8] of the presentation at the Symposium Hirschegg 2019

References

[1] Hora, H. Laser Plasma Physics, 2nd Ed. SPIE-book 2016

[2] Strickland, D. & G. Mourou, Opt. Comm. 56 (1985) 219

[3] Sauerbrey, R., Phys. Plasmas 3 (1996) 4712

[4] Hora, H. G.H. Miley et al. Opt. Comm.283 (2009) 412

[5] Eliezer, S., H. Hora et al. Phys. Plasmas 23 (2016) 050704

[6] Hora H., G. Korn, L.Giuffrida, D. Margarone, A. Picciotto, J.Krasa, K. Jungwirth, J. Ullschmied, P. Lalousis, S. Eliezer, G.H. Miley, S. Moustaizis and G. Mourou Laser & Part. Beams. 33 (2015) 607

[7] Krasa, J., D. Klier, et al. Laser and Particle Beams 31 (2013) 395

[8] Liu B. et al. Workshop ENN LangFang 20-22 Feb. 2019

Three-body formation mesonic bound states in ultradense plasmas of fusion catalysis concern

C. Deutsch[1], J.P. Didelez[2], A. Bendib[3], K. Bendib-Kalache[3]

[1]Laboratoire de Physique des Gaz et Plasmas - LPGP, UMR-CNRS 8578, UPS, Université Paris-Saclay, 91405 Orsay, France; [2]Institut de Physique Nucléaire - IPN, UMR - CNRS 8608, UPS, Université Paris-Saclay, 91405 Orsay, France; [3]Laboratoire Electronique Quantique - LEQ, Faculté de Physique, USTHB, BP. 12, El Alia 1611, Alger, Algeria

We first argue that negative muons in the MeV energy range can be fully stopped in warm-dense- matter and fast ignition scenario ultradense plasmas on a picosecond time scale, by taking into account the slowing down on partially de- generate electrons and charged hy- drogen isotope ions taken as classical. Atomic and molecular recombinations within these plasmas on the lowest available exoatom bound states states are then demonstrated. The very existence of in-situ produced exoatoms can be proved with x-ray line Stark broadening. Finally, a former conjecture about the negligibility of meson sticking on fusion-produced particles is reinforced. Mesonic catalysis of deuterium-tritium fusion reactions is then shown possible in short-lived plasma targets with rates that are orders of magnitude above cold deuterium ones. The dipole exoatom orientations clearly favor the cold and long-lived warm-dense-matter option [1].

A testimony to the stability of the D/T exoatoms is afforded by their rather low collision frequency with surrounding D/T ions (Table I) especially when remaining on their deepest bound level (n=1).

The given frequency is then explained as

$$\nu = N_{D/T}\pi d(n,l)^2 V_{th}^{D/T},$$

where

$d(n,l) = \sum_{l=0}^{n-1} d(n,l)$ with $d(n,l) = 0.5[3n^2 - l(l+1)]a_0^{\mu}$

referring to the l-averaged extension of μ-D/T excited states, and the averaged ion thermal velocity

$V_{th}^{D/T} = 9.79*10^5 \quad \sqrt{(T\ (eV)/2.56)}\,cm/s.$

According to Table I, ν remains always far below any acceptance threshold in the WDM target case, in the considered T range, when compared to target electron and ion frequencies.

The molecular binding process of concern for achieving μ-catalyzed fusion highlights a further D/T capture by the exoatom D/T μ. This can be obtained with a Langevin-like superposition (Fig.1a) [2] of the exoatom polarizability α with its asymmetric dipole contribution μD, so that the D/T capture rate constant (in cm3/sec and per exoatom) reads as (μ, relative mass) [3]

$$\overline{K} = (2\pi q/\mu^{1/2})[\alpha^{1/2} + c\mu_D(2/\pi k_B T)^{1/2}]$$

with [4]

$$\alpha = \frac{1}{n}\sum_{\ell=0}^{n-1}\left[a_0^{n\ell} + 2\sum_{m=0}^{\ell} a_2^{n\ell}\,\frac{3m^2 - \ell(\ell+1)}{\ell(2\ell-1)}\right] cm^3,$$

n	WDM ($N_{D/T} = 5.64\times10^{23}/\mathrm{cm}^3, T = 1.75eV$)			FIS($N_{D/T} = 10^{26}/\mathrm{cm}^3$)	
	1.75 eV	10 eV	50 eV	100 eV	1 keV
1	0.00214	0.00525	0.0113	2.865	9.06
2	0.0287	0.0507	0.127	38.51	121.8
3	0.141	0.3002	0.671	188.47	596
4	0.44	0.9705	2.1702		
5	1.07	2.400	5.367		
6	2.204	5.07	11.23		

Table I: Exoatom D/T μ on D/T^+ collision frequency (ps^{-1}) $\nu = N_{D/T}\,\pi\overline{d(n,\ell)}^2\,V_{th}^{D/T}$ in terms of main quantum number n, D/T^+ density $N_{D/T}$, atomic extension $\overline{d(n,\ell)}$, and ion thermal velocity $V_{th}^{D/T}$. Depicted n are restricted by the continuum lowering (1).

where

$$a_0^{n\ell} = \frac{n^4}{4}[4n^2 + 14 + 7\ell(\ell+1)],$$

$$a_2^{n\ell} = \frac{-n^4\ell}{4(2\ell+3)}[3n^2 - 9 + 11\ell + \ell(\ell+1)],$$

and the dipole moment $\mu_D = \frac{ea0}{2n}\sum_{l=0}^{n-1}(3\ n^2\text{-}\ell\ (\ell+1))$ averaged over (n, ℓ) levels through Holtsmark Stark mixing, with tuning parameter c featuring either a locked dipole (c = 1) or a rotating one (c = 0.1).

a) WDM target ($T = 1.75eV, N_{D/T} = 5.64\times10^{23}/\mathrm{cm}^3$)

n	1	2	3	4	5	6
c=0.1	1.34	5.71	14.45	28.85	50.2	79.73
c=1	10.55	39.5	89.2	161	256	375.5

b) FIS target ($T = 1keV, N_{D/T} = 10^{26}/\mathrm{cm}^3$)

n	1	2	3	4
c=0.1	64.32	374.46	1151.3	2757.0
c=1	132.64	624.95	1705.4	3601.25

c) FIS target ($T = 100eV, N_{D/T} = 10^{26}/\mathrm{cm}^3$)

n	1	2	3	4
c=0.1	80.73	434.64	1824.44	2857.3
c=1	296.8	1226.8	3036.75	5953.83

Table II: Three-body capture rates $N_{D/T}\,\overline{K}$ ($psec^{-1}$) in terms of exoatom main quantum number n and amount of dipole contribution c

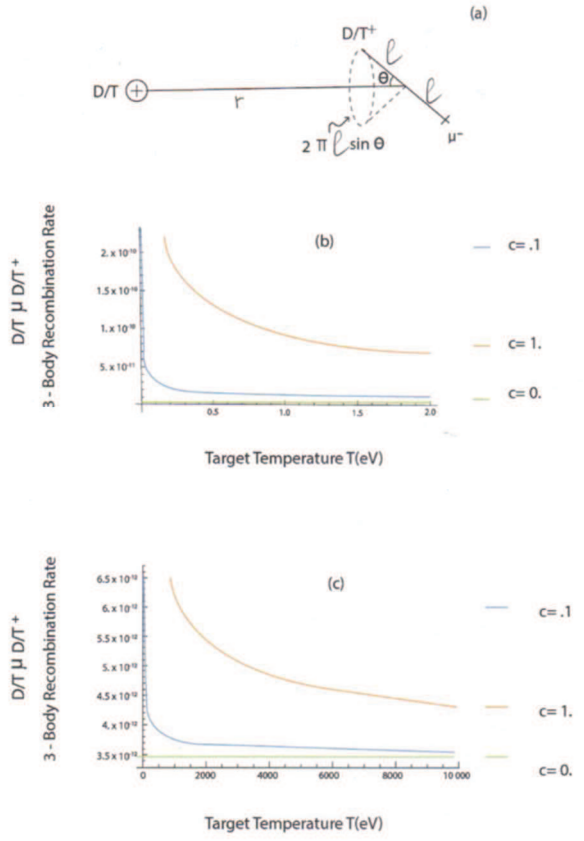

Figure 1: Three-body D/T μ D/T$^+$ recombination rates $\overline{K}$(cm^3/psec) in terms of target plasma temperature T(eV) parametrized with dipole contribution for n=2. c=0.1 (blue) qualifies a rotating dipole and c = 1 (orange) a fixed one. c=0 (light green) advocates a only polarizable dipole. **(a)** Geometry of D/T ion interacting with exoatom D/Tμ; **(b)** WDM target (N = 5.64x10^{23}/cm^3, T = 1.75eV); **(c)** FIS target (N = 10^{26}/cm^3, T = 1keV).

The temperature dependence is respectively given for WDM (Fig.1b) and FIS (Fig.1c) plasma targets. It is parametrized with the amount of dipole contribution, the only one displaying T variations.

Corresponding capture rates ND/T $\overline{K}$(psec^{-1}) are tabulated in Table II for $1 \leq n \leq 6$ (WDM) and $1 \leq n \leq 4$ (FIS). One witnesses a non-negligible contribution down to n = 1 with c = 0.1 on 1 ps time scale, FIS targets show up as the most effective ones. However, including the fact that WDM targets could keep their parameters up to 0.5 nsec, these latter appear as most promising for an experimental study. These capture rates can easily induce the production of hydrogenic molecular ions D/Tμ+ on low lying bound levels, thus allowing the triggering of a quantitatively significant amount of nuclear reaction. Moreover, present 3-body recombination rates steadily increase with n, while former two- body ones [1] do the opposite. Tables I and II shows clearly that the frozen dipole option (c=1) looks ap- propriate for n=1 WDM ground state. On the other hand, the rotating dipole (c=0.1) rules FIS levels.

References

[1] C. Deutsch, J.P. Didelez, A. Bendib and K. Bendib-Kalache, Phys. Rev. E98, 053204 (2018)

[2] P. Langevin, Ann. Chim. Phys. 5, 245 (1905)

[3] T.S. Su and M.T. Bowers, J. Chem. Phys. 58, 3027 (1973)

[4] D. Baye, Phys. Rev. A86, 062514 (2012)

Author Index

List of Contributing Institutes

Al-Farabi Kazakh National University
Almaty 050040, Kazakhstan

Beihang University
37 Xueyuan Road, Haidian District,
Beijing, 100083, China

Beijing Institute of Applied Physics and Computational Mathematics
Haidan, Beijing 10088, China

Center for Applied Physics and Technology
Peking University, Beijing, 100871, China

Dalian University of Technology
School of Physics and Optoelectronic Technology
Dalian116024 , Ganjingzi,
Liaoning, China

Excitech GmbH
Branterei 33, 26419 Schortens
Germany

Extreme Light Infrastructure - Nuclear Physics
Strada Reactorului 30, Bucharest - Măgurele 077126
Romania

Facility for Ion and Antiproton Research (FAIR)
64291 Darmstadt, Germany

Fondazione Bruno Kessler,
Micro-Nano Facility
Via Sommarive, 18, 38123 Povo,
Trento, Italy

Forschungszentrum Jülich
Wilhelm-Johnen-Straße, 52428 Jülich
Germany

Friedrich-Schiller-Universität Jena
Inst. für Optik und Quantenelektronik
Abbe Center of Photonics
07743 Jena, Germany

GSI Helmholtzzentrum für Schwerionenforschung GmbH
64291 Darmstadt, Germany

HB11 Energy P/L,
Freshwater, Sydney 2096, Australia

Hebei Key Laboratory of Compact Fusion
Langfang 065001, China

Heinrich-Heine-Universität Düsseldorf
Institut für Theoretische Physik I
40225 Düsseldorf, Germany

Helmholtz-Zentrum Dresden-Rossendorf e.V.
Bautzener Landstr. 4,
01328 Dresden, Germany

Helmholtz-Institut Jena
Fröbelstieg 3, 07743
Jena, Germany

Horia Hulubei National Institute for R&D in Physics and Nuclear Engineering
Strada Reactorului 30, Bucharest - Măgurele, Romania

IHEP – Institute for High Energy Physics,
NRC 'Kurchatov Institute",
Protvino142281, Moscow Region, Russia

Indian Institute of Technology Hyderabad
Department of Physics, ,
Kandi, Sangareddy,502285, India

INFN-Laboratori Nazionali del Sud
Via Santa Sofia, 62, 95125 Catania CT,
Italy

IMP - Institute of Modern Physics
Lanzhou 730000, China

Institute for Nuclear Research, RAS
7a, Prospect 60-letiya Octyabrya,
Moscow, 117312, Russia

Inst. of Physics, Academy of Science
Na Slovance 2, 18221 Prague,
Czech Republic

Institute of Problems of Chemical Physics (IPCP), RAS
142432 Chernogolovka, Russia

Instituto Superior Tecnico,
Av. Rovisco Pais 1, 1049-001 Lisboa,
Portugal

Joint Institute for High Temperatures, RAS
Moscow 125412, Russia

Johann-Wolfang-Goethe-Universität
Institut für Angewandte Physik
60438 Frankfurt, Germany

Justus Liebig Universität
Fachbereich 07
Ludwigstraße 23, 35390 Gießen
Germany

Keldysh Institute of Applied Mathematics - RAS
Moscow 125047, Russia

Laboratoire Electronique Quantique - ,
Facult´e de Physique, BP. 12,
El Alia 1611, Alger, Algeria

Laser Fusion Research Center, CAEP
Mianyang 621900, Sichuan, China

Lawrence Livermore National Laboratory
Livermore, CA 94550, USA

Lebedev Physical Institute, RAS
Leninskij Prospekt, 53
119991 Moscow, Russia

Leibniz-Rechenzentrum, LMU München
Boltzmannstraße 1
85748 Garching, Germany

Ludwig-Maxemilians-Universität
Fakultät für Physik
Am Coulombwall 1, 85748 Garching

Moscow Engineering Physics Inst. (MEPhI), Nat. Research Nucl. Univ.
Moscow 115409, Russia

Moscow Institute of Physics and Technology, Dolgoprudny,
Moscow Region, 141701, Russia

Moscow State University
Faculty of Physics
International Laser Center
Moscow 119991, Russia

NRC “Kurchatov Institute” - ITEP
Moscow 117259, Russia

National Research Center - ‘Kurchatov Institute’, Kurchatov Sq. 1,
123182 Moscow, Russia

Naval Research Laboratory
Plasma Physics Division
Washington, DC 20375, USA

Nizhny Novgorod State Technical University,
Minina St, 24, Nizhny Novgorod
603155, Russia

Osaka University
Open and Transdisciplinary Research Initiatives Institute,
Institute of Laser Engneering,
Graduate School of Engineering
Suita, Osaka 565-0871, Japan

Prokhorov General Physics Institute, RAS - Vavilov st., 38 Moscow 117942, Russia

Shanghai Jiao Tong University
Laboratory for Laser Plasmas,
Depart. of Physics and Astronomy,
Collaborative Innovation Center of IFSA
200240 Shanghai, China

School of Mathematics and Physics,
Queens University Belfast
7-9 College Park E, Belfast BT7 1PS, UK

Raja Ramanna Centre for Advanced Technology
Laser Plasma Division
Indore 452 013, India

Shanghai Institute of Optics and Fine Mechanics, CAS
State Key Laboratory of High Field Laser Physics,
Shanghai 201800, China

SOREQ - Nuclear Research Centre
81800 Yavne, Israel

Technische Universität Darmstadt
Institut für Kernphysik (IKP),
64289 Darmstadt, Germany

Technische Universität Dresden
Fakultät Physik
01062 Dresden, Germany

Technische Universität Kaiserslautern,
Fachbereich Physik und Landes-forschungszentrum OPTIMAS
67663 Kaiserslautern, Germany

Technische Universität München,
Physik Department E12
85748 Garching, Germany

Ulsan National Institute of Science and Technology, Ulsan 44919, Korea

Universitat Politécnica de Valencia
Dpto. de Matemática Aplicada
Camino de Vera, 46022 Valencia,
Spain

University of Lucknow
Department of Physics
Lucknow-226007, India

University of New South Wales
Dept. of Theoretical Physics
Sydney, NSW 2052, Australia

University of Ottawa,
75 Laurier Ave E, Ottawa,
ON K1N 6N5, Canada

Université Paris Sud - Saclay
Laboratoire de Physique des Gaz et Plasmas (L.P.G.P),
Institut de Physique Nucleaire
91405 Orsay, France

University of Peking (Beida)
College of Engineering,
School of Physics,
Center for Applied Physics and Technology,
Haidian, Beijing 100871, China

University of Rochester
Dept. Mechanical Engineering
Laboratory for Laser Energetics
Dept. Physics and Astronomy
Rochester, NY 14623-1299, USA

University of Warwick
Centre for Fusion, Space- and Astrophysics, Physics Depart.
Coventry CV4 7A1, UK

Weizmann Institute of Science
Rehovot 7610001, Israel

Xi'an Jiaotong University
School of Science
Xi'an, 710049, Shaanxi, China